Chapter *(Microsoft Word 2007)*

YTTERBIUM/SILICON AND YTTERBIUM/GERMANIUM INTERFACES: EARLIEST STAGES OF FORMATION

Mikhail Kuzmin*

Department of Physics and Astronomy
University of Turku
Turku, Finland
and
Ioffe Physical-Technical Institute
Russian Academy of Sciences
St. Petersburg, Russian Federation

and

Pekka Laukkanen
Department of Physics and Astronomy
University of Turku
Turku, Finland

ABSTRACT

Ytterbium/silicon (or germanium) interface can be classified as a model system for a family of interesting junctions − rare-earth/Si and -Ge contacts with distinct and outstanding physical and chemical properties among which are extremely low Schottky barrier heights on n-type Si, good electrical and thermal conductivities, low temperature of formation, ability to produce ultra-thin silicide or germanide nanowires by self-assembly. From the

* Address correspondence to: m.kuzmin@mail.ioffe.ru

technological viewpoint, a weak spot of electronic devices is electrical losses of which nature is closely related to the details of atomic and electronic structure of ultrathin region arising from the contact of two different materials at junctions. In particular, peculiar properties of only a few atomic layers in such contacts can drastically affect the performance of whole macroscopic devices. Therefore, knowledge of earliest stages of interface formation is not only of fundamental importance but also crucial for the creation of device junctions with tailored properties. The epitaxial Yb silicide and germanide interfaces provide a potential platform to develop device metal-semiconductor contacts which are typically non-crystalline junctions. This chapter deals with structures formed by depositing submonolayer quantities of Yb atoms on different Si and Ge surfaces, i.e., it addresses the ealiest stages of Yb/Si and -Ge interface formation. The characterization of such structures is performed *in situ* by using a wide arsenal of experimental techniques combined with *ab initio* calculations. In general, the results can be categorized into two groups. One of them concerns Yb-induced (n×1) and (n×2) (where n = 2,3,5,7,9…) reconstructions composed of atomic chains on (111) Si and Ge surfaces. The other group is related to (2×3), (2×4), and (2×6) reconstructions stabilized by Yb on (100) Si and Ge surfaces. The obtained results allow us to explain and predict why and which surface reconstcructions can be stabilized by rare earth and other metal adsorbates on both types of group-IV substrates. In particular, we demonstrate how the electron counting rule determines the formation of adsorbate-induced Si and Ge honeycomb chains on the (111) substrates and the adsorbate-controlled symmetrization of dimers on the Si(100) one, and how the saturate adsorbate coverages of these reconstructions are influenced by this rule. The understading of such interrelation is important to control the local defect and, thus, electrical losses at metal/group-IV junctions. The presented results provide a good ground for the improvement and development of rare-earth/Si and /Ge junctions in various applications.

Keywords: interface; surface; thin film; reconstruction; growth mechanism; stages of formation; atomic structure; electronic properties; ytterbium; silicon; germanium.

1. INTRODUCTION

1.1. Definition of interface

In this chapter, we deal with materials systems prepared by deposition of ytterbium layers onto group-IV semiconductor (Si and Ge) surfaces, which are called Yb/Si and Yb/Ge interfaces therein. The term *interface* is defined as a transition region (Fig. 1) from one material (A) to another (B) when they are

brought together to form physical contact. The chemical and physical properties of this region are often different from those of A and B, and thus the interface can be considered as a novel material. Depending on the reactivity of A and B, the interface can include up to several atomic layers. Here we focus mostly on the earliest stages of Yb/group-IV semiconductor interface formation where the Yb film thickness does not exceed one atomic layer, since understanding structures formed at these stages is very important from both fundamental and technological viewpoints (see below). Throughout the chapter, the interfaces can be also called *junctions*, or *contacts*, which is typical for applied studies.

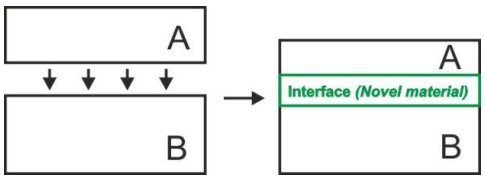

Fig. 1. Schematic illustrating the formation of interface. Two materials, A and B, are brought together in physical contact (left panel). In the resulting structure (right panel), the interface is the transition region between A and B, which often exhibits distinct properties.

From the practical viewpoint, the significance of metal/semiconductor interfaces is due to that they are a key part of most devices and components in electronics and photonics, such as transistors, laser and light-emiting diodes, infrared sensors, solar cells etc (e.g., see Streetman and Banerjee 2000). Usually, all those contain a semiconductor substrate with a pattern of n- and p-type regions, and metal/semiconductor junctions are required at least for transmitting the input and output signals to/from the functional semiconductor part of device. Depending on the relation of work functions (φ) of metal and semiconductor and the doping type of semiconductor, these junctions can be traditionally categorized into Schottky and Ohmic contacts. The physics of ideal metal-semiconductor junctions of both types have been thoroughly considered in literature (e.g., Streetman and Banerjee 2000, Li 2006). Schottky junctions are widely used as rectifiers. In Ohmic junctions, in contrast, the electric current flows across the interface as easily as possible with a minimum resistance. In practice, however, it is not so easy to produce Ohmic contacts because of the reactivity of semiconductor surfaces, as discussed below. Examples of effective Ohmic contacts are Au/n-Si and Al/p-Si.

1.2. Defects at metal/semiconductor interfaces

Unfortunately, the relation of metal and semiconductor work functions does not properly predict the behavior of metal/semiconductor junctions in practice. This is largely due to specific and frequently unpredictable properties of semiconductor surfaces (in particular, the electronic band structure and energy band gap), which drastically differ from the well-established properties of the semiconductor bulk. In other words, one cannot deduce the behavior of semiconductor surfaces and interfaces on the basis of the bulk properties. The reason is that the surfaces and interfaces can have dangling bonds and tend to reconstruct in order to eliminate these unsaturated bonds, i.e., the surface and interfaces change their atomic structures as compared to the bulk. This structural rearrangement can often result in new surface electronic states lying within the projected bulk band gap of semiconductor. A high density of such states (typically $>1\times10^{13}$ $eV^{-1}cm^{-2}$) causes Fermi level pinning at the semiconductor interface at certain energy level, which prevents the operation of metal-semiconductor junctions as Ohmic contacts (Tung 2014).

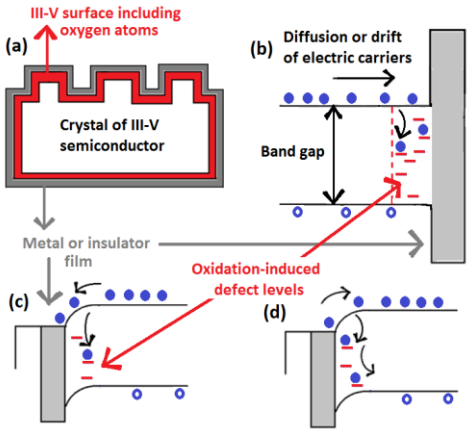

Fig. 2. Defects induced at metal/semiconductor junctions prior to the growth of metal film. The presence of such defects makes the properties of junctions less predictable.

Then, one can address the question why so many electronic states appear around the band gap at the metal/semiconductor interface, since most of broken (dangling) bonds of semiconductor atoms should become saturated via interaction

with valence orbitals of metal atoms at the interface region. The general reason is a high reactivity of semiconductor surfaces with environment, which still takes place prior to the interface growth. This leads to the formation of a new interface layer (1-10 nm thick) with specific chemical and physical properties. For example, most semiconductor crystals contain an oxidized surface part, because semiconductor oxidation is energetically very favored process and difficult to be avoided in air during the manufacturing of metal contacts. Fig. 2 illustrates the issue in the case of silicon crystals of which surfaces become readily oxidized prior to the film growth. Such surfaces often exhibit, in addition to various -Si-O- bonding configurations, a number of Si species bonded to carbon and hydrogen impurities. As a result, the interface region can contain defect-related electronic states in the band gap, making the properties of whole junction less predictable.

The oxidation, however, is not the only problem in producing the metal/semiconductor interfaces. Yet, semiconductor surfaces readily react with metal atoms: the latter can diffuse toward semiconductor and/or vice versa. The common feature of such reacted metal/semiconductor interfaces is that they have more or less amorphous atomic structure, in contrast to the well-ordered crystalline semiconductor bulk. The amorphous structure naturally includes a higher density of point defects (e.g., contamination, interstitials, vacancies, substitution sites) than the single-crystal material. From the technological viewpoint, this can drastically influence the electrical transport through or nearby the metal/semiconductor interfaces, and therefore, the chemical, electronic, and structural properties of interface layers need to be studied in order to predict the device performance. Also, one should emphasize that even a small amount of metal-induced defects at a semiconductor surface, which is significantly smaller than the density of atoms in a single atomic layer (i.e., $<< 1\times10^{15}$ cm^{-2}) can essentially affect the electronic, electric, and structural properties of semiconductor interfaces (Kuzmin et al. 2015; 2016).

Based on the above consideration, it is clear that knowledge of the earliest stages of interface formation is of high importance for the metal/semiconductor junctions not only from the fundamental viewpoints but also for technological tasks. In the following, we will focus on Yb/Si and Yb/Ge interfaces where the quantity of metal is restricted by one atomic layer.

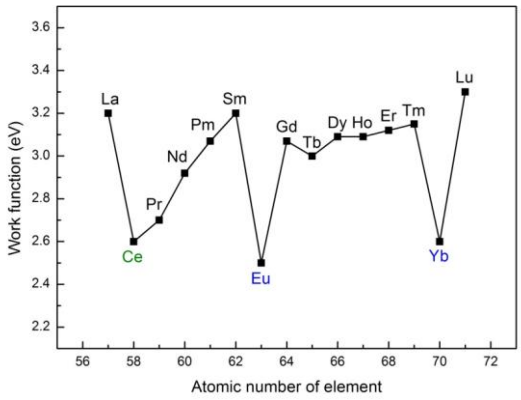

Fig. 3. Dependence of work function on the atomic number of element for the RE series. *The data are taken from: Nikolić et al. 1996*.

1.3. Ytterbium

Rare earths (REs) are considered to be low work-function metals. Within the RE series the dependence of work-function value on the atomic number of element is nonmonotonic and largely predetermined by the details of electronic structure of RE metal, in particular the number of electrons on the 4*f* subshell (Nikolić et al. 1996). The most stable configuration occurs when the localized $4f^n$ band of RE metal is zero filled, half-filled or fully filled, i.e., at n = 0, 7 or 14, respectively. Such RE metals, i.e., tetravalent Ce (the electron configuration $4f^0(5d6s)^4$) and divalent Eu ($4f^7(5d6s)^2$) and Yb ($4f^{14}(5d6s)^2$), are known to have lower work functions (2.5-2.6 eV) in comparison to the other REs possessing the trivalent $4f^{n-1}(5d6s)^3$ electron configuration (Fig. 3). Furthermore, these values are significantly less than work functions of most single-crystal semiconductor surfaces. For instance, the typical work function values for clean low-Miller-indices surfaces of Si and Ge crystals vary between 4.6 and 5.0 eV (Dillon and Farnsworth 1958; Allen and Gobeli 1962; Tallaj and Buyle-Bodin 1977), which is higher by 2.0 eV or more than that of Yb. Therefore, ytterbium (along with europium and cerium) is appealing to investigate its potential for Ohmic and Schottky metal contacts to n-type and p-type group-IV (and other) semiconductors, respectively. Indeed, high-performance anneling-free metal-insulator-semiconductor and metal-semiconductor Ohmic contacts on a GaN

substrate using low work-function Yb metal have been succesfully demonstrated and characterized recently (Wu et al. 2019). Moreover, it has been reported that Yb emerges as the best choice for future applications requiring a low work function electrical contact on graphene, and that Yb films at the metal-graphene interface have the strongest photovoltage response and maintain a relatively low surface roughness as compared to those of Pr, Eu, Er, and Y (DeJarld et al. 2018).

1.4. Overview of RE/Si and RE/Ge interfaces

Despite the successful attempts of physical realization of Yb metal contacts to various materials, the fabrication of ideal, atomically abrupt, interfaces between the Yb films and Si or Ge substrates is challenging, because the reaction occurs at such interfaces even at room temperature (RT). As already remarked in Subsection 1.2, this is the common problem in synthesizing various metal/semiconductor junctions, which leads to amorphization of interface region and defect-related interface states. The reactivity issues at the RE/Si and RE/Ge interfaces (including Yb/Si and Yb/Ge) at RT have been thoroughly discussed in two comprehensive review articles (Rossi 1987; Netzer 1995). In such systems, the reaction products and the properties of resulting interfaces have a specific character; one can briefly summarize that the behavior of RE/Si and RE/Ge is dramatically influenced by the temperature. Therefore, the scenarios of interface formation for these systems at RT and elevated temperatures should be explicitly distinguished.

At RT, the thickness of interface region where the reaction between RE and Si or Ge has occured is dependent on the chemical nature of deposited metal, substrate material, and crystallographic orientation of surface plane. For Yb, the thickness of reacted interface can vary from four atomic monolayers (ML) at the Yb/Si(111) (Rossi et al. 1983; Braicovich et al. 1986) to ~20 ML at the Yb-Ge(111) (Nogami et al. 1986). Such interface regions represent an Yb-rich mixed phases with no long-range order. The RE/Si and RE/Ge interfaces at RT are metastable, and upon annealing at moderate temperatures ($\leq$ 300-400°C), they irreversibly change to Si- or Ge-rich interfaces. For this reason, we do not consider the non-annealed RE/Si and RE/Ge hereafter.

When the RE/Si and RE/Ge interfaces are annealed at ~350-400°C of higher, the metastable metal films transform into RE silicide or germanide phases. In most cases, the crystal lattice of RE silicides is of AlB_2 type (Iandelli et al. 1979; Koleshko, Belitsky, and Khodin 1986). It hosts the RE atoms in hexagonal planes stacked directly on one another, similar to the case of graphite, however, the *c* axis is not much larger than the *a* axis in the RE silicide lattice, in contrast to

those of graphite. The Si atoms occupy the interstitial sites between the RE hexagonal planes, and the important feature of respective Si planes is the presence of a number of vacancies (Chi, Tsai, and Chen 2003). This makes the stoichiometry of AlB_2-type RE silicides is different from the ideal $RESi_2$; it corresponds to $RESi_{2-n}$ with n ~ 0.2-0.3 (pseudo-disilicides). Yb silicide phases also display Si-rich stoichiometries and can have the distorted AlB_2-type structure ($YbSi_{1.8}$) and hexagonal Th_3Pd_5-type structure with slightly lower Si concentration (Yb_3Si_5) (Iandelli et al. 1979). A similar Yb_3Ge_5 structure is found for the ytterbium pseudo-digermanides (Rossi 1987).

Two circumstances should be taken into account for understanding the growth mechanisms of silicides and germanides at RE/Si and RE/Ge interfaces. First, these compound phases grow at RE/Si and RE/Ge interfaces via nucleation, which is a specific property of both systems (Smith, Johnson, and Tharp 1965; d'Heurle and Gas 1986; Koleshko, Belitsky, and Khodin 1986), while the dominant behavior of all other silicides is the diffusion-controlled reactivity (Rossi 1987). The reason for the nucleation-controlled reaction in RE silicides and germanides is related to the presence of vacancies in the group-IV sublattice of the RE pseudo-disilicide or -digermanide structure. The fast diffusion of Si atoms is favored by the abundance of vacancies in the $A1B_2$-type lattice. The RE atoms are not mobile in the $A1B_2$-type structure up to ~1000°C representing twice as high a temperature than that needed for fast mobility of silicon, and for nucleation of $RESi_{2-n}$ (~400°C) (Baglin, d'Heurle, and Petersson 1980; Baglin, d'Heurle, and Petersson 1981; d'Heurle 1986).

Second, it is essential that due to a significant difference in activation energy for diffussion of Si and RE atoms (~1.5 and ~3 eV, respectively), Si to RE mobility ratios are estimated to be of the order of 10^5 at 1000°C and 10^{13} at 275°C (d'Heurle and Gas 1986). For this reason, the nucleation of $RESi_{2-n}$ is hindered by the low mobility of the RE at RT, while it gets an explosive behavior at ~350-400°C when the diffusion of silicon becomes large enough for penetrating a frozen RE hexagonal network. The kinetics of the pseudo-disilicide formation at RE/Si systems, once the critical temperature is reached, is very fast, which clearly distinquishes these systems from the other classes of metal silicides (Iandelli et al. 1979; Thompson and Tu 1982).

The epitaxial growth of Yb silicides on Si(111) and Si(100) has been reported by several groups (Knapp and Picraux 1986; Abbati et al. 1987; Wigren et al. 1991; Hofmann et al. 1992; Hofmann et al. 1993; Krachino et al. 1999; Pasquali, D'Addato, and Nannarone 2002; Kuzmin et al. 2004[a]; Kuzmin et al. 2004[b]; Perälä et al. 2009). It is shown the morphology of Yb silicide film is strongly dependent on the growth parameters (Hofmann et al. 1992; Hofmann et al. 1993). The Si

vacancies in the silicide lattice can form an ordered structure with the $(\sqrt{3}\times\sqrt{3})R30°$ periodicity observed by low-energy electron diffraction (LEED) (Wigren et al. 1991) and transmission electron microscopy (Chi, Tsai, and Chen 2003), while the top of silicide film is terminated by the Si layer (Hofmann et al. 1992; Hofmann et al. 1993). The Si(111) surface in between the Yb silicide islands reveals an Yb-induced (2×1) reconstruction observed with scanning tunneling microscopy (STM) (Hofmann et al. 1993). Electronically, the epitaxial Yb silicide phase reveals a relatively low density of states (DOS) at the Fermi level, suggesting a high quality of Yb/Si(111) interface, while an Yb-rich mixed phase at the Yb/Si(111) interface at RT shows a high DOS at the Fermi level and a clearly metallic behavior (Hofmann et al. 1992). In this view, the electronic structure of epitaxial Yb disilicide films on the Si(111) can be considered to be semimetallic rather than purely metallic.

Several RE disilicides demonstrate a fascinating ability to form spontaneously ultralong (i.e., with micrometer scale length) self-assembled nanowires on the Si(100) due to the highly anysotropic lattice mismatch at the respective interfaces (Chen et al. 2000; Nogami et al. 2001; Preinesberger et al. 2002; Owen, Miki, and Bowler 2006). The Yb/Si(100) interface is shown to belong to this family of systems and can follow a similar trend (Kuzmin et al. 2004[a]).

It has been reported that the Yb disilicide is a promising material, in particular, for the metal-oxide-semiconductor field-effect transistor (MOSFET) technology (Zhu et al. 2004). MOSFETs with heavily doped source/drain (S/D) contacts have encountered technological difficulties when miniaturization below the 32 nm node is considered, e.g., for limiting short-channel effects arising from lateral diffusion of dopants in the channel during activation, and for reaching low sheet and contact resistances with ultra shallow junctions. To overcome these difficulties, the replacement of conventional high doping S/D's by the Schottky barrier MOSFET architecture, where S/D contacts are metallic, has been suggested, and $YbSi_{2-x}$ for n-Si has been considered as potential candidate for Schottky barrier MOSFET contacts since such contacts achieve low Schottky barrier heights with electrons (≈ 0.3 eV).

For the application of Yb/Si and Yb/Ge, it is crucial to prepare the respective high-quality interfaces with low electrical losses. As already mentioned in Subsection 1.2, the density of electronic states as low as 1×10^{13} $eV^{-1}cm^{-2}$ can cause Fermi level pinning. This implies that a low submonolayer amount of structural defects, such as unsaturated dangling bonds, point defects etc., can strongly affect the properties of devices based on such junctions. Hence, detailed knowledge of earliest stages of Yb/Si and Yb/Ge formation is very important. It is known that in such systems, the silicide or germanide film growth requires a

critical coverage of RE atoms, which is usually about or lower than one monolayer (Rossi 1987; Netzer 1995). Below this coverage, the silicide and germanide phases do not form. Instead, Yb atoms induce so-called two-dimensional (2D) reconstructions that can involve not only submonolayer amount of metal atoms but also reconstructed layer(s) of substrate atoms on top of the group-IV crystal (Kofoed, Chorkendorff, and Onsgaard 1984; Wigren et al. 1993[a]; Wigren et al. 1993[b]). Clearly, the atomic and electronic structures of such reconstructions, in particular, the arrangement of defects in the reconstructed topmost Si and Ge layers can be very essential for the resulting RE/group-IV junctions. Nevertheless, in contrast to silicide and germanide phases, 2D reconstructions in RE/Si and RE/Ge systems have received less attention. A brief reviews of RE/Si reconstructions reported in early studies can be found in literature (Netzer 1995). However, the atomic structures and electronic properties of 2D reconstructions in Yb/Si and Yb/Ge systems have still remained far from being fully realized or even investigated (in the case of Ge substrates). Below, we will consider the current status of such investigations and present our results shedding more light on the Yb/Si and Yb/Ge reconstructions.

2. PREPARATION AND CHARACTERIZATION OF YB/SI AND YB/GE INTERFACES : GENERAL ASPECTS

Since even small quantities of impurities can affect the properties of RE/semiconductor contacts, the basic strategy in studying the Yb/Si and Yb/Ge is to prepare and characterize the interfaces *in situ*, i.e., in the ultra-high vacuum (typically at the residual pressure ~10^{-11}-10^{-9} mbar), avoiding an exposure in air in order to minimaze the contaminations from environment. The preparation of an atomically clean and smooth surface of group-IV semiconductor, which is the absolute requirement for acquiring reliable results, is the first step. There are standard methods allowing the cleaning of Si and Ge surfaces at the atomic scale. For Si, the cleaning in surface science is typically performed by a rapid flashing at 1200-1250°C by using the direct-current heating to remove oxygen and carbon contaminations from the surface. For Ge, the surface can be cleaned by repeated cycles of Ar^+ ion bombardment, followed by annealing at 600-700°C needed to reduce the created defects. The cleanness of surfaces can be verified by different experimental techniques, e.g., x-ray photoelectron specroscopy or Auger electron spectroscopy (AES). These techniques are sensitive to the chemical nature of impurities, and the limit of their detection is usually ~0.01 ML. After the cleaning procedure, the Si(111) and Ge(111) surfaces exhibit the famous (7×7) and c(2×8)

reconstructions, respectively, while the Si(100) and Ge(100) have the same (2×1) reconstruction at RT (Mönch 2001). These reconstructions, however, are destroyed after the deposition of Yb, and therefore, we do not consider the structures of cleaned substrate surfaces further. Obviously, the atomic-scale cleanness and smoothness of pristine surface is very crucial for the quality of interfaces upon the metal deposition. It is worth noting that the above direct current heating is not possible on wafer scale for technology, but still vacuum technology can be used after the common wet chemical etching procedure of wafers. The post heating of the etched wafers removes contaminants and enhances crystalline nature of the starting surfaces, which is a key step toward epitaxial metal-semiconductor interfaces.

The next step in producing the Yb/Si and Yb/Ge interfaces is the deposition of metal films. It can be performed either on the substrate held at RT, followed by annealing at appropriate temperatures, or on the heated substrate directly. The two methods give rise to similar results. In this study, the annealing/deposition temperature was 530°C for the Si substrates and 400°C for Ge. Our tests showed that at such temperatures, ytterbium does not evaporate from the sample, and that these temperatures are high enough to arrange a long-range order in the resulting interface and, thus, fabricate the well-defined interfaces with the ground-state structures.

Beside the temperature, the other important parameter is the metal coverage that is expressed in ML throughout the chapter. As widely acccepted in surface studies, one monolayer is refered as to the atomic density on the clean surface; that is, 1 ML Yb nominally corresponds to the number of semiconductor atoms on the substrate surface. Table 1 summarizes these values for Si and Ge surfaces with (111) and (100) crystallographic orientations. Also, the coverages can be expressed via the film thicknesses which are also presented in Table 1.

Table 1. Atomic concentrations (cm^{-2}) and film thicknesses (Å) corresponding to one monolayer of Yb on various Si and Ge surfaces.

	Si(111)	Ge(111)	Si(100)	Ge(100)
Atomic concentration	7.84×10^{14}	7.22×10^{14}	6.78×10^{14}	6.24×10^{14}
Thickness	3.24	2.98	2.80	2.58

For the characterization of grown interfaces, combining comprehensive experimental and theoretical techniques is desirable, since applying a single

method is frequently not enough for arriving at reliable conclusions. In this study, we have utilized a variety of experimental tools, including STM, scanning tunneling spectroscopy (STS), LEED, core-level and valence-band photoelectron spectroscopies (CLPES and VBPES, respectively) using the synchrotron radiation, thermal desorption spectroscopy (TDS), AES, and work-function change ($\Delta\varphi$) measurements using the contact-potential-difference method. The STM, STS and most of LEED observations are performed at the University of Turku in Finland. The TDS, AES, and $\Delta\varphi$ measurements are carried out at the Ioffe Institure in St. Petersburg, Russian Federation. The CLPES and VBPES experiments are conducted in beamlines 33 and I4 at the MAX-lab synchrotron radiation laboratory in Lund, Sweden. In addition, experimental results are provided with theoretical support on the basis of density functional theory (DFT) calculations. All these methods are well known and serve '*working horses*' in surface science for long. The detailed description of each method can be easily found in numerous publications in literature.

It is worthwhile noting that the techniques have own restrictions some of which are not always obvious *a priori*. For instance, STM, STS, and $\Delta\varphi$ measurements might not be suitable for probing the buried interfaces. In contrast, photoemission measurements frequently have a low sensitivity to the surface when the detected signal is strongly contributed by the bulk because of relatively large inelastic mean free path of photoelectrons, which is dependent on the kinetic energy. In other words, the probing depth in photoemission can frequently be much greater than the thickness of surface layer. Yet, some techniques, e.g., STM can be too slow. The acquisition time in this technique is on order of 10^{-3}-10^{-1} s. It is by many orders of magnitude greater that the characteristic time of most elementary processes on surfaces, of which rate is on order of 10^{12}-10^{15} s^{-1}. Thus, STM provides an average picture in time. The well-known example of such behavior is how STM shows up buckled dimers on the Si(100) surface: in fact, they appear as symmetrical ones in STM images at RT (Hamers, Tromp, and Demuth 1986; Wolkow 1992). The reason is that there are two tilting configurations of the buckled dimer, and fast fluctuations (the so-called flip-flop motion) occur between them with the residence time of ~50% for each configuration, leading to an average of the two on the timescale of STM image acquisition. In contrast, the timescale in photoelectron spectroscopy is significantly shorter (~10^{-18}-10^{-17} s), which is determinated by the rate of photoionization process and the core-hole lifetime. This technique provides a '*snapshot*' of the buckled dimer.

3. PROPERTIES OF YB/SI AND YB/GE INTERFACES

3.1. Growth mechanism

As already discussed, the formation of silicide and germanide phases at RE/Si and RE/Ge interface requires the critical metal coverage for the disruption of Si-Si or Ge-Ge bonds and onset of reaction between the grown film and substrate. To examine the issue, a comparative study of Yb/Si(111) and Yb/Si(100) interfaces has been performed by using TDS and AES.

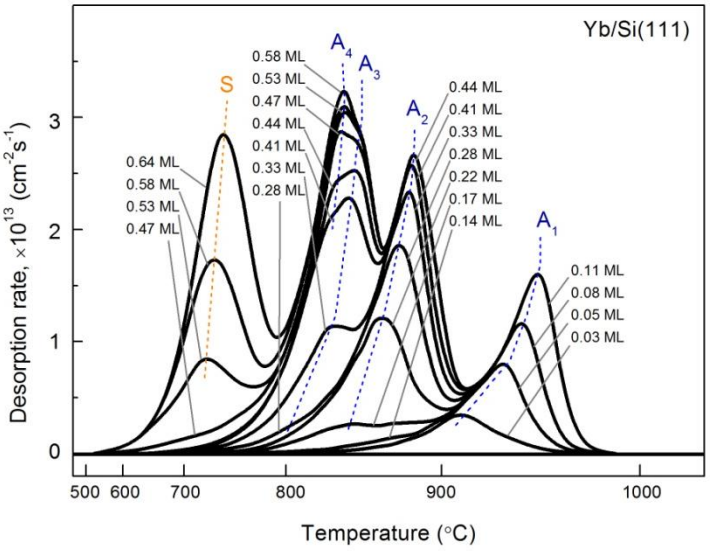

Fig. 4. Thermal desorption spectra for the Yb/Si(111) as function of metal coverage. The desorption peaks corresponding to adsorbed phases (2D reconstructions) are denoted by A_1, A_2, A_3, and A_4. The desorption peak corresponding to the Yb silicide phase is denoted by S.

Fig. 4 shows a series of TD spectra measured for the Yb/Si(111) as function of metal coverage (Krachino et al. 1997[a]). A few peaks appear in these spectra upon increasing the coverage, indicating that several Yb-induced phases with different desorption temperatures and thermal stabilities are formed. In the lowest coverage range (0-0.13 ML) one observes the highest temperature peak, A1. It is

well resolved from the second highest temperature peak (A2) that is found in the coverage range of 0.14 to 0.27 ML. The A3 and A4 peaks, which are shifted to the lower temperature and poorly resolved, appear and evolve in the 0.27-0.46 ML range. All these features correspond to several (at least four) 2D reconstructions of Yb on the Si(111) at <1/2 ML. As shown below, these peaks correspond to (3×2), (5×1), (7×1) and (2×1) structures.

At 0.46 ML a fifth, qualitatively different, peak (S) appears. It is found at a lower temperature as compared to the A1-A4. The S raises without any saturation even for the thick deposited films (not shown here). The analyses show that (i) the Yb evaporation rate at the leading edge of S is by seven orders of magnitude lower than that of the metallic bulk Yb, as estimated from the vapor pressure for pure Yb, and (ii) the activation energy for Yb evaporation from the phase corresponding to the S (2.9 eV) is essentially higher than the heat of sublimation for metallic Yb (1.7 eV). Thus, the S peak can be assigned to the Yb silicide phase.

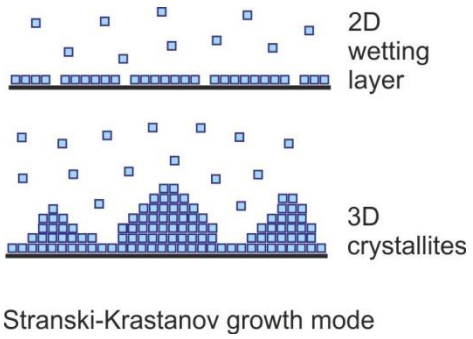

Fig. 5. Schematic of Stranski-Krastanov growth mode.

The above results indicate that the formation mechanism of Yb/Si(111) can be clearly divided into two stages: (1) Adsorption stage, where a few adsorbed phases, or 2D reconstructions, are formed below 1/2 ML, and (2) Silicide formation stage, where the onset of Yb-silicide formation occurs at ~1/2 ML and the silicide film grows without limitation at higher coverages. As shown earlier (Netzer et al. 1993), the Yb silicide film is not entire and composed of 3D islands. Thus, the mechanism of Yb/Si(111) formation closely resembles the well-known Stranski-Krastanov (SK) growth mode. It is illustrated in Fig. 5. In the beginning a 2D film (so-called wetting layer) is formed at the adsorption stage. After the wetting layer is completed, 3D crystallites of deposited material start to grow atop the 2D film. The growth mechanism of Yb/Si(111) is different from that of Fig. 5

in that the 3D islands comprises both adsorbate and substrate atoms (3D silicide islands).

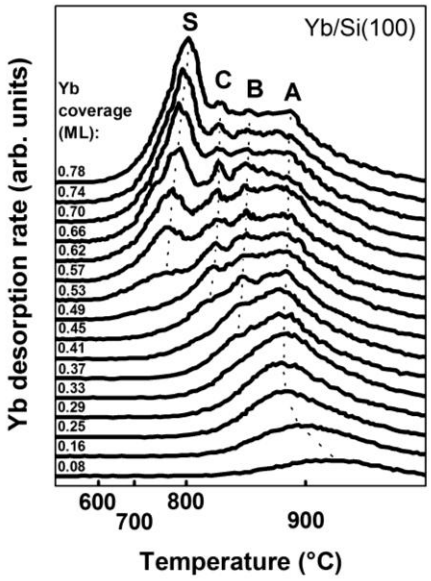

Fig. 6. Thermal desorption spectra for the Yb/Si(100) as function of metal coverage. The desorption peaks corresponding to adsorbed phases (2D reconstructions) are denoted by A, B, and C. The desorption peak corresponding to the Yb silicide phase is denoted by S.

A similar growth mechanism is found for the Yb/Si(100) system (Fig. 6) (Kuzmin et al. 2003[a]). For this system, a broad single peak (A) is found at low coverages (≤0.33 ML) and lower-temperature peaks (B and C) at higher submonolayer coverages. The resolution of all peaks is poorer than those of Yb/Si(111). Finally, after the Yb quantity exceeds one-half a monolayer, the peak S appears in TD spectra. It is interpreted as originating from the silicide phase. Thus, both systems suggest the critical Yb coverage for the onset of silicide formation (~1/2 ML). Prior to the silicide growth, Yb-induced reconstructions, or a wetting layer in the context of SK growth mechanism, are formed. The formation of such a layer is energetically favorable over the formation of silicide phase, since the reconstructions are thermally more stable, as seen from the TDS data in Figs. 4 and 6.

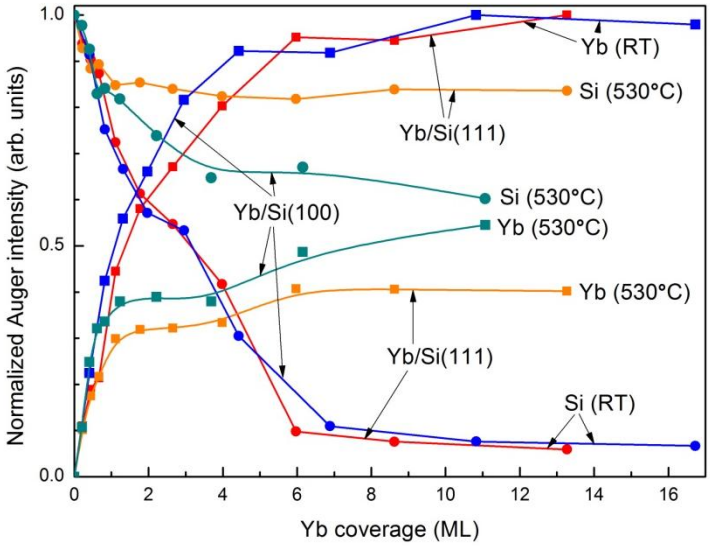

Fig. 7. Dependences of Auger Si LVV (92 eV) and Yb NNN (180 eV) intensities (peak-to-peak amplitudes) on the Yb coverage for Yb/Si(111) and Yb/Si(100) systems. The results are obtained non-heated interfaces (RT) and those annealed at 530°C.

The above conclusions are well supported by AES data. Fig. 7 shows the intensities of Si LVV (92 eV) and Yb NNN (180 eV) Auger signals as function of Yb coverage for the Yb/Si(111) and Yb/Si(100) before and after annealing at 530°C. As seen, the annealing does not affect the Auger amplitudes in the coverage regime of 0-0.5 ML for the Yb/Si(111) and 0-0.6 ML for the Yb/Si(100). This means that there is no intermixing between Yb and Si atoms upon heating at these coverages. The intensity of Yb peak increases linearly with the metal amount within these ranges, implying the formation of 2D wetting layer (adsorbed phases).

Drastic changes occur at higher coverages. Upon annealing, the Yb and Si intensities significantly decrease and increase, respectively, giving a clear evidence for the Yb silicide formation. The analysis shows that the stoichiometry of Yb silicide in the Yb/Si(111) is close to $YbSi_{2-x}$ (x = 0.2-0.3), while the silicide phase in the Yb/Si(100) is more metal-rich.

In the following, we will consider 2D reconstructions formed at the first stage of interface formation on both Si and Ge surfaces.

3.2. 2D reconstructions on Si(111) and Ge(111)

The first observation of ordered 2D structures induced by Yb on the Si(111) surface was reported more than three decades ago (Kofoed, Chorkendorff, and Onsgaard 1984). They found (2×1), (5×1) and (3×1) LEED patterns after annealing of ~1 ML Yb on the Si(111) at 700-800, 800-900, and 1000-1100 K, respectively. Later, similar structures have been reported in other studies (Hofmann et al. 1992; Wigren et al. 1993[a,b]; Krachino et al. 1997[a]; Vaara et al. 2003[a,b]). Tentative atomic models have been proposed for these reconstructions, where the Si structure is bulk-terminated and the metal atoms are divalent and adsorbed at bridge sites (Wigren et al. 1993[a]; Krachino et al. 1997[a]). Such models, however, do not explain the high thermal stability of such reconstructions and many other experimental observations (see below).

It has been also discovered that the lowest-coverage Yb/Si(111) reconstruction, which causes the (3×1) spots in LEED, has actually the (3×2) periodicity (Wigren et al. 1993[a]). The double periodicity can be manifested in the form of 1/2-order LEED streaks at RT. The previous identification of Yb/Si(111)(3×2) as the '(3×1)' is not surprising, since a closely related (3×1) reconstruction has been reported for a family of alkali metals (AM: Li, Na, and K) on the Si(111), as described in Subsection 3.2.1. Next, we consider the (3×2) structure on Si(111) and its counterpart, Ge(111), and then other higher-coverage reconstructions of Yb/Si(111).

3.2.1. Yb/Si(111)(3×2)

First of all, it is worth presenting a retrospective view of (3×1) and (3×2) structures stabilized by various adsorbates (AM, RE, and alkaline earth metals (AEM)) on Si(111) and Ge(111). The constructing of atomic models for these structures has been a puzzling issue for more than two decades. The monovalent adsorbates, such as AM and Ag, induce the (3×1) reconstruction (Daimon and Ino 1985), and its common origin is confirmed by similarities of LEED patterns and *I-V* curves (Fan and Ignatiev 1990; Quinn and Jona 1991), STM images (Jeon et al. 1992; Wan, Lin, and Nogami 1992; Wan, Lin, and Nogami 1993), and surface core-level shifts (SCLS) (Paggel et al. 1995; Weitering, Shi, and Erwin 1996). Several structural models, e.g., the Seiwatz chain model (Weitering et al. 1994; Sakamoto et al. 1994) and the extended Pandey chain model (Okuda et al. 1994; Erwin 1995), were discussed for the (3×1). Most of them, however, were rejected because of the inconsistency with the topmost Si atom density in the (3×1) reconstruction (4/3 ML) (Saranin et al. 1998[a]; Hasegawa et al. 1998). This density

is found to be consistent with only two plausible structures, namely the so-called double-π-bonded chain model (DπC) (Saranin et al. 1998[a,b]) and honeycomb-chain-channel model (HCC) (Collazo-Davila, Grozea, and Marks 1998; Lottermoser et al. 1998; Erwin and Weitering 1998; Kang, Kang, and Jeong 1998). Based on DFT calculations, it was established that the HCC model is energetically favored for the AM/Si(111)(3×1) and in good agreement with empty and filled-state STM (Erwin and Weitering 1998), transmission electron diffraction data (Collazo-Davila, Grozea, and Marks 1998), surface X-ray diffraction results (Lottermoser et al. 1998), SCLS (Paggel et al. 1995; Weitering, Shi, and Erwin 1996; Okuda et al. 1994; Paggel et al. 1993), and angle-resolved photoemission showing the semiconducting character of AM/Si(111)(3×1) (Sakamoto et al. 1994; Weitering, Shi, and Erwin 1996; Okuda et al. 1997). The metal coverage of (3×1) is 1/3 ML (Hashizume et al. 1993; Fukuda 1994).

The interpretation becomes more complicated in the case of divalent metal adsorbates. Similar to the case of monovalent AM and Ag, the reconstructions stabilized by AEM (Ca, Mg, Ba) on the Si(111) give rise to the (3×1) spots in LEED (Quinn and Jona 1991; An et al. 1995; Weitering 1996; Kubo et al. 1998; Saranin et al. 2000; Okuda et al. 2001) and reflection high-energy electron diffraction (RHEED) (Baski et al. 2001; Sekiguchi et al. 2001). Moreover, the filled-state STM images for AEM-adsorbed Si(111) surfaces resemble those of AM-stabilized (3×1) structures (Baski et al. 2001; Sekiguchi et al. 2001; Lee et al. 2001[a]; Petrovykh et al. 2002). However, the empty-state STM images of AEM/Si(111) show the ×2 periodicity along a row of protrusions (Kubo et al. 1998; Saranin et al. 2000; Sekiguchi et al. 2001; Lee et al. 2001[a]), which nicely correlates with an appearing of half-order LEED and RHEED streaks (Saranin et al. 2000; Okuda et al. 2001; Sekiguchi et al. 2001). In other words, these results imply the (3×2) rather than (3×1) unit cell for the AEM-induced reconstructions. Indeed, the (3×2) and c(6×2) LEED spots have been observed for the Ca/Si(111) at 100 K (Sakamoto et al. 2002). Since the Si 2p core-level spectra measured for Mg (An et al. 1995) and Ca (Baski et al. 2001) revealed the close resemblance of (3×2)-AEM and (3×1)-AM structures and the angle-resolved PES data showed similarities of surface band dispersion for (3×2)-Ba (Okuda et al. 2001), -Ca (Petrovykh et al. 2002), -Mg (An et al. 1995), and (3×1)-Li (Erwin and Weitering 1998), the HCC structure of Si substrate was adopted for AEM-adsorbed (3×2) surfaces (Sekiguchi et al. 2001; Lee et al. 2001[a]; Sakamoto et al. 2002). In particular, such suggestion was also supported by the observation of edge row structure on the boundary region of single-domain Ca-induced reconstruction (Petrovykh et al. 2002). However, a simple substitution of AM by AEM atoms in the HCC backbone should lead to the serious discrepancy arising from a valence

electron counting, since an additional electron from divalent AEM atoms should result in the odd number of electrons in the (3×1) unit cell, which is completely inconsistent with the semiconducting behavior of AEM-stabilized surfaces (Olmstead 1987; An et al. 1995; Okuda et al. 2001; Baski et al. 2001; Petrovykh et al. 2002; Sakamoto et al. 2002). In view of this discrepancy, the metal coverage of 1/6 ML was proposed for the AEM/Si(111)(3×2) reconstructions (Lee et al. 2001[a]; Petrovykh et al. 2002; Sakamoto et al. 2002), which reconciles the above-mentioned contradiction.

The other promising candidates for the stabilization of (3×2) reconstruction on the Si(111) are divalent RE metals (in particular, Yb). In previous work, the Yb atoms are found to be divalent in reconstructions induced on the Si(111), and Si 2p core-level spectra for Yb-induced 3×2 reconstruction (Wigren et al. 1993[a]) are shown to be very similar to those for Ca (Baski et al. 2001) and Mg (An et al. 1995). No plausible model for the Si structure, however, is proposed for this phase. Here we elucidate the atomic arrangement of this phase on the basis of measurements by different experimental techniques (Krachino et al. 1997[a,b]; Kuzmin et al. 2002; Kuzmin et al. 2003[b]).

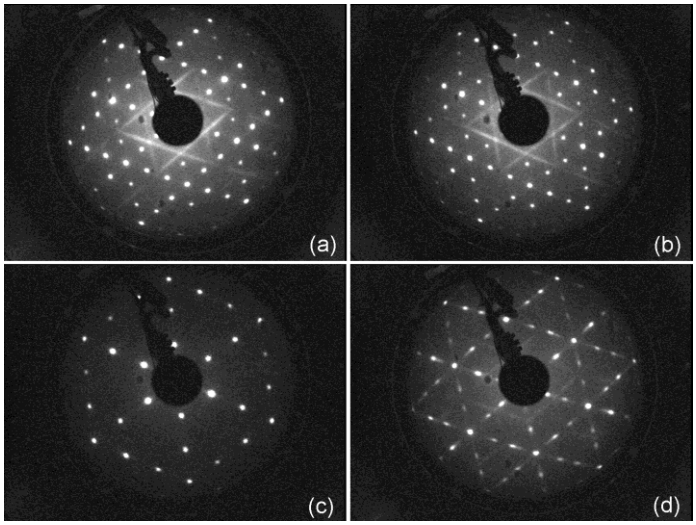

Fig. 8. (a) LEED pattern of Yb/Si(111)(3×2) at 0.17 ML. The electron energy (E_p) is 77 eV. (b) LEED pattern for the Si(111) surface stabilized by 0.1 ML Yb and 0.1 ML Eu (E_p = 75 eV). (c) LEED pattern from the (3×2) surface at E_p = 24 eV. (d) LEED pattern at 0.33 ML Yb. E_p = 68 eV. Note that (a), (b), and (d) show the half-order streaks.

The well-defined (3×1) LEED spots are observed for the Yb/Si(111) surface in the metal coverage range of 0.10 to 0.33 ML. The sharpest spots and lowest background are seen at 0.17–0.25 ML. In Fig. 8(a), we present a typical LEED pattern taken at 0.17 ML at the electron energy E_p = 77 eV. As seen, the (3×1) spots are superimposed with the half-order streaks, and no sign of (7×7) reconstruction is seen. Therefore, the surface area is completely covered with the adsorbed phase and its saturate coverage is 1/6 ML, suggesting one metal atom per six Si atoms in the (3×2) unit cell. Interestingly, the same LEED pattern can be seen when the (3×2) can be stabilized by two coexisting RE species, Yb and Eu (Fig. 8(b)), supporting the common origin of this reconstruction irrespective of adsorbate nature.

The intensities of (3×1) spots and half-order streaks depend on the energy in different manners. The former have been visible at all energies studied (from several eV to more than 150 eV), whereas the latter could be detected only within a narrow energy range (~ 60–80 eV). Such behavior can be illustrated in Fig. 8(c) where the (3×2) spots are seen, whereas the ×2 streaks are missing at E_p = 24 eV. Thus, we assume that the LEED spots and streaks arise from different substructures (constituents) of (3×2) reconstructions.

With increasing the Yb coverage, the (3×1) spots still persist at least up to 0.33 ML (Fig. 8(d)). However, the intensity of ×2 streaks strongly decreases and very faint (5×1) spots appear at this coverage. This emphasizes the difference of AM/Si(111)(3×1) and Yb/Si(111)(3×2) reconstructions: the former has the metal coverage of 1/3 ML, whereas the latter does the 1/6-ML coverage. The same (3×1) LEED spots for both reconstructions reflect a similarity of top Si atom arrangement, while the presence of ×2 streaks only for the Yb/Si(111) system suggests different structures of metal-atom network in these reconstructions. A careful analysis of Fig. 8(a) and 8(b) reveals that very weak (3×2) spots can be resolved at RT, however, the streaks remain dominating because of poor correlation of ×2 rows in the (3×2)-Yb structure. The ×2 ordering are poorer at 1/3 ML (Fig. 8(d)) than at 0.17 ML (Fig. 8(a) and 8(b)).

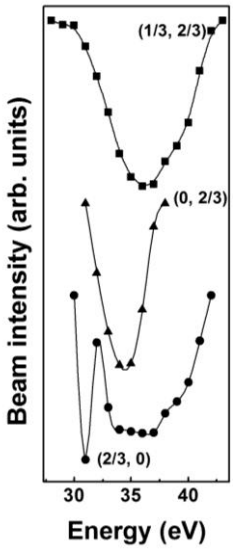

Fig. 9. *I-V* LEED curves for (1/3, 2/3), (0, 2/3) and (2/3, 0) LEED spots from the Yb/Si(111)(3×2) reconstruction. The coverage is 0.17 ML.

The intensities of some fractional-order spots in the (3×1) LEED pattern are depending on *E* non-monotonically. Fig. 9 shows *I-V* curves measured for the (1/3, 2/3), (0, 2/3) and (2/3, 0) spots in the range of 28–43 eV. The curves for the (1/3, 2/3) and (0, 2/3) indicate a minimum at 35 eV, while that of (2/3, 0) has two minima: the sharp feature at 32 eV and the other, much broader, one at 35–36 eV. These *I-V* data are in a good agreement with similar results for Li-, Na- and Ag-induced Si(111)-3×1 reconstructions (Fan and Ignatiev 1990), supporting a close similarity of Si structures in all these reconstructions.

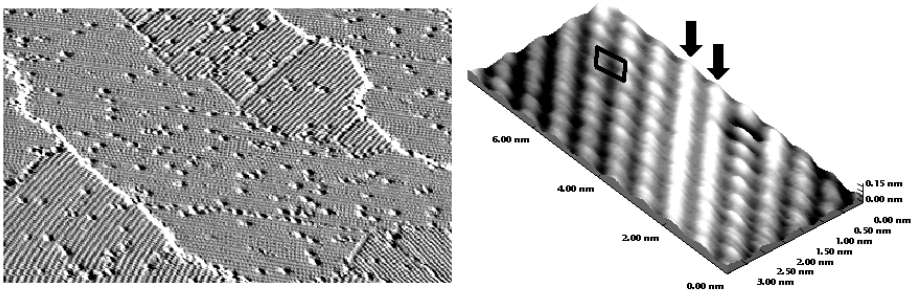

(a) (b)

Fig. 10. Empty-state STM images of Yb/Si(111)(3×2). The coverage is 0.17 ML. The bias voltage (V_S) is 1.8 V, the tunneling current (I_t) is 0.50 nA. (a) The scanning area is 81×50 nm^2. (b) A 3D view of this surface with high magnification. The (3×2) unit cell is marked, and the ×1 rows are shown by arrows (+1.8 V, 0.50 nA).

STM measurements give strong evidence that the saturate coverage of Yb/Si(111)(3×2) is 1/6 ML. An empty-state STM image (the bias voltage V_S = 1.8 V) taken at 0.17 ML is shown in Fig. 10(a). It demonstrates the presence of three equivalent, 120° rotated, (3×2) domains as well as the removal of (7×7) reconstruction of the adsorbate-free surface.

The atomic arrangement of Yb/Si(111)(3×2) can be revealed from the zoomed-in STM image in Fig 10(b). In this image rows of protrusions are associated with chains of Yb atoms. The separation between these chains is $3a_{Si}$, where a_{Si} = 3.84 Å is the unit length on the Si(111). The Yb rows are seen to have different corrugation. Some of them are made up of well-resolved ball-like protrusions and clearly demonstrate the separation of $2a_{Si}$ between the neighboring protrusions and, thus, the ×2 periodicity along a row, in agreement with the ×2 streaks in LEED. Apart from the ×2 rows, the others do not show a clear resolution along a row. Thus, the ×2 rows have a poor correlation with respect to each other, and the poor arrangement of such rows can naturally account for the finding of ×2 streaks rather than ×2 spots in LEED (Figs. 8(a) and 8(b)).

The unresolved rows are reminiscence of single-periodicity lines revealed in empty-state STM images of (3×1)-AM (Erwin and Weitering 1998; Kang, Kang, and Jeong 1998). Hence, one could assume that the respective Yb rows have the ×1 periodicity and interatomic separation of a_{Si}. That is, the (3×1) unit cell could be assigned for such an atomic arrangement. It should, however, have the 1/3 ML coverage and the metallic electronic structure, which is inconsistent with experiment. The other possible explanation of unresolved rows is thermally induced disorder of the ×2 rows. In such a case, the surface should exhibit a microscopic mixture of thermally disordered, unresolved in STM, rows and stable ×2 ones which are pinned, for example, by defects.

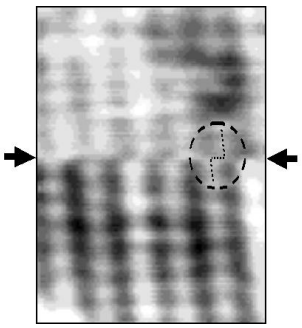

Fig. 11. A dual-polarity STM image of Yb/Si(111)(3×2) at 0.17 ML. (5.5×7.5 nm^2). V_S = 1.8 V/-1.8 V, I_t = 0.22 nA. The tip position where a sample bias reverse was applied is marked by arrow. The lateral shift caused by changing the polarity is shown inside the oval.

The brightness contrast in filled-state STM images from the Yb/Si(111)(3×2) is not so pronounced as compared to that of empty-state images. In the range of V_S from -4.0 to -1.5 V the filled-state images show up linear rows separated by $3a_{Si}$. A registry of features in both STM modes is compared in the dual-polarity image shown in Fig. 11. The tip position where the sample bias is reversed from V_S = 1.8 V (the lower half of the image) to V_S = -1.8 V (the upper half of the image) is marked by arrows. This switching-over results in a lateral shift of rows, as illustrated in Fig. 11. Thus, the STM images of Yb/Si(111)(3×2) are strongly bias-dependent and, therefore, they are contributed by not only the atomic topography but also the electronic structure effects, which makes the interpretation more complicated.

An atomic structure model of Yb/Si(111)(3×2) can be built up on the basis of experimental results described in this Subsection as well as those of Eu/Si(111)(3×2) (not shown here) ([b]Kuzmin et al. 2003). The (3×2) model (Fig. 12(a)) is derived from the HCC structure proposed for AM-induced (3×1) surfaces (Erwin and Weitering 1998). In the latter structure (Fig. 12(b)), the topmost layer of Si substrate is rearranged to form (i) the nearly planar honeycomb chains composed of four inequivalent Si atoms, *a*, *b*, *c*, and *d*, and (ii) the empty channels that accommodate 1/3 ML of metal atoms at the T_4 sites (just above a second-layer Si atom). The inner atoms of the Si honeycomb chains, i.e., the atoms *b* and *c*, form an unusual Si=Si double bond and are only weakly bonded to the underlying Si atoms *e*. The double bonds within the honeycomb chains cause an additional lowering of the energy of HCC structure. Moreover, the HCC geometry

can aptly describe the semiconducting character of AM/Si(111)(3×1) surfaces as well as the Si atom density of 4/3 ML determined for the Na/Si(111)(3×1).

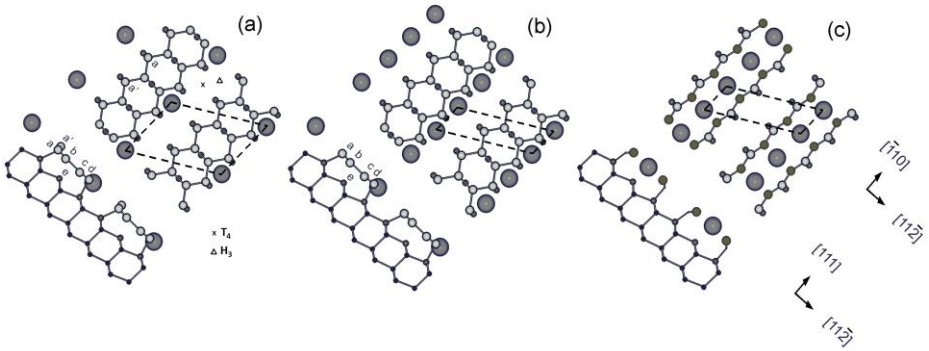

Fig. 12. Atomic structure models of Si(111)(3×*n*) reconstructions (*n* = 1, 2). (a) The (3×2) HCC model. (b) The (3×1) HCC model. (c) The (3×1) DπC model. The adsorbate coverage is 1/6 ML in (a) and 1/3 ML in (b) and (c). The large shaded circles represent metal atoms. The other circles are Si atoms. The T_4 and H_3 sites for adsorbate atoms are shown by cross and triangle, respectively.

In the case of Yb and other divalent adsorbates (such as, e.g., Eu), the reconstruction exhibits the (3×2) rather than (3×1) periodicity as well as the 1/6 rather than 1/3 ML coverage, and therefore, the HCC model needs some modification. It is assumed that the (3×2) HCC structure shown in Fig. 12(a) has almost the same Si honeycomb chain arrangement as in Fig. 12(b), but the number of metal atoms in the channels between the Si honeycomb chains is twice as low as the number of monovalent AM atoms in the (3×1) HCC structure. That is, the Yb atoms occupy every second T_4 site in the (3×2) HCC configuration, while the other T_4 sites are empty, as illustrated in Fig. 12(a). The presence of both occupied and unoccupied T_4 sites in the channels leads to a slight deformation of neighboring Si honeycombs in the equilibrium structure (not shown in Fig. 12(a) for the sake of simplicity). In particular, the left edge of the honeycomb chain exhibits a lateral corrugation, i.e., the adjacent *a* and *a'* atoms are displaced in the direction perpendicular to the chain, and the right edge exhibits a pairing of the *d* atoms due to the Coulomb interaction between the metal ion and the dangling-bond electrons of the surrounding Si atoms.

The other possible site for Yb atoms in the HCC-structure channels is H_3 (just above a fourth-layer Si atom). In such a case, similar conclusions can be made for the Yb/Si(111)(3×2) structure. Moreover, it is very difficult to distinguish

between the T_4 and H_3 sites in the HCC structure. In general, DFT calculations indicate that the energy difference between the two sites for divalent adsorbates in (3×2) HCC reconstructions is rather small, e.g., 0.01 eV/atom for Ba (Lee et al. 2003). In the case of Mg, the H_3 can be even slightly more stable than the T_4 (Hong, Lee, and Kim 2003). The energy difference of T_4 and H_3 in the Yb/Si(111)(3×2) is small as well (i.e., 0.08 eV per unit cell) (Özkaya, Çakmak, and Alkan 2010). This means that thermally induced fluctuations of Yb atoms between these two sites can occur in the (3×2) reconstruction at RT. The unresolved rows of protrusions observed in empty-state STM images can be interpreted as originating from such fluctuations. In contrast, the well-resolved ×2 rows are believed to be due to the Yb atoms at T_4 sites solely ('*frozen*' rows) and can be pinned by defects etc. Beside the T_4 and H_3, the other adsorption sites, e.g., B_2 and C_6, are less stable for the adsorbate atoms in the HCC structure (Lee et al. 2003).

The above (3×2) HCC model is able to explain well various experimental results. First, the similarity of intensity LEED *I-V* curves for the the (3×2)-Yb reconstruction and (3×1)-Li, -Na, and -Ag (Fan and Ignatiev 1990) ones seems to be quite natural and originate from the common nature of Si backbone in all these reconstructions. Some minor differences are related to the presence of ×2 periodicity in the case of Yb, however, the well-defined 3× periodicity is a signature of HCC arrangement for the whole family of these reconstructions.

Second, the Si 2*p* core-level spectra for the Yb/Si(111)(3×2) (Wigren et al. 1993[a]) are found to be similar to those of Ca (Baski et al. 2001) and Mg (An et al. 1995) adsorbates. This suggests a similar arrangement of Si substrate in these reconstructions.

Third, the electronic structure of Yb/Si(111)-(3×2), which has been studied by angle-resolved photoemission, is well explained in the framework of HCC model (Takada et al. 2006). Identified in the projected bulk-band gap are five surface states among which the dispersions of three agree well with those of the surface states of AM/Si(111)-(3×1) surfaces. The dispersions of the two other surface states agree well with those observed on the Ca/Si(111)-(3×2) surface, whose basic HCC structure is the same. On this basis, the five surface states of Yb/Si(111)-(3×2) are interpreted as being due to the orbitals of Si atoms that form the HCC structure.

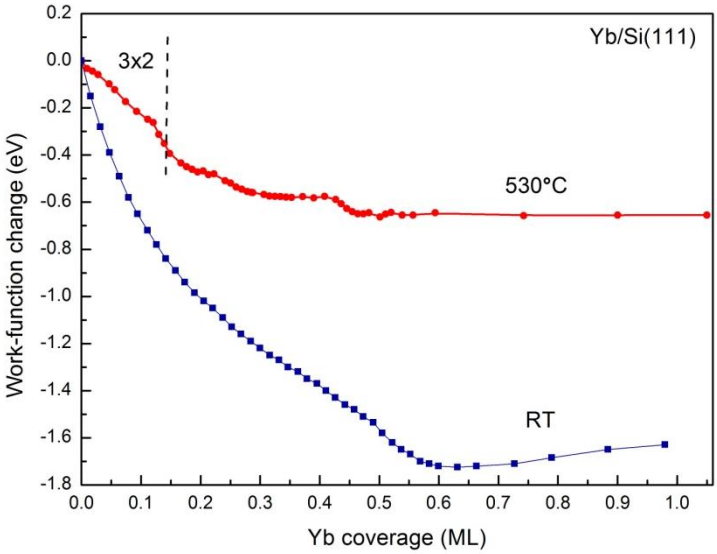

Fig. 13. Work-function change as function of metal coverage for Yb/Si(111) systems formed at RT and 530°C.

Fourth, the HCC geometry is in a good agreement with $\Delta\varphi$ measurements for the Yb/Si(111) system (Fig. 13) (Krachino et al. 1997[b]). As seen, the work function of the (3×2) HCC Yb/Si(111) surface (i.e., the curve taken for the system after annealing at 530°C) is notably higher than that of Yb/Si(111) obtained at RT at a certain Yb coverage. In general, this is because the $\Delta\varphi$ value is strongly contributed, in addition to an induced band bending, by formation of a surface dipole layer that affects the electron affinity (Lüth 2001). In the (3×2) HCC structure, the Yb atoms are located in the empty channels and have almost the same height level as the *a*, *a'*, *b*, *c*, and *d* Si atoms forming nearly the planar honeycomb chains (Fig. 12). Therefore, it is unlikely that such atomic arrangement involves a strong surface dipole moment normal to the surface plane, in contrast to the Yb/Si(111) surface at RT, where the Yb atoms are adsorbed on top of destroyed (7×7) reconstruction and the surface dipole layer can affect the work function more significantly in such a system.

Fifth, the HCC reconstruction is surprisingly stable, which can be naturally explained in terms of formation of Si=Si double bond between the *b* and *c* atoms of honeycomb chains in Fig. 12. Indeed, the TDS experiments confirm that the formation of Yb/Si(111)(3×2) is accompanied by a significant strengthening of the bonding of Yb atoms with the surface. In particular, the activation energy

required to remove an Yb atom from the (3×2) structure into vacuum is considerably higher (by more than 50%) than the desorption energy of a single Yb atom on the Si(111) (4.4 and 2.9 eV, respectively) (Krachino et al. 1997[a]). This can be understood in terms of the Si arrangement in the (3×2) HCC reconstruction. In fact, the detachment of Yb atom from the (3×2) HCC structure is expected to lead to a local transition of Si structure from the Yb-stabilized (3×2) to Yb-free high-temperature (1×1) phase, and this transition should be accompanied by the disruption of two Si=Si double bonds in the HCC structure. Hence, one can be roughly estimated on the basis of above data that the disruption of Si=Si double bond requires the activation energy of 0.75 eV. Thus, the high stability of (3×2) HCC structure is largely caused by the presence of Si=Si double bonds.

Finally, some additional STM observations should be mentioned to discuss atomistic details of Yb/Si(111)(3×2). Empty-state STM images taken for the Eu-induced Si(111)(3×2) at the low bias voltage (1.1 V) have shown extra spur-like features having the same ×2 periodicity, in addition to the bright protrusions that can be observed at both high and low bias voltages and assigned to the metal atoms (Kuzmin et al 2003[b]). Similar features have been also observed on both sides of rows related to metal atoms for the AM/Si(111)(3×1) structure and interpreted as being due to π^* antibonding states originating from Si honeycomb-chain atoms (Erwin and Weitering 1998; Kang, Kang, and Jeong 1998). Based on the registry of such features and bright protrusions for the Eu/Si(111)(3×2), it has been assumed that the RE atoms in the (3×2) HCC structure are slightly shifted from the T_4 or H_3 sites toward the [-1-12] or [11-2] direction, respectively, for the relaxation of surface structure (Kuzmin et al 2003[b]). Such a lateral shift of Yb atoms, however, is not confirmed later by DFT calculations (Özkaya, Çakmak, and Alkan 2010). In contrast, the distortion of Si honeycomb chains, which leads to the ×2 periodicity of spur-like features in STM, is well consistent with these calculations.

The other peculiarity of (3×2) HCC structure of Yb/Si(111) can be derived from the dual-polarity STM image (Fig. 11). At the first glance, it is not clear why the filled-state part of this image shows the linear rows of features, whereas the filled-state images from the (3×1) and (3×2) surfaces for other adsorbates, such as Li (Wan, Lin, and Nogami 1992; Hasegawa et al. 1998), Na (Jeon et al. 1992; Saranin et al. 1998), Ca (Baski et al. 2001; Sekiguchi et al. 2001; Petrovykh et al. 2002), and Ba (Lee et al. 2001[a]), demonstrate a typical zigzag structure due to the outer atoms of Si honeycomb chains (Erwin and Weitering 1998; Kang, Kang, and Jeong 1998). This difference of STM images can originate from the difference in adsorption sites for the metal atoms in these systems. In the case of

Yb, the *d* atoms of honeycomb chains can be screened by adsorbed atoms shifted from the T_4 (Fig. 12), while the contribution of valence 6*s* electrons of Yb atoms to the tunneling current can be rather low, as proposed for Tl on Ge(111) (Castellarin-Cudia et al. 2001). Thus, one can assume that the striped features observed for the Yb/Si(111)(3×2) in filled-state STM images are mainly associated with the *a* atoms of Si honeycomb chains. The ×2 periodicity along such features as well as the registry of filled-state and empty-state features in Fig. 11 are well consistent with the model in Fig. 12(a) and 12(b).

The other suitable model proposed in earlier studies for the (3×1) reconstruction is the DπC one (Fig. 12(c)) (Saranin et al. 1998[a,b]), as already mentioned above. As illustrated in Fig. 12(c), the DπC model implies the symmetry of metal row and two adjacent π-bonded Si chains. Clearly, such a structure is in a poor agreement with STM data described here, and therefore, cannot be adopted for the Yb/Si(111)(3×2).

Last but not least, it is worthwhile noting that the HCC structure enables to explain the insulating property of metal-adsorbed Si(111)(3×2) surface where the metal adsorbate is divalent RE and the coverage is 1/6 ML. The (3×2) unit cell provides the even number of electrons: two from RE atom, two from the *a* and a_0 atoms and six from the *b*, *c*, and *d* atoms of the Si honeycomb chain, and two from the first-layer Si atoms *e* (Fig. 12(a)). Likewise, a similar character can be found for the (3×1) HCC structure stabilized by 1/3 ML of monovalent AM atoms; the (3×1) unit cell contains six electrons donated by five Si atoms and one metal atom (Fig. 12(b)). In contrast, the (3×1) HCC structure with 1/3 ML of divalent adsorbate (RE and AEM) atoms and the (3×2) HCC structure with 1/6 ML of monovalent adsorbate (AM and Ag) atoms would fail in having the insulating electronic structure: they would have the odd number of electrons per unit cell and, therefore, the metallic rather than insulating property. Since the tendency to open a band gap between the highest occupied band and the lowest unoccupied one, i.e., to maintain the insulating electronic structure, is very common for metal/semiconductor reconstructions and one of driving forces for their formation, the Si(111)(3×1) and -(3×2) structures stabilized by 1/3 ML of divalent metal and 1/6 ML of monovalent metal, respectively, appear to be unstable. Thus, the other aspect behind the stabilization of 1/6-ML (3×2) HCC structure for various divalent adsorbates, including Yb, is the electron counting rule: the HCC geometry is stabilized by the donation of single electron from the adsorbate per (3×1) mesh irrespective of the adsorbed species. Interestingly, neither (3×1) nor (3×2) HCC reconstruction has been reported for trivalent RE adsorbates, such as, e.g., Dy, Ho, Er, and Gd. This is in full agreement with the above electron counting rule. One may predict that such metals can form a

hypothetical (3×3) HCC structure with the 1/9 ML coverage and insulating electronic structure. Nevertheless, such a structure has never been reported yet; instead, the trivalent RE adsorbates give rise to a (5×2) structure consisting of honeycomb and Seiwatz chains of Si atoms, which obeys the electron counting picture leading to a semiconducting surface-band structure (Kirakosian et al. 2002; Okuda et al. 2004; Engelhardt et al. 2006; Battaglia et al. 2007; Battaglia et al. 2008).

3.2.2. Yb/Ge(111)(3×2)

Since germanium is a group IV element like silicon, similar reconstructions can be expected for isoelectronic metal/Ge(111) and –Si(111) surfaces. Indeed, based on the surface x-ray diffraction and LEED *I-V* measurements, it has been shown that Na- and Li/Si(111)(3×1), on one hand, and Rb/Ge(111)(3×1), on the other hand, have similar bonding configurations (Lottermoser et al. 1998). Later, utilizing STM (Lee et al. 2000; Lee, Mai, and Willis 2001[b]), angle-resolved ultraviolet PES (Gurnett et al. 2009), CLPES (Gurnett et al. 2009; Lee et al. 2007), transmission electron measurements (Grozea et al. 1999), and DFT calculations (Lee and Kang 2002), the Ge(111)(3×1) reconstructions stabilized by monovalent adsorbates (Ag, Li, Na, and K) have been interpreted in terms of the HCC geometry. It has, however, remained unresolved whether the Ge=Ge double bond, similar to the Si=Si double bond, is present in the Ge HCC structure. No evidence for the antibonding π^* state originating from the Ge=Ge has been found in the STM images from Na/Ge(111)(3×1) (Lee et al. 2000; Lee et al. 2001[c]; Yoon et al. 2000). Moreover, DFT calculations (Gurnett et al. 2009) showed that the Ge=Ge does not exist on the Li/Ge(111)(3×1), and that the inner atoms of Ge honeycomb chain, which are akin to the *b* and *c* atoms in the Si HCC structure, are located asymmetrically relative to the atom *e* (see Fig. 12(b). The other theoretical study (Lee and Kang 2002) reported that the buckled nonplanar HCC configuration of AM/Ge(111)(3×1) is unstable, whereas the flat arrangement with the Ge(*b*)=Ge(*c*) double bond is favorable. Experimentally, the double bond between *b* and *c* in the Li/Ge(111)(3×1) has been confirmed by STM (Lee et al. 2000; Lee, Mai, and Willis 2001[b]). Thus, to recapitulate, the issue of the Ge=Ge double bond has still remained far from being resolved for the (3×1) HCC reconstructions.

To shed light on the HCC structure on the Ge(111) surface, we have studied Yb/Ge(111)(3×2) reconstruction (Kuzmin et al. 2007; Kuzmin et al. 2010[a]). First, we focus on the atomic structure of this surface, and then we describe electronic properties of the reconstruction.

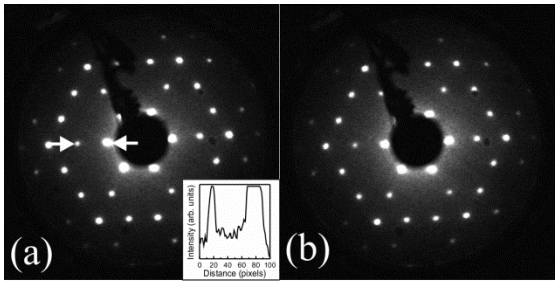

Fig. 14. LEED patterns from the the Yb/Ge(111)(3×2) surface. The coverage is 0.17 ML. The patterns are captured at (a) RT and (b) 400 °C. The electron energy is 37 eV. The inset of (a) shows the intensity profile taken along the line shown by arrows in the pattern.

3.2.2.1. Atomic structure

Similar to the case of Yb/Si(111)(3×2), the Yb/Ge(111)(3×2) has the adsorbate coverage of 1/6 ML at which the substrate becomes entirely covered with the adsorbate-induced phase. Fig. 14 illustrates LEED patterns of Yb/Ge(111)(3×2) at RT (a) and 400°C (b). Bright (3×1) spots are clearly observed, however, neither half-order spots nor streaks are found at various electron energies. The inset illustrates the intensity profile taken along the line between the neighboring fractional-order spots of the (3×1) LEED pattern shown by arrows in Fig. 14(a). It shows no sign of ×2 periodicity. Nevertheless, it will be shown later that the true periodicity of this reconstruction is actually (3×2).

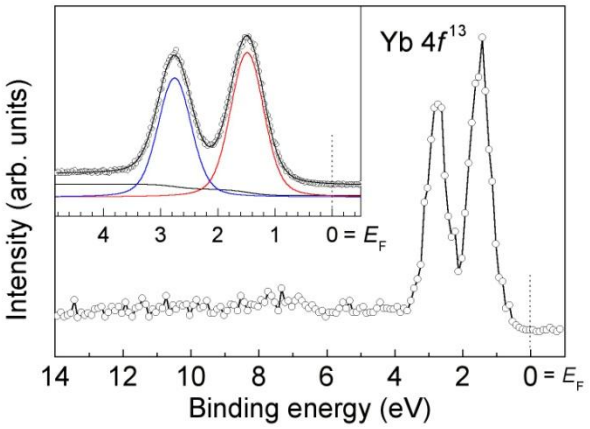

Fig. 15. Yb 4*f* spectrum of Yb/Ge(111)(3×2). The photon energy (*hv*) is 175 eV. The emission angle (θ_e) is 0°. The inset shows the fitting of Yb $4f^{13}$ final-state feature, recorded at *hv* =150 eV, by a single doublet with the Voigt functions. The background is removed by Shirley's method.

The valence state of Yb in the Ge(111)(3×2) has been determined from the Yb 4*f* photoelectron spectrum in Fig. 15, where the $4f^{13}$ and $4f^{12}$ final states related to the divalent and trivalent configurations of Yb atoms, respectively, are well separated in energy (Gerken 1983). The spectrum is measured at the normal emission angle (θ_e = 0°) and photon energy (*hv*) of 175 eV where the Yb 4*f* emission is strongly enhanced. Only a doublet of spin-orbit split peaks at the binding energies of 1.49 and 2.76 eV, which correspond to divalent Yb atoms (i.e., $4f^{13}$ final state), is found, whereas features corresponding to the Yb $4f^{12}$ final-state multiplet between 4 and 11 eV (the trivalent state) are not detected. We, therefore, conclude that the Yb atoms are completely divalent in the Yb/Ge(111)(3×2). Also, no emission is found at the Fermi level in Fig. 15 (also see below), indicating that the Yb/Ge(111)(3×2) is semiconducting, similar to the cases of AEM/ and REM/Si(111)(3×2) reconstructions.

The inset of Fig. 15 depicts the Yb 4*f* spectrum of Yb/Ge(111)(3×2) in more detail. The Yb^{2+} state can be reproduced by a single doublet of Voigt functions. The spin-orbit splitting is 1.269 eV, agreeing well with earlier fitting data (Dávila et al. 2002), and the branching ratio is 1.21, which can be somewhat different from the theoretical value (4/3) due to the diffraction effects (Yeom et al. 1998). The Lorentzian width (LW) and Gaussian width (GW) are 0.172 and 0.588 eV,

respectively. The presence of only one component in the Yb 4*f* spectrum suggests that the Yb atoms reside at equivalent (or very similar) adsorption sites in the Yb/Ge(111)(3×2). Their origin will be discussed in this subsection later.

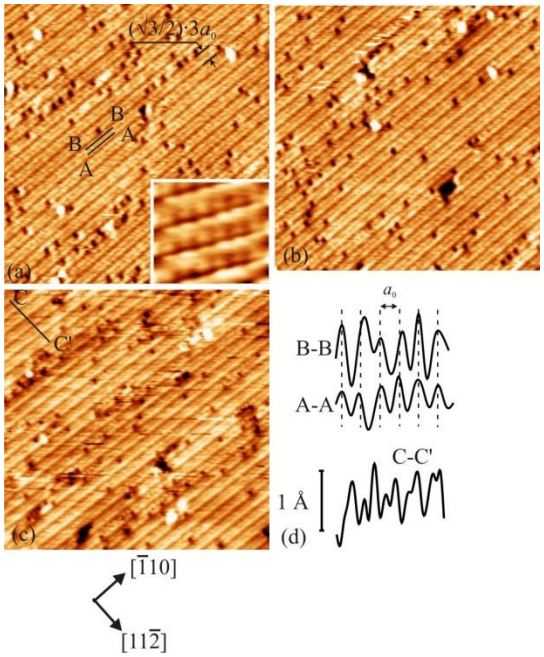

Fig. 16. Bias-dependent STM images from the Yb/Ge(111)(3×2) reconstruction in the filled states. The bias voltage (V_S) is (a) −2.32 V, (b) −1.70 V, and (c) −1.08 V. The tunneling current is (a) 69, (b) 56, and (c) 42 pA. The inset of (a) shows a high-resolution image of zigzag chain features (4.2 nm × 3.7 nm). (d) The line profiles A-A, B-B, and C-C' taken along and across the zigzag chains in (a) and (c). The vertical bar shows the scale along the (111) direction.

STM observations in filled states measured reveal double rows of protrusions on the Yb/Ge(111(3×2) (Fig. 16). The zoomed-in image taken at −2.23 V (see the inset of Fig. 16(a)) demonstrates that the maxima of double rows are arranged in zigzag chains, which is the well-established fingerprint of the HCC structure (Erwin and Weitering 1998). These maxima are associated with the dangling-bond states caused by the outer atoms of honeycomb chains, i.e., *a* and *d* in Fig. 17(a), *a*, *a'*, and *d* in Fig. 17(b), and *a*, *d*, and *d'* in Fig. 17(c).

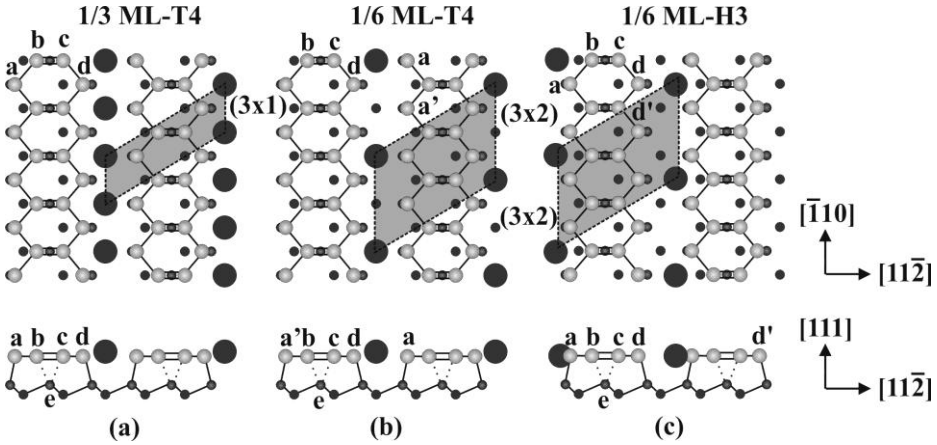

Fig. 17. HCC structures of (3×1) and (3×2) surfaces with monovalent and divalent metal adsorbates, respectively. (a) The (3×1) structure with the 1/3 ML coverage of monovalent atoms adsorbed at the T_4 sites. (b) and (c) The (3×2) structures with the 1/6 ML coverage of divalent atoms adsorbed at T_4 and H_3 sites, respectively. The metal atoms are represented by large solid circles. The (3×1) and (3×2) unit cells are shown by shadowed parallelograms.

The distance between the neighboring zigzag-chain features in the [11-2] direction in Fig. 16(a) is $\sqrt{3}/2 \times 3a_0$, where $a_0 = a_{Ge} = 4.0$ Å is the unit length on the Ge(111) surface. As shown in Fig. 16(d), the line profiles A-A and B-B taken along the two adjacent rows of the zigzag chain feature in Fig. 16(a) indicate that the distance between the neighboring protrusions in a row is basically a_{Ge}, that is, the zigzag chains have a single periodicity in the [-110] direction. A closer inspection, however, reveals that the zigzag chain features are locally slightly distorted; in particular, the neighboring protrusions tend to be grouped in pairs. Especially, the ×2 pairing effect is observed for the line profile B-B. Thus, the zigzag chain features locally show the ×2 periodicity along a chain. A similar behavior has been reported also for divalent metals, Ba (Lee et al. 2003), Ca (Sekiguchi et al. 2001), and Sm (Palmino et al. 2003) on the Si(111), and Eu on Ge(111) (Kuzmin et al. 2006[a]), and supported by calculations (Lee et al. 2003; Miwa 2005; Hong, Lee, and Kim 2003). This effect is explained by the electrostatic interaction between the metal ion and the neighboring honeycomb atoms, e.g., *d* in the (3×2) structure with T_4 adsorption sites (Fig. 17(b)). This leads to slight displacement of both *d* atoms to each other and the doubling of periodicity along the honeycomb chain (Lee et al. 2003). The distortion along the

other outer row of the honeycomb chain, i.e., along the row composed of the atoms *a* and *a'* in Fig. 17(b) is much more hardly recognized.

The further analysis of STM data in Fig. 16 shows that the filled state images of Yb/Ge(111)(3×2) are bias dependent, which is not reported for related systems earlier. The adjacent rows of zigzag chains locally have a contrast in brightness at $V_S = -1.70$ V (Fig. 16(b)). This difference becomes more pronounced at −1.08 V (Fig. 16(c)). As depicted in Fig. 16(d), the line profile C-C' taken across zigzag chains in Fig. 16(c) reveals the noticeable difference in height level of the adjacent rows of zigzag chains. It is expected that the bonding configurations and charge states of the outer Ge honeycomb atoms in the HCC structure are not identical. For example, in Fig. 17(b) the metal atom is surrounded by the two nearest-neighbor atoms *d*, while it faces the atom *a* and does not interact directly with the atom *a'*. Thus, the contrast in height level of the adjacent rows of the zigzag chain is thought to reflect the difference in bonding sites of the outer Ge honeycomb atoms. Yet, the Yb atoms can slightly move toward the row of *d* atoms in the (3×2)-T_4 or *a* atoms in the (3×2)-H_3, leading to an increase in the valence charge of these atoms. This rearrangement is possible because the shift of Yb atoms would facilitate a larger angle between the two bonds of the Yb atom and the two neighboring Ge atoms.

Another prominent quality of the images in Fig. 16 is an abundance of defects that appear as dark depressions along the zigzag chains. It is essential that such defects are distributed nonuniformly. We found that about 68% of the defects appear on the brighter row of the zigzag chain. The origin of such propensity is still unclear. We notice that a similar behavior has been reported for filled state STM images of Li/Ge(111)(3×1), where the defects are distributed along one of the two adjacent rows of the zigzag chain feature (Lee, Mai, and Willis 2001[b]). For the Yb/Ge(111)(3×2), the defects can originate from a local distortion of metal rows in the HCC channels or/and contaminations. We will discuss the origin of defects of Fig. 16 in more detail below.

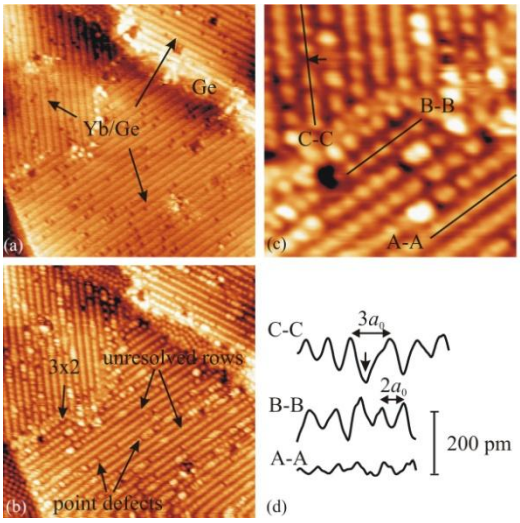

Fig. 18. (a) and (b) Filled and empty state STM images of almost the same surface area on the Yb/Ge(111)(3×2). The bias voltages are −2.32 and +2.32 V, respectively. The tunneling current is 106 pA. (c) A high-resolution empty state (V_S = +2.32 V and I_t = 106 pA) STM image with larger magnification. (d) Line profiles A-A, B-B, and C-C. The vertical bar shows the scale along the (111) direction.

The left panel of Fig. 18 shows STM images taken from almost the same surface area not simultaneously in both filled and empty states V_S = −2.32 and 2.32 V, respectively. Three equivalent, 120°-rotated, domains of (3×2) reconstruction along with a small bare Ge region are seen in these images. As described above, the filled-state image exhibits the double rows with zigzag chain features. In empty states (Fig. 18(b)), the surface shows up single rows of protrusions, where the distance between these rows is $\sqrt{3}/2 \times 3a_{Ge}$. Frequently, the protrusions in a row are clearly resolved and have the $2a_{Ge}$ separation, leading to the well-defined ×2 periodicity along a row. However, such rows have a local character. First, a poor resolution can be locally found along the rows, leading to continuous segments in Fig. 18(b). Fig. 18(c) represents a zoom-in of the image in Fig. 18(b), where the line profiles are taken along the continuous and well-resolved 2× rows A-A and B-B, respectively. Comparison of these curves reveals that the rows have a similar periodicity, which is ×2, but very different height contrast.

Second, the regularity of ×2 rows is locally broken by point defects or vacancies, appearing as dark depressions marked by arrows in Fig. 18(b). The line profile C-C taken along such a row is depicted in Fig. 18(d). It shows that the separation of the protrusions adjacent to the point defect is $3a_{Ge}$, whereas the separation of other protrusions in this row is not affected by this defect and equal to $2a_{Ge}$.

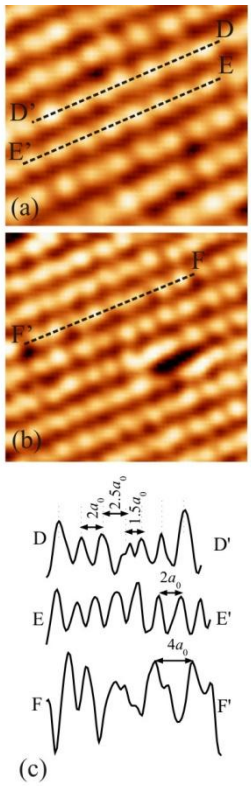

Fig. 19. (a) and (b) High-resolution empty-state STM images of Yb/Ge(111)(3×2). The bias voltage is +2.04 V. The tunneling current is 80 pA. (c) Line profiles D-D', E-E', and F-F'.

Third, the well-resolved ×2 rows can locally exhibit nonequivalent protrusions. In Fig. 19(a), the row D-D' includes a protrusion of which location is not identical to those of other protrusions. The line profile D-D' shown in Fig. 19(c) reveals that the distances between this protrusion and the two neighboring maxima in a row are $2.5a_{Ge}$ and $1.5a_{Ge}$. For comparison, the row E-E' has the

regular corrugation with the ×2 periodicity. Moreover, the presence of two nonequivalent protrusions can locally lead to the ×4 periodicity, as shown by the line profile F-F' in Fig. 19(b).

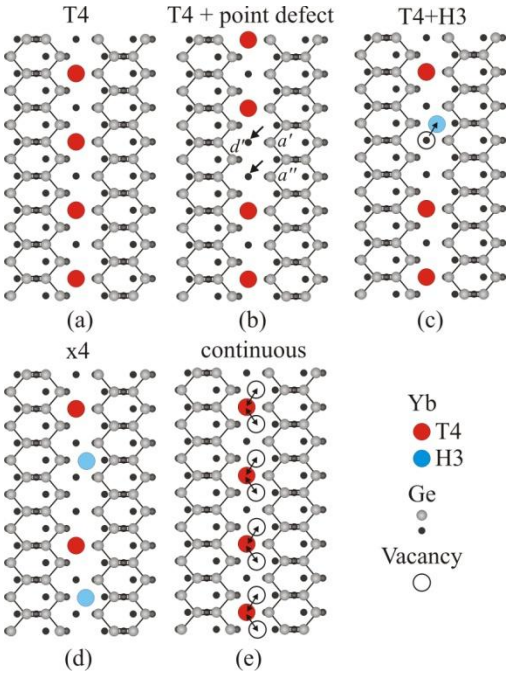

Fig. 20. Atomic models of Yb rows observed in empty state STM images of Figs. 18 and 19. For details see the text.

The registry of protrusions in the well-defined ×2 rows in empty-state images of Figs. 18 and 19 suggests that the Yb atoms reside at equivalent sites. As already discussed in Subsection 3.2.1, the most favorable sites for metal atoms in the HCC structure on both Si(111) and Ge(111) are T_4 and H_3, and the energy difference between them is very small. In Fig. 20(a), the arrangement of the ×2 row with Yb atoms on T4 sites in the channel of HCC structure is shown. (Note that such an arrangement is identical to that of metal rows in the (3×2)-T4 model in Fig. 17(b)). The ×2 row in Fig. 20(a) suggests that every second T_4 site is unoccupied. When the two neighboring T_4 sites are unoccupied (labeled by arrows in Fig. 20(b)) and thus the ×2 row is distorted, it is expected that dark depression appears in the ×2 row, which is consistent with STM images in Fig. 18, where the ×2 rows with point defects are present. It is essential that the regular ×2

periodicity of such rows is observed out the point defect, as found in Fig. 18(c). That is, the point defect leads to the shift of ×2 Yb row by a_{Ge}. Therefore, it is unlikely that the point defects are due to contamination atop the intact ×2 row. Since the location of point defects in empty state image (Fig. 18(b)) coincides with the location of dark depressions in filled state one (Fig. 18(a)), we suggest that these defects influence the Ge HCC structure, e.g., the atoms *d*, *a'*, and *a''* in Fig. 20(b). Indeed, an appearing of the point defect leads to the violation of the electron counting rule, which is required to stabilize the HCC structure, in the vicinity of this defect. Therefore, the HCC structure can be locally modified or destroyed. In Fig. 20(b) no modification the HCC structure is shown for the sake of simplicity.

In Figs. 20(c) and 20(d), modified HCC models that are able to explain the line profiles D-D' and F-F' in Fig. 19 are proposed. Shown in Fig. 20(c) is the 2× row distorted by a shift of Yb atom from the T_4 to the neighboring H_3 site, which is well consistent with the line profile D-D'. In fact, the distances between the Yb atom at H_3 and the neighboring Yb atoms at T_4 sites are about $2.5a_{Ge}$ and $1.5a_{Ge}$, in agreement with the measured protrusion separations in the line profile D-D'. The model of Fig. 20(d) proposes a regular chain of Yb atoms at T_4 and H_3, which gives rise to the ×4 periodicity along the Yb chain. We note, however, that the ×4 segments of ×2 rows are local and quite limited, and that no two-dimensional (3×4) domains were found in this study.

In the continuous rows shown in Figs. 18(b) and 18(c), a weak ×2 periodicity is found. Therefore, we assume that in these rows, the Yb atoms are adsorbed at every second T_4 site. Also, the Yb atoms can fluctuate rapidly between T_4 sites and the neighboring H_3 sites, as shown schematically in Fig. 20(e). Such fluctuation is much faster than the STM tip motion in our measurements and thus the measured STM images reflect the time-averaged picture. For this reason, we assume that the continuous rows in STM images are due to dynamical fluctuation of the Yb atoms in ×2 rows between T_4 and neighboring H_3 sites. It is important that the model of Yb row shown in Fig. 20(e) suggests the donation of the appropriate number of electrons from the Yb atoms to the surface in order to stabilize the HCC structure.

Thus, the long-range ×2 ordering along the metal rows is very limited in the Yb/Ge(111)(3×2). Most likely, this limitation explains the lack of double periodicity in LEED (Fig. 14) and the local character of the ×2 periodicity in the filled state STM images (Fig. 16). In contrast, the 3× periodicity is clearly observed in LEED and it is well consistent with the good long-range ordering of Yb/Ge(111)(3×2) in the perpendicular direction, i.e., across the Yb rows and Ge honeycomb chains. Moreover, the 3× LEED spots persist upon increasing the

temperature up to 400 °C, as found in Fig. 14(b), thus indicating that the HCC structure is stable at this temperature.

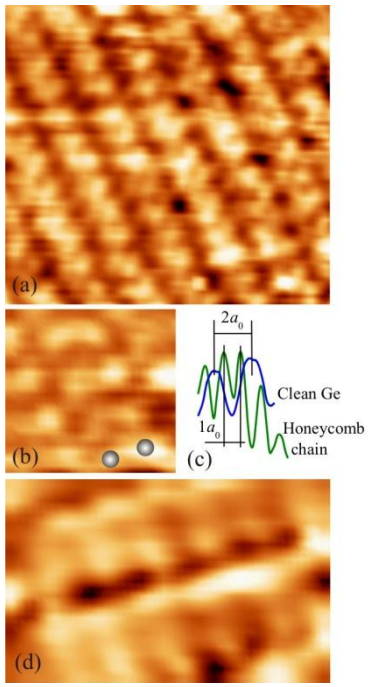

Fig. 21. Empty state STM images at lower bias voltages. (a) V_S = +1.06 V. 7.3 nm × 6.8 nm. The tunneling current is 456 pA. (b) and (d) V_S = +0.99 V. 2.4 nm × 2.3 nm and 3.9 nm × 2.5 nm, respectively. The tunneling current is 30 pA. The dimerized feature is marked in (b). (c) Corrugations of Yb/Ge(111)(3×2) and clean Ge(111)c(2×8) surfaces. The line profile for the Yb/Ge(111)(3×2) is taken along the row of dimerized features (the honeycomb chain) in lower bias-voltage STM image.

Fig. 21(a) shows an empty state STM image measured at the relatively lower bias voltage V_S = +1.06 V. The corrugation of this image is different from those of empty state images at +2.32 V (Figs. 18 and 19) and the filled state images (Figs. 16 and 18(a)). As seen in Figs. 21(b) and 21(d), high-resolution images at +1.06 V reveal rows of dimerized features. As shown in Fig. 21(c), the distance between the neighboring STM maxima along such a row (a_{Ge}) is two times smaller than the distance between the neighboring STM maxima for the Ge(111)c(2×8) surface ($2a_{Ge}$). Therefore, the structure found in Figs. 21(b) and 21(d) has the (3×1)

periodicity. The building block of this structure, i.e., the dimerized feature clearly resembles dimerlike entities caused by the Si=Si and Ge=Ge double bonds of the HCC structure in calculated empty-state STM images (Erwin and Weitering 1998; Palmino et al. 2003; Miwa 2005; Lee and Kang 2002; Hong, Lee and Kim 2005). In the case of Ge, similar features were also reported in measured empty-state images for the Li/Ge(111)(3×1) (Lee et al. 2000; Lee, Mai, and Willis 2001[b]) and Eu/Ge(111)(3×2) (Kuzmin et al. 2006[a]). Hence, we suggest that the dimerized features in the STM images of Fig. 21 are due to the Ge(*b*) = Ge(*c*) double bond on the Yb/Ge(111)(3×2), and that different structural elements of this reconstruction can be identified in STM images, depending on the bias voltage, namely, the Yb rows are mostly contributed at the higher bias voltage and the Ge=Ge double bonds at the lower bias voltage. Since the buckling of Ge=Ge double bond would lead to charge redistribution between the atoms *b* and *c*, and therefore, the asymmetry of the dimerized features in STM images, we tentatively assume that no significant buckling of this bond occurs on the Yb/Ge(111)(3×2). This is also consistent with DFT calculations (Özkaya, Çakmak, Alkan 2010). However, it should be also noted that the identification of tilted configuration of Ge=Ge by STM might be rather challenging at RT, similar to the case of the Si dimers on the Si(100)(2×1) surface.

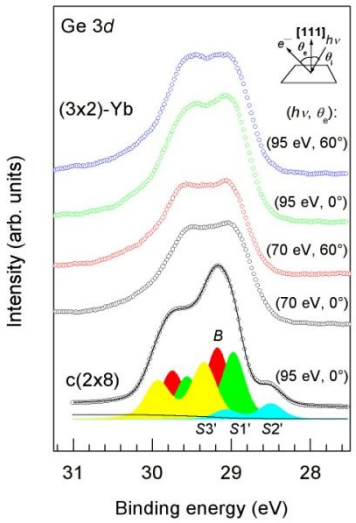

Fig. 22. Ge 3*d* spectra of Yb/Ge(111)(3×2) at various $h\nu$ and θ_e. The bottom spectrum is obtained for the clean Ge(111)c(2×8) surface at $h\nu$ = 95 eV and θ_e = 0°. This spectrum is decomposed into the bulk component (*B*) and three surface

components (*S*1–*S*3), which are represented by shadowed doublets below the raw data shown by open circles. The background (solid line) is removed by Shirley's method. At the upper right, a schematic drawing illustrates the geometry of experiment. The fitting parameters are presented in Table 2.

Table 2. Fitting parameters for the Ge 3*d* spectrum of Ge(111)-c(2×8) taken at $h\nu$ = 95 eV and θ_e = 0°. The spectrum is deconvoluted by the bulk component (*B*) and three surface components (*S*1', *S*2', and *S*3'). The spin-orbit splitting and surface core-level shifts are given in eV. The Lorentzian and Gaussian widths are in meV.

	B	*S*1'	*S*2'	*S*3'
Spin-orbit splitting	0.58			
Branching ratio	1.57			
Lorentzian width	150			
Gaussian width	265	269	275	287
Surface core-level shift	-	-0.21	-0.70	0.18

More information about the atomic structure can be obtained by Ge 3*d* surface core-level shift (SCLS) measurements. It is useful to compare Ge 3*d* spectra of Yb/Ge(111)(3×2) with those of clean Ge(111)c(2×8) surface. Fig. 22 presents normalized Ge 3*d* spectra from both surfaces measured at different experimental conditions, i.e., photon energies and emission angles in order to vary the sensitivity to the Ge surface/bulk. A spectrum from the clean surface (at the bottom of Fig. 22) is fitted by the bulk (*B*) and three surface (*S*1', *S*2', and *S*3') components. The raw data are represented by open circles and the resulting fitting curve by a solid line. The individual bulk and surface components are plotted below the raw spectrum. The decomposition was made by using a standard least-squares-fitting procedure with a linear combination of spin-orbit split Voigt functions. The background solid line below the spectrum was removed by Shirley's method. The fitting parameters are given in Table 2. The interpretation of *S*1', *S*2', and *S*3' has been thoroughly described elsewhere (Göthelid et al. 1993; Kuzmin et al. 2011[a]), and their atomic origins are pedestal first-layer atoms, half of the rest atoms, and adatoms in the c(2×8) reconstruction, respectively. As

the c(2×8) Ge structure is completely rearranged in the Yb-induced (3×2) phase, we will not consider the c(2×8) reconstruction of clean Ge furthermore.

The Ge 3*d* spectra of (3×2) are different from those of the clean surface. Even without any fitting, it is clear that a larger number of surface components are involved in the Ge 3*d* spectra of (3×2) as compared to those of c(2×8). Also, (3×2) spectra do not show a characteristic shoulder at lower binding energy, which is clearly present in the c(2×8) spectrum and caused by rest atoms (the *S*2' component). Therefore, the Yb adsorbate fully removes the c(2×8) structure, and the adsorbed phase completely covers the surface area, in good agreement well with the finding of 1/6 ML coverage for this reconstruction.

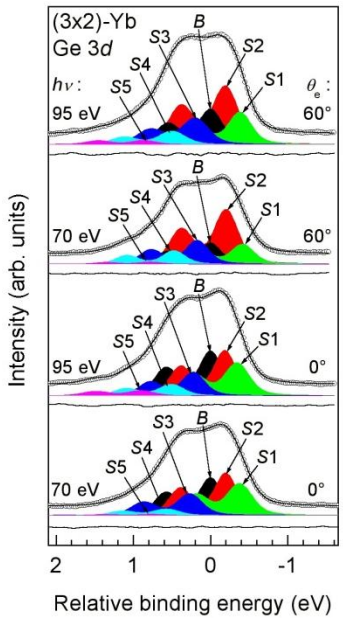

Fig. 23. Decomposition of Ge 3*d* spectra from the Yb/Ge(111)(3×2). The experimental data are shown by open circles. The fitting curves are shown by solid lines. The bulk (*B*) and surface (*S*1–*S*5) components are indicated by shadowed doublets. The residual between the experimental and fitting results is given at the bottom of each spectrum. The binding energy is referenced to the bulk component.

The deconvolution of (3×2) spectra is depicted in Fig. 23. For the adequate fitting, five surface components (*S*1−*S*5), in addition to the bulk one, are

introduced. The fitting parameters for the (3×2) spectra are given in Table 3. The *S*1 and *S*2 are shifted to the lower binding energy and the *S*3, *S*4, and *S*5 to the higher binding energy relative to the bulk component. Analyzing the relative intensities of these components, we find that the intensity of *S*5 is always quite low and ranges from *S*5/B = 0.03 at the experimental condition ($h\nu$, θ_e) = (70 eV, 0°) to 0.12 at (95 eV, 0°). We, therefore, argue that the *S*5 originates from the Ge bonding sites that do not belong to the regular (3×2) structure, while the rest surface components, *S*1−*S*4, are related to the Ge sites in the Yb/Ge(111)(3×2) reconstruction. The intensity ratios of *S*1/B, *S*2/B, *S*3/B, and *S*4/B increase upon changing the emission angle from 0° to 60°, i.e., from the enhanced bulk to surface sensitivity, as expected for the surface components. Among those, however, the behavior of *S*1 is different from the other three. In going from θ_e = 0° to θ_e = 60°, the intensity ratio of *S*1/B increases by only 10%, whereas the *S*2/B, *S*3/B, and *S*4/B ratios increase by 80–200%. We, therefore, interpret the *S*1 as arising from subsurface atoms and the *S*2–*S*4 from the topmost-layer Ge atoms of the (3×2)-Yb.

Table 3. Fitting parameters for the Ge 3*d* spectra of Yb/Ge(111)(3×2) (Fig. 23) decomposed by using the bulk component *B* and five surface components, *S*1–*S*5. The spin-orbit splitting and surface core-level shifts are given in eV, and the Lorentzian and Gaussian widths are in meV.

	B	*S*1	*S*2	*S*3	*S*4	*S*5
Spin-orbit splitting	0.58					
Branching ratio	1.60 ± 0.01					
Lorentzian width	150					
Gaussian width at $h\nu$ = 70(95) eV	265 (275)	273 (282)	0.281 (289)	289 (301)	292 (304)	290 (302)
Surface core-level shift	–	−0.19	−0.38	0.22	0.52	0.82

Next, it is worthwhile to discuss briefly the Ge 3*d* core-level data as compared to previous Si 2*p* and Ge 3*d* results for related (3×2) and (3×1) reconstructions interpreted on the basis of the HCC structure. As depicted in Fig. 24(a), the (3×1) HCC structure includes a few nonequivalent substrate atoms in the top layer, e.g., the *a* and *d* atoms bonded to metal atoms directly, and the *b* and *c* atoms which form the double bond. Therefore, one can expect that such atomic configuration causes four SCLS components originating from the topmost substrate atoms. In addition, core-level shifts can stem from the second- and third-

layer atoms, i.e., the *e*, *f*, *g*, *h*, *i*, and *j*. In fact, the DFT calculations discovered a number of SCLSs for the (3×1) reconstruction induced by Li, Na, and K on Si(111) (Gurnett et al. 2005). However, most of them are difficult to resolve experimentally because of the limited instrumental resolution. In general, two surface components were resolved in Si 2*p* spectra of AM/Si(111)(3×1). The most evident one was found at the lower binding energy relative to the bulk peak (Gurnett et al. 2005; Okuda et al. 1994). This component was assigned to the both of the two outside atoms of the Si honeycomb chain, i.e., *a* and *d* in Fig. 24(a) (Kang, Kang, and Jeong 1998; Gurnett et al. 2005). The other surface component resolved at the higher BE relative to the bulk emission was assigned to either *b* and *c* atoms (Kang, Kang, and Jeong 1998) or several Si atoms including *b* and *c* (Gurnett et al. 2005).

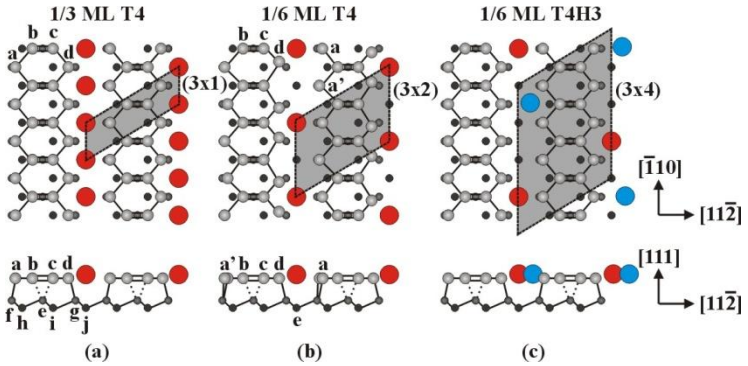

Fig. 24. Atomic configurations of (a) the 1/3 ML (3×1) reconstruction induced by AM on Si(111) and Ge(111), (b) the 1/6 ML (3×2) reconstruction induced by AEM and RE on Si(111), and (c) the 1/6 ML (3×2)/(3×4) reconstruction induced by Eu on Ge(111). The metal atoms (large circles) are adsorbed on T_4 sites in (a) and (b), and occupy both T_4 and H_3 sites in (c). The (3×1), (3×2), and (3×4) unit cells are marked.

In contrast to the 1/3 ML (3×1) structure, the (3×2) structure with a 1/6 ML coverage has one metal atom per two (3×1) surface units. Within the T_4 model (Fig. 24(b)), this leads to a difference in bonding configuration of substrate atoms on the right side of the honeycomb chain, i.e., the *a* and *a'* atoms. According to theoretical calculations and STM observations (Lee et al. 2001[a]; Lee et al. 2003; Hong, Lee, and Kim 2005; Palmino et al. 2003), the Si honeycombs of the divalent-metal-adsorbed Si(111)(3×2) are deformed, and this deformation is not equivalent for the neighboring honeycomb units. In particular, one honeycomb is

more elongated in the [11-2] direction than the neighboring ones, and the lateral displacement perpendicular to the honeycomb chain is found to occur mostly at its left edge, which is formed by the atoms *a* and *a'* in the T4 model of Fig. 24(b). Thus, the 1/6 ML (3×2) structure of the divalent-metal-adsorbed Si(111) is expected to result in different SCLSs for the outer honeycomb-chain atoms which are the *d*, *a*, and *a'* atoms in Fig. 24(b). Indeed, Si 2*p* core-level measurements, performed for Ca (Sakamoto et al. 2002), Ba (Okuda et al. 2005), and Eu (Sakamoto, Pick, and Uhrberg 2005; Kuzmin et al. 2005[a]) induced Si(111)(3×2) reconstructions, revealed two SCLS components shifted to the lower binding energy (typically, by ~0.5 and ~0.2–0.3 eV) and one SCLS component shifted to the higher binding energy relative to the bulk. Taking into account the intensity ratio and core-level binding energies of these surface components, the one with the lowest binding energy, *S*1, is assigned to the *d* atoms in Fig. 24(b), and the other component with the second lowest binding energy, *S*2, is interpreted as originating from the *a* atoms (Sakamoto et al. 2002; Sakamoto, Pick, and Uhrberg 2005; Kuzmin et al. 2005[a]) or *a* and *a'* atoms (Okuda et al. 2005). The third SCLS component at the higher binding energy relative to *B* was attributed to the *b*, *c*, and/or *e* atoms.

As for the HCC structures on the Ge(111) substrate, Ge 3*d* spectra from K- (Lee et al. 2000) and Na/Ge(111)(3×1) (Lee, Mai, and Willis 2001[b]) reveal two surface components both of which appear on the lower binding energy side. The Li/Ge(111)(3×1) surface provides only one surface component which is shifted to the lower binding energy (Lee and Kang 2002). The surface components found in the Ge 3*d* spectra from the Eu/Ge(111)(3×2) are qualitatively similar to those of Si 2*p* spectra from the Si (3×2) surfaces (Kuzmin et al. 2006[b]). However, the intensity ratios of Ge 3*d* surface components differ dramatically from those of Si reconstructions. For this reason, the atomic structure of the Eu/Ge(111)(3×2) was assumed to be different from those of AEM/ and REM/Si(111)(3×2). It suggests two distinct adsorption sites for the Eu atoms. The analysis of Ge 3*d* spectra from the Eu/Ge(111) shows that in addition to the bulk component, there are two surface-related components, *S*1 and *S*2, shifted by 0.6 and 0.2 eV, respectively, to the lower binding energy relative to *B* and one surface component, *S*3, shifted by 0.15 eV to the higher binding energy relative to *B*. In general, these results resemble the Si 2*p* fitting scheme for the divalent-metal-adsorbed Si(111)(3×2) surfaces whose atomic structure is interpreted on the basis of HCC structure with a 1/6 ML coverage of metal atoms adsorbed on T_4 sites. However, the intensity ratios of Ge 3*d* surface components for the Eu/Ge(111)(3×2) drastically differ from those of Si (3×2) surfaces and cannot be explained with the T_4 HCC model. A modified structural model is proposed for the Eu/Ge(111)(3×2)/(3×4) surface,

where half of the Eu atoms (1/12 ML) are adsorbed on T_4 and the other half on H_3, leading to the (3×4) periodicity in the so-called T_4H_3 configuration (Fig. 24(c). This model is also consistent with DTF calculations (Özkaya, Çakmak, Alkan 2010) showing that the T_4 and H_3 sites in the Ge HCC structure can be degenerate in energy.

The Ge 3*d* line shape of Yb/Ge(111)(3×2) is qualitatively different from those of Eu/Ge(111) and other (3×2) HCC reconstructions on Si(111). The Ge 3*d* spectra from the Yb/Ge(111(3×2) reconstruction include two lower binding-energy components, *S*1 with an SCLS of −0.19 eV and *S*2 (−0.38 eV), and two higher binding-energy components, *S*3 (0.22 eV) and *S*4 (0.52 eV). The *S*2, *S*3, and *S*4 are connected with the top-layer atoms and *S*1 with the subsurface atoms of the reconstruction. Since the number and SCLSs of Ge 3*d* components for the Yb/Ge(111)(3×2) is different from those of Eu/Ge(111)(3×2)/(3×4), the T_4H_3 model in Fig. 24(c) cannot be adopted in the case of Yb/Ge(111)(3×2). One candidate for the model of Yb/Ge(111)(3×2) is the HCC structure with the buckled Ge(b)=Ge(c) bond (Kuzmin et al. 2007). This model, however, is hardly consistent with STM data (Fig. 21) and supported by independent calculations (Özkaya, Çakmak, Alkan 2010). Therefore, we propose here a novel model of Yb/Ge(111)(3×2) based on the Ge 3*d* core-level data.

Since the *S*1 is a bulk rather than surface sensitive component, it is assumed that the atomic origin(s) of *S*1 is (are) Ge atom(s) which are different from those of topmost-layer (honeycomb-chain) Ge atoms. Among the other components, there are the two shifted to the higher binding energy (*S*3 and *S*4). They can be related to the inner atoms of honeycomb chains. This implies that the atomic arrangement of the Ge honeycomb is not equivalent to that of Si honeycomb chain (the inner atoms of Si honeycomb chains provide a single surface-shifted Si 2*p* component). The intensity ratio of *S*3 and *S*4 is 2:1 (note that for it should be 1:1 for the buckled Ge(*b*)=Ge(*c*) bonds). Also, the intensity ratio of *S*2 : (*S*3 + *S*4) is 4:3. Therefore, we assume that the *S*2 is contributed by the outer atoms of Ge honeycomb chains and *S*3 and *S*4 by 3/4 of the inner atoms of Ge honeycomb chains. Thus, the ×2 arrangement of Yb rows affects the inner structure of Ge honeycomb chains. Further studies are needed for further verification of such a structure.

3.2.2.2. Electronic properties

In this Subsection, we consider the electronic properties of Yb/Ge(111)(3×2) studied by angle-resolved photoemission and STS. Since this surface is triple-domain, i.e., it has three equivalent, 120°-rotated, domains, there is an ambiguity

in interpreting valence-band photoelectron spectra at finite $k_\parallel$ (where $k_\parallel$ is the momentum parallel to the surface). Nonetheless, at $k_\parallel = 0$ the contributions from three different domains are identical. For this reason, we measured valence-band spectra only at normal emission, $\theta_e = 0°$, which corresponds to the Γ symmetry point of the surface Brillouin zone (SBZ) ($k_\parallel = 0$).

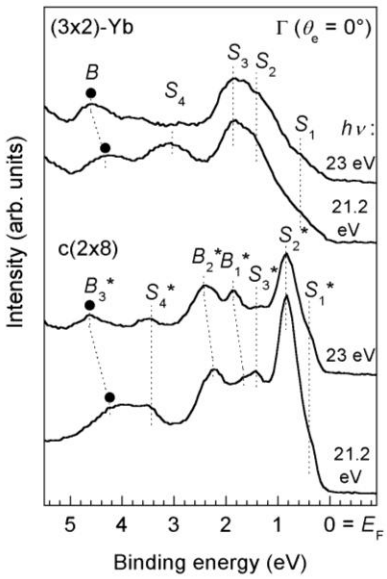

Fig. 25. Valence-band spectra of Ge(111)c(2×8) and Yb/Ge(111)(3×2) at θ_e = 0° and $h\nu$ =21.2 and 23 eV. The bulk- and surface-related states are denoted by "*B*" and "*S*", respectively.

Fig. 25 presents the spectra measured by VBPES at $h\nu$ = 21.2 and 23 eV and θ_e = 0° for the clean Ge(111)c(2×8) and Yb-adsorbed Ge(111)(3×2) surfaces. For the clean surface, several emission features labeled *S*1*–*S*4* and *B*1*–*B*3* are found. Since none of these features lie in the band gap at the Γ point (Chelikowsky and Cohen 1976), they cannot be directly assigned to surface states. However, some of the features were identified as surface states in earlier studies (Bringans and Höchst 1982; Yokotsuka et al. 1984; Wachs et al. 1985; Nicholls et al. 1986; Bringans, Uhrberg, and Bachrach 1986; Aarts, Hoeven, and Larsen 1988). In particular, the peak *S*2* at 0.85 eV below E_F, which is the dominant feature in both of the c(2×8) spectra, agrees well with those studies, where it was assigned to the rest-atom dangling bond surface state. The feature *S*3* at the binding energy of 1.4 eV was also observed earlier. It was connected with the

adatom back-bond surface state. Moreover, the weak shoulder *S*1* is due to the back-bond surface states localized in the first layer, with some weight in the second layer, as revealed by *ab initio* calculations (Takeuchi, Selloni, and Tosatti 1992). The energy positions of *S*1*, *S*2*, and *S*3* do not change at $h\nu$ = 21.2 and 23 eV, supporting their surface-related character.

Regarding the other features in the c(2×8) spectra, most of them are related to bulk bands because such features were found to persist upon an exposure of atomic hydrogen (Yokotsuka et al. 1984). In fact, the *B*1*, *B*2*, and *B*3* are dispersive at $h\nu$ =21.2 and 23 eV, and therefore, they are suggested to be due to the direct bulk transitions. In contrast, the *S*4* can be related to the surface structure, e.g., surface resonance or umklapp process. A similar feature was found previously, where it disappeared upon an exposure of atomic hydrogen (Yokotsuka et al. 1984).

For the Yb/Ge(111)(3×2), the valence-band spectra are drastically changed. As illustrated in Fig. 25, the spectrum at $h\nu$ = 21.2 eV shows at least five features at binding energies of 0.55, 1.5, 1.85, 3.1, and 4.3 eV (labeled *S*1, *S*2, *S*3, *S*4, and *B*, respectively). The *S*1, *S*2, and *S*3 have the same binding energies at two photon energies ($h\nu$ = 21.2 and 23 eV) and are not observed for the clean surface. We, therefore, assume that the *S*1, *S*2, and *S*3 are related to surface states of Yb/Ge(111)(3×2).

In contrast, the *B* corresponds directly to the bulk feature *B*3* of the clean surface. The *S*4, which can be readily identified in the spectrum at $h\nu$ =21.2 eV but not in the spectrum at $h\nu$ =23 eV, does not show a one-to-one correspondence with the clean surface. Most likely, this feature is due to the second-order light ($h\nu$ = 42.4 eV) and is related to the Yb $5p_{3/2}$ core level.

The other technique to study the electronic structure of surfaces is STS. Whereas the angle-resolved VBPES allows the identification of electronic structure below the Fermi level and photoelectron spectra are contributed by emission from both the surface and the bulk, STS probes the electronic structure both below and above the Fermi level and contributed mostly by states associated with uppermost atomic layers of the sample. Moreover, another difference is that in photoemission the information is usually collected and averaged from the relatively large surface area (~1 mm), while STS is a local probe and provides the information on the atomic scale. For this reason, STS can be utilized to get insight into the local electronic structure of Yb/Ge(111)(3×2). To this end, we measured normalized conductance spectra $(dI/dV)/(I/V)$ for the clean and Yb-adsorbed surfaces. Such spectra reflect the spatial variation in the local density of states and the energy positions of surface bands. However, the intensity of peaks in the

spectra depends strongly on the tip-substrate configuration and the normalization procedure (Tersoff and Hamann 1983; 1985).

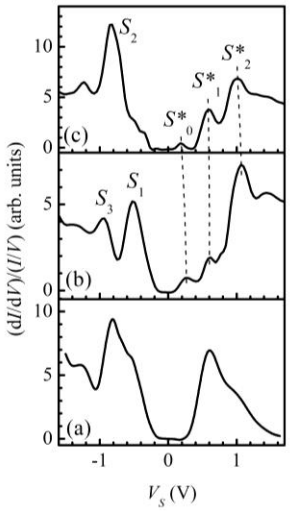

Fig. 26. Normalized conductance spectra taken from (a) the clean Ge(111)c(2×8) surface, and (b) the Yb row and (c) Ge honeycomb chain of Yb/Ge(111)(3×2) reconstruction.

Fig. 26(a) shows a normalized conductance spectrum from the clean substrate. The 0-V bias voltage corresponds to the Fermi level. In occupied orbitals the curve reveals a pronounced feature at −0.80 eV and a shoulder at −0.57 eV. These states are due to the two nonequivalent rest atoms in the c(2×8) reconstruction and their energy splitting agrees well with the predicted value (Takeuchi, Selloni, and Tosatti 1992). In unoccupied orbitals a peak at +0.61 eV and an extended shoulder around 1.0 eV are present. They can be attributed to the adatom dangling-bond states (Takeuchi, Selloni, and Tosatti 1992). The tunneling gap is 0.40–0.45 eV, and the valence-band maximum is located 0.17 eV below the Fermi energy, in good agreement with earlier observations (Guichar, Garry, and Sébenne 1979; Feenstra et al. 2005).

Normalized conductance spectra for the Yb/Ge(111)(3×2) reconstruction are represented in Figs. 26(b) and 26(c). They are taken over the Yb rows and Ge honeycomb chains, respectively. For each of these spectra, the *I-V* curve (not shown here) is an average of about 20 individual spectra taken for the respective structural unit. No significant difference is found for those of continuous and 2×

rows of Yb atoms. It is intuitively understood on the basis of the similarity of the electronic structures of the HCC configurations with T_4 and H_3 sites, as described below. In the occupied states, the spectrum of Yb rows (Fig. 26(b)) clearly shows two features, S_1 and S_3, at −0.51 and −0.95 eV, respectively, whereas the dominant feature in the spectrum of Ge honeycomb chain (Fig. 26(c)) is a peak S_3 at −0.83 eV. In the empty states, the dominant feature of the spectrum of Yb rows is a peak S_2^* at 1.06 eV. Besides, two minor features S_0* and S_1* at 0.27 and 0.61 eV, respectively, are seen. In the spectrum of Ge honeycomb chain, the S_1^* and S_2^* are clearly resolved at 0.60 and 1.02 eV, respectively. The S_0^* is also found at 0.18 eV. Thus, the spectra of Yb rows and Ge honeycomb chain are rather different, allowing the identification of observed states. The tunneling gap is 0.25–0.30 eV for the Yb rows and about 0.35 eV for the Ge honeycomb chain. This is consistent with the photoemission data in Fig. 25, which indicate the semiconducting character of Yb/Ge(111)(3×2) reconstruction.

Previously, the band-structure calculations performed for the (3×1) HCC structures induced by Tl on Ge(111) showed that the results for two configurations where the adsorption site is either T_4 or H_3 are very similar (Hatta et al. 2008). Each of the two models includes three fully occupied surface bands and two completely empty bands lying in the projected bulk band gap. For example, in the HCC-T_4 model shown in Fig. 24(a) one of the three occupied bands labeled S_a has a bonding character between the dangling bonds of the Ge *a* and metal atoms. The other two bands, S_{bc} and S_d, have a strong bonding character between the dangling bonds of Ge atoms *b* and *c*, and a hybridized character of the dangling bond of Ge *a* and a back bond of Ge *a* with the substrate atom, respectively. The unoccupied bands, U_{bc} and U_{Tl} have the antibonding character between *b* and *c*, and mostly the metal atom and the Ge *d* and *c*, respectively. It is important that the S_{bc} and the respective band S_{bc} in the HCC-H_3 model have almost similar dispersion and binding energies, that is, the adsorption site of metal atoms in the HCC-T_4 and HCC-H_3 models does not affect noticeably the bonding between the inner honeycomb atoms *b* and *c*. Moreover, the differences of the dangling-bond states of the outer honeycomb atoms *a* and *d* and the unoccupied states in the HCC-H_3 and -T_4 models are not significant. Therefore, we expect that the charge distributions and normalized conductance spectra for the metal rows with T_4 sites (i.e., ×2 rows) are similar to those of T_4 and H_3 sites (i.e., continuous rows).

Based on the above data, we interpret our STS results as follows. The possible origin of S_1 and S_3 features, which are identified for the Yb rows, are assumed to be the states associated with the dangling bonds of the outer Ge honeycomb atoms that surround the Yb atom, i.e., *a* and *d*. In contrast, the S_2 is

identified for the Ge honeycomb chain, and therefore, it is natural to assign this feature to the inner atoms of Ge honeycomb chains. It is also worth noting that the S_2 lies between the S_1 and S_3, in agreement with the calculations (Özkaya, Çakmak and Alkan 2010).

Above the Fermi level, the S_2^* state is dominant in the curve for the Yb rows. Therefore, we assume that it has an antibonding character of the bond between the Yb atoms and outer Ge honeycomb atoms. The S_1^* state, which is clearly found for the Ge honeycomb chains but not for the Yb rows, is suggested to have an antibonding character for the *b* and *c* atoms. Thus, the energy splitting of the bonding and antibonding bands for the Ge=Ge double bond in the Yb/Ge(111)(3×2) reconstruction is 1.43 eV within the above picture. It is important that the interpretation of S_1^* and S_2^* agrees with STM observations. That is, the Yb atoms clearly contribute to STM images at higher bias voltages (typically at 2.0–2.3 V) and the inner Ge honeycomb atoms contribute to those of lower bias voltages (typically about 1.0 V).

It is more difficult to assign the S_0^* state. No additional unoccupied band was found in calculations for the (3×1) HCC structure and (3×2) one. However, the (3×2) HCC structure involves the additional bonding site for the honeycomb atoms (i.e., *a'* in the HCC-T_4 of Fig. 24(b) and *d'* in the HCC-H_3 of Fig. 24(c) that does not interact with the metal atoms and, in principle, can be the origin of S_0^*.

3.2.3. Yb/Si(111)(*n*×1) (*n* = 5, 7, 9, and 2)

While the (3×1) and (3×2) structures induced by various metal adsorbates on the Si(111) at 1/3 ML and 1/6 ML, respectively, are rather well understood, less is known about more close-packed structures formed by AEM and RE adsorbates at higher coverages. Beyond the (3×2) reconstruction, two intermediate phases, (5×1) and (7×1), followed by the (2×1) end phase at 1/2 ML have been found in order of increasing the metal coverage on the Ca/Si(111) surface (Baski et al. 2001; Sekiguchi et. al. 2001; Sakamoto et al. 2002). Based on STM and Si 2p core-level measurements, the structural models of (*n*×1) intermediate phases have been suggested to consist of honeycomb chains and Seiwatz chains with an appropriate proportion, and that of (2×1) phase is constructed by the Seiwatz chains, with Ca atoms forming the ×1 rows in the channels in between these Si chains (Baski et al. 2001; Sekiguchi et. al. 2001). Later, the double periodicity has been reported for the Ca-induced 5×1, 7×1, and 9×1 intermediate phases at low temperature, and the model of 5×‘‘2’’ reconstruction with the adsorbate coverage of 0.3 ML has been proposed (Sakamoto et al. 2002). The RE adsorbates (Sm and Yb (Wigren et al. 1993[b]) and Eu (Krachino et al. 2001)) stabilize similar (5×1)

and (7×1) periodicities on the Si(111) at intermediate coverages. At the highest coverage, Sm forms a complex (√3×√3) R30°-like structure, whereas the series of Yb and Eu stabilized structures are terminated by the 2×1 phase. Intuitively, the distinction was associated with the different valence of these RE adsorbates ; in particular, in contrast to complete divalence of Yb in all (*n*×1) reconstructions, both divalent and trivalent Sm atoms appeared in the √3 phase (Wigren et al. 1993[b]), but the formation mechanism and atomic arrangement of RE-induced intermediate and end reconstructions remain so far under debate.

Here we present the structural and statistical analysis of Yb-induced (*n*×1) structures (Kuzmin et al. 2004[c]). As already mentioned, a series of LEED patterns can be observed for the Yb/Si(111) system, in particular, (5×1), (7×1), and (2×1) ones in order of increasing the Yb coverage beyond the lowest-coverage (3×2) structure. The coverage ranges for the (5×1), (7×1), and (2×1) have not been determined precisely because of significant overlaps of LEED patterns. This means that the coverage intervals where pure LEED patterns can be found are rather narrow. This is especially the case for the intermediate (5×1) and (7×1) structures.

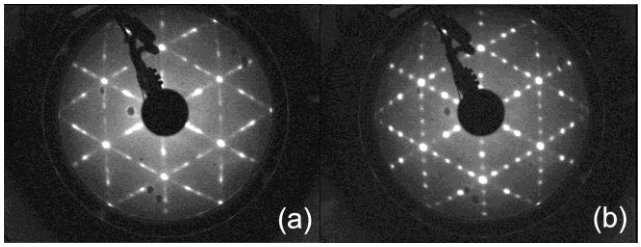

Fig. 27. LEED patterns from the Yb/Si(111) surfaces. (a) The coverage is 0.34 ML. Two structures, (3×2) and (5×1) are coexisting. The electron energy E_p = 63 eV; (b) The coverage is 0.40 ML. E_p = 60 eV. Only the (5×1) pattern is observed.

Fig. 27 exemplifies LEED patterns at 0.34 and 0.40 ML. At the former coverage superimposed patterns of two structures, (3×2) and (5×1), are found. The coexisting fractional-order (3×1) and (5×1) spots are oblong, indicating that the dimensions of domains with 3× and 5× periodicities are limited in one direction. Further, it will be clearly seen from STM results that this is due to a mixture of structural units of these phases. The coexistence of two phases, (3×2) and (5×1), at 1/3 ML also implies that the (3×1) HCC structure with the 1/3 ML

coverage does not form on the Yb/Si(111) surface, which is well consistent with the electron counting rule discussed in Subsection 3.2.1.

Fig. 27(b) illustrates the pure (5×1) LEED pattern taken at 0.4 ML of Yb. It exhibits no sign of adjacent (3×1) and (7×1) structures, and therefore, the surface is mostly covered by the (5×1) phase at this coverage. The pattern is qualitatively very similar to that reported for the Ca/Si(111)-(5×''2'') reconstruction (Sakamoto et al. 2002). The 2× periodicity was assigned to this reconstruction due to dim diffuse spots of which positions correspond to the ×2 spots of (5×2) and c(10×2) structures. For the Yb/Si(111)(5×1), the possible ×2 periodicity will be examined later by STM. Note that the dim diffuse spots contribute to the intensity of neighboring 1/5-order spots which, as seen in Fig. 27(b), have the increased brightness. A similar brightness modulation was also found for the other (n×1) intermediate LEED patterns (e.g., (7×1)) in the Yb/Si(111) system.

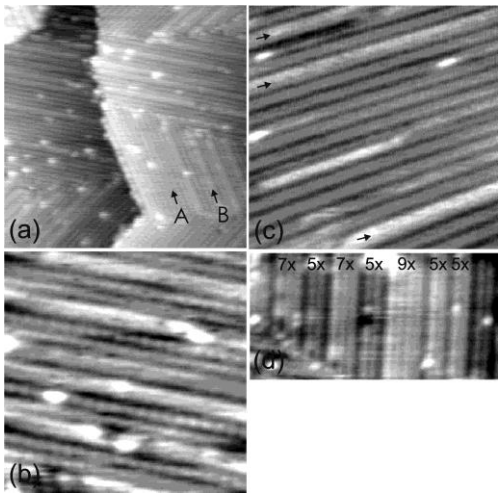

Fig. 28. STM images of Yb/Si(111) at 0.34 ML (a, b), 0.4 ML (c), and 0.5 ML (d). (a) V_S = 2.0 V, I_t = 0.2 nA, 37 nm × 37 nm; (b) V_S = 2.0 V, I_t = 0.2 nA, 12 nm × 12 nm; (c) V_S = 1.5 V, I_t = 0.4 nA, 15 nm × 15 nm; (d) V_S = 1.8 V, I_t = 0.14 nA, 24 nm × 8.5 nm. In (a) the 3× and 5× stripes are labeled A and B, respectively. In (c) the Yb layer basically shows the 7× stripes. In (d) three structures, (n×1) with n = 5, 7 and and 9, are microscopically mixed.

Fig. 28(a) shows the large-scale STM image of the Yb/Si surface at 0.34 ML. In this image, three 120°-rotated domains are formed by parallel stripes of two types (marked by A and B), which are mixed in a microscopic way. The stripe

length is only limited by domain sizes and no meandering occurs. The high-magnification STM image in Fig. 28(b) shows that narrower stripes (the type A) are the single rows of protrusions with the inter-row spacing of 3*b* (where $b = \sqrt{3}/2a_{Si}$). The brightness along the single rows is frequently modulated by 2*b*, but the single periodicity can be also found. The single periodicity of such rows can be due to thermally induced disorder of ×2 rows, as discussed for the (3×2) structure. As also seen in Fig. 28(b), the B-type stripes consist of two adjacent ×1 rows having the 2*b* inter-row separation. It is known that the ordered arrangement of ×1 rows alternately separated by 3*b* and 2*b* can be interpreted with the (5×1) structure (Wigren et al. 1993[b]). Therefore, the overall 0.34 ML Yb/Si surface represents the statistical mixture of local (3×2) and (5×1) periodicities. The areas of regular 3× and 5× periodicities are in fact very limited in the direction perpendicular to the metal rows, which is well consistent with LEED observations (Fig. 27(a)).

At 0.4 ML of Yb the proportion of 3× and 5× stripes changes drastically. As shown in Fig. 28(c), the latter become dominating and their regular array can be found on a relatively large area. Obviously, this agrees with an appearing of sharp (5×1) LEED spots and disappearing of (3×1) ones at this coverage (Fig. 27(b)). Beside the 5× stripes, the additional 7×, 9× etc. stripes, which are composed in a similar manner and consist of three, four and more ×1 rows with the 2*b* inter-row separation, can be observed locally in STM images at 0.4 ML, suggesting the formation of local 7×1, 9×1 etc. phases.

Table 4. The characteristics of odd-order intermediate Yb/Si(111) structures. The saturate coverage is evaluated assuming that the Yb rows have the actual ×1 periodicity. 'H' is the honeycomb chain and 'S' the Seiwatz chain.

Phase	**Inter-row spacing**	**Saturate coverage (ML)**	**Structural unit**
(5×1)	…3*b*2*b*…	0.40	HS
(7×1)	…3*b*2*b*2*b*…	0.43	HSS
(9×1)	…3*b*2*b*2*b*2*b*…	0.44	HSSS
…	…	…	…
(*n*×1)	…3*b* *m*×2*b*… *m* = (*n*-1)/2 - 1	(*n*-1)/2*n*	H *m*×S, *m* = (*n*-1)/2 - 1

In Fig. 28(c), the occasional 7× stripes are shown by arrows. The characteristics of odd-order intermediate reconstructions are summarized in Table

4. All of them are basically composed of ×1 rows with the n×1 unit cell comprising one 3b inter-row separation and m× 2b separations, where $m = 1/2 \times (n - 1) - 1)$. For example, the 7×1 unit includes the 3b, 2b and 2b inter-row separations, the (9×1) unit the 3b, 2b, 2b and 2b separations, etc. It is interesting that in STM images, the n× structures (n = 5, 7, ...) do not reveal any sign of ×2 periodicity along the metal rows, which can be expected from LEED observations, as discussed above.

Upon increasing the Yb coverage, the mixture of 5×, 7×, and other striped structures becomes more noticeable. In Fig. 28(d), the high-magnification STM image taken for the Yb/Si(111) at 0.5 ML demonstrates the co-existence of 5×, 7×, and 9× stripes. Providing that the protrusions in empty-state STM images are associated with Yb atoms and the metal rows has the ×1 periodicity (note that the resolution was not sufficient to resolve single protrusions along such rows), the saturate coverages for the 5×1, 7×1, and 9×1 structures are evaluated to be very similar (see Table 4), allowing the co-existence of different odd-order stripes in the same coverage ranges. To recapitulate, the STM results show that the structural units of (n×1) reconstructions, i.e., different n× stripes are microscopically mixed on the Yb/Si(111) surface at >1/6 ML, with the correlation length across the stripes being rather short (usually only a few unit cells). This proposes that the Yb rows, in general, are rather weakly correlated, leading to several, microscopically mixed, local periodicities.

3.2.3.1. Structural analysis

As shown above, the odd-order (n×1) intermediate and (2×1) end structures stabilized by Yb on the Si(111) are due to different assembling of the ×1 rows arranged with a variable inter-row spacing (either 3b or 2b). For example, the fivefold periodicity is accommodated by the ×1 rows separated alternately by 3b and 2b with the ratio of 1:1, the sevenfold periodicity by the rows separated by 3b, 2b, and 2b with the ratio of 1:2, and so on. Being the most close-packed structure, the (2×1) endpoint phase is arranged by the ×1 rows separated only by 2b. Such row combinations are quite similar to those on the Ca/Si(111) surface (Baski et al. 2001; Sekiguchi et. al. 2001). Therefore, we suggest that the striped Yb/Si(111) reconstructions can be described on the basis of HCC and Seiwatz chain models with different proportion of Si honeycomb (H) and Seiwatz (S) chains (see Table 4). Note that the lowest-coverage (3×2) and higher-coverage (2×1) endpoint phases have the zero density of S and H chains, respectively. Thus, the transition from the (3×2) to the (2×1) surface occurs via substitution of the H chains by the S chains through the intermediate phases including the both in different

proportions. In this sense, the (n×1) (n = 5, 7, 9, ...) unit cells, geometrically, are mixtures of (3×1) and (2×1) subunits. In order to illustrate the atomic arrangement of these reconstructions, we present a structural model for the (5×1)/(5×‘‘2’’) phase (Fig. 29). The unit cell of this reconstruction includes one H chain and one S chain, and therefore, the structural unit of 5× phase can be referred as to HS one. The adsorption sites of Yb atoms sitting in the empty channels can be assigned by comparison of the 3× and 5× stripes shown in Fig. 28(b). A closer inspection of this figure reveals that the registry of STM protrusions associated with Yb atoms in empty states appears to be the same for the both subunits, and therefore, we can assume that the adsorption sites of metal atoms are identical as well. It has been earlier proposed that in the (3×2) HCC structure the Yb atoms occupy T_4 (or H_3) sites or they are slightly shifted from such a site towards the adjacent Si honeycomb chains (Subsection 3.2.1). Hence, similar sites can be assumed for the Yb/Si(111)(5×1) reconstruction, too.

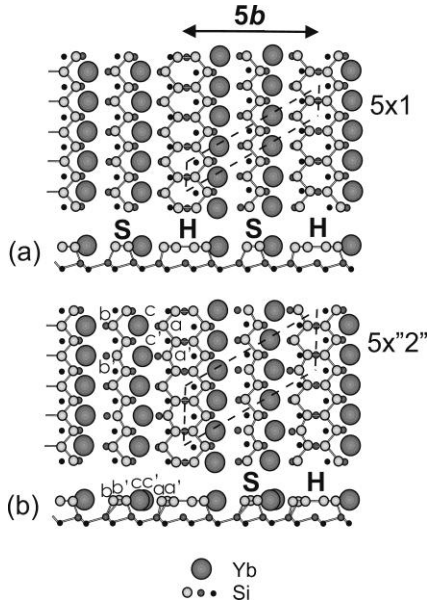

Fig. 29. (a) The atomic model of (5×1) reconstruction. The unit cell is shown by dot line parallelogram. The honeycomb and Seiwatz chains are labeled H and S, respectively. (b) The atomic model of (5×2) reconstruction. The deformed H and S chains and Yb rows include six inequivalent atoms (*a*, *a*’, *b*, *b*’, *c* and *c*’, respectively). The (5×1) and (5×2) unit cells are given by dot lines.

A structural model is illustrated in Fig. 29(a). The metal atoms are slightly displaced from T_4 to the neighboring honeycomb and Seiwatz chains. Further, an intriguing issue is the periodicity along the Yb rows. As the STM resolution was not enough to resolve individual protrusions in this direction, a single periodicity is proposed earlier (Wigren et al. 1993[b]). In other words, the Yb atoms are separated by a_{Si} along a row. Thus, the (5×1) unit cell contains two Yb atoms which reside at equivalent adsorption sites, as shown in Fig. 29(a). However, this is inconsistent with a semiconducting electronic structure of Yb/Si(111)(5×1) (Wigren et al. 1993[b]), and moreover, a similar arrangement implies the odd number of electrons per unit cell (i.e., a metallic character) for all odd-order (n×1) reconstructions. At the same time, the Yb/Si(111)(7×1) reconstruction is also found to be semiconducting (Wigren et al. 1993[b]). This serious discrepancy can be reconciled by assignment of the ×2 periodicity to Yb rows, as predicted from LEED results above. As mentioned before, the model of (5×2) reconstruction with the ×2 periodicity along the Ca rows and the adsorbate coverage of 0.3 ML (i.e., one and half Ca atoms per 5×1 subunit) was proposed for the Ca/Si(111) (Sakamoto et al. 2002). However, in the case of Yb this model does not enable to account for STM and LEED data, and therefore, it cannot be adopted for the Yb/Si(111) system. In fact, the deposition time required to saturate the Yb/Si(111)(5×1)/(5×'2') structure should be, according to our LEED experiment, approximately 2.4 times higher than that of Yb/Si(111)(3×2). Therefore, if the former structure had the coverage of 0.3 ML, the latter would be basically saturated at 0.125 ML, which is not the case. In other words, if the Yb/Si(111)(3×2) structure has the 1/6 ML coverage, the saturate coverage of 0.3 ML for the Yb/Si(111)(5×1)/(5×'2') is clearly underestimated.

Moreover, it is questionable why such a ×2 periodicity, e.g., the $2a_{Si}$ separation between Yb atoms in a row has never been observed for the intermediate structures by STM even though the thermally induced distortion of some metal rows is possible. Therefore, we assume that the Yb rows do have a single ($1a_{Si}$) spacing between the adsorbate atoms in a row in the odd-order intermediate structures, and therefore, the (5×1) unit cell includes two Yb atoms. The one-electron picture discrepancy can be alternatively eliminated by the assignment of ×2 periodicity to the Si substrate structure (and, as a result, to some Yb rows). This modification can, as one of possible structural arrangements, involve deformation of every second honeycomb due to slight displacement of Si atom a', as compared to the equilibrium position of Si atom a in the adjacent intact honeycomb (Fig. 29(b)). Then, the Yb/Si(111)(5×1) actually has the (5×2) periodicity and obeys the electron counting rule, i.e., it has a semiconducting character. Perhaps such relaxation can be driven by lowering the symmetry to

minimize the surface energy. Note that the deformation of every second Si honeycomb was earlier found in the (3×2) reconstructions stabilized by Ba (Lee et al. 2001[a]; 2003), Yb and Eu (Kuzmin et al. 2003[b]), and Sm (Palmino et al. 2003). It cannot be also excluded that similar structural distortion occurs in Seiwatz chains or/and even atomic rows of Yb, as proposed in Fig. 29(b). In the distorted configuration, one expects an appearing of six inequivalent atoms *a*, *a*', *b*, *b'*, *c* and *c'*, which causes the periodicity doubling. Basically, the deformation of honeycomb and Seiwatz chains might be imaged by STM in occupied orbitals. Unfortunately, the experimental filled-state STM images were too obscure to verify a double periodicity of such surface structures. As to the distortion of Yb rows, it can be simply missed in STM images for many reasons. Hence, the other techniques are required for further clarification. It should be also emphasized that the fingerprint of the ×2 periodicity in the intermediate structures are dim diffuse LEED spots. However, they are very weak, meaning that the ×2 ordering is poor enough and the correlation length of distorted Si and/or Yb chains is very short.

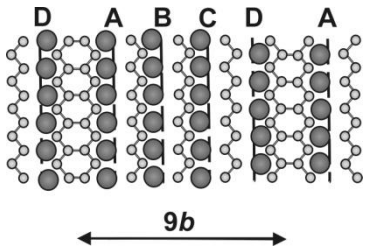

Fig. 30. The schematic presentation of (9×1) structure. The channels between H and S chains are marked by dashed lines and labeled A, B, C, and D. The Yb atoms are shown by large circles. For the sake of simplicity, the distortion of structural elements (Si chains and Yb rows) is not illustrated.

Within the above models, it should be expected that the Yb atoms have different environment in the intermediate phases with a larger unit cell, (7×1) and (9×1), irrespective of which periodicity and adsorption sites are assigned for the Yb atoms. In particular, some Yb rows run in these reconstructions between two Seiwatz chains and the others between one Seiwatz chain and one honeycomb chain. Therefore, we assume that such rows are not equivalent. It can be realized in the diagram presenting the schematic model of (9×1) reconstruction (Fig. 30). In this diagram, there are two edge rows running in the channels marked by dot lines and labeled A and D. These rows have a different surrounding compared to that of the rows B and C. The A and D rows can also differ from each other. Note

that for the sake of simplicity, the distortions of Si and metal chains are not shown in Fig. 30.

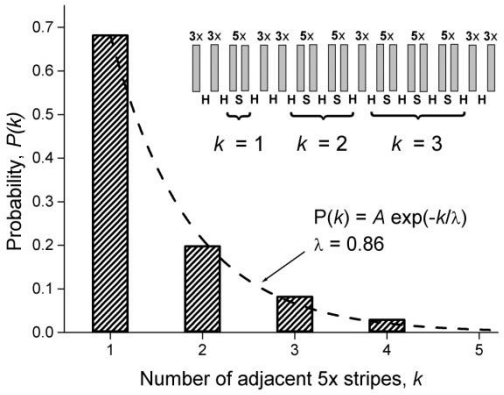

Fig. 31. The probability of *k* adjacent 5× stripes as a function of *k* for the 0.34-ML Yb/Si(111). The inset of histogram illustrates the row combinations for *k* = 1, 2, and 3.

3.2.3.2. Statistical analysis

Here we examine the correlation of atomic rows on the Yb/Si(111) surfaces using a statistical analysis of STM data. As mentioned earlier, the formation of (5×1) phase occurs by means of substitution of 3× stripes by 5× stripes, and for example, the resulting configuration at 0.34 ML in Fig. 28(a) and 28(b) is a combination of both stripes mixed microscopically. Let us introduce a parameter *k* that represents the number of adjacent 5× stripes on this surface. That is, $k = 1$ corresponds to a single 5× stripe, $k = 2$ to two adjacent 5× stripes and so on (see the inset of Fig. 31). Then, the histogram given in this figure presents the probability of *k* neighboring 5× stripes, $P(k)$, as a function of *k*. For this histogram, we utilized a series of STM images from randomly selected surface areas comprising the total surface area of more than 9000 nm^2 and more 150 stripes. As shown, the single isolated stripes ($k = 1$) have the highest probability at 0.34 ML, which is quite natural, as there are co-existing (5×1) and (3×2) phases at this coverage. Also, the histogram shows that upon increasing the parameter *k*, the $P(k)$ decreases exponentially and can be well described by the expression $P(k) = A \times exp(-k\lambda)$, where $\lambda = 0.86$. Taking into account that the 5× stripes are mixed with the 3× ones, such behavior can imply a random distribution of 5× stripes at 0.34

ML. In the other words, the 5× stripes show neither tendency to group into regular 5×1 domains nor to arrange the configuration with long-range repulsive interaction between the stripes. Assuming that the (5×1) unit cell involves one Seiwatz chain and one honeycomb chain, the histogram also illustrates the probability distribution for the Seiwatz chains, where k = 1 corresponds to the configuration of ...HHSHH..., k = 2 to the configuration of ...HHSHSHH... etc.

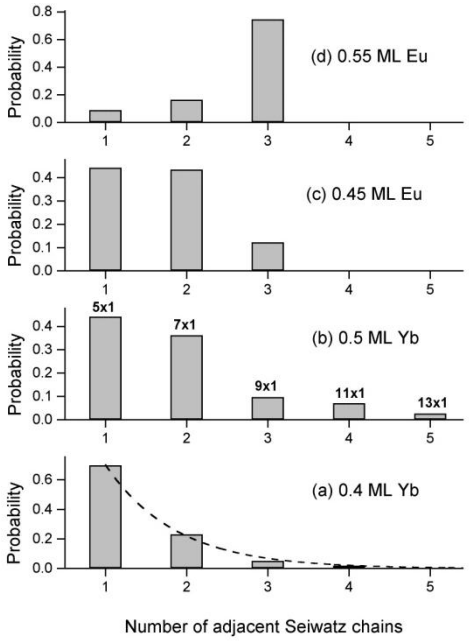

Fig. 32. The probability of m adjacent Seiwatz chains versus m for Yb/Si(111) at 0.4 ML (a) and 0.5 ML (b) and Eu/Si(111) at 0.45 ML (c) and 0.55 ML (d). Modified from: Kuzmin et al. 2004[c].

With increasing the Yb coverage, the proportion of Seiwatz and honeycomb chains gradually changes, and the 7×, 9× etc. stripes containing two, three and more adjacent Seiwatz chains appear. In order to measure the probability distribution for these stripes, we introduce a parameter m which represents the number of adjacent Seiwatz chains. The meaning of this parameter is the same as that of m in Table 4, i.e., m = 1 corresponds to the single isolated Seiwatz chains (5× stripes), m = 2 corresponds to the isolated pair of two neighboring Seiwatz chains (7× stripes) etc. Fig. 32(a) and 32(b) show the probability distributions for isolated groups composed of m adjacent Seiwatz chains, i.e., n× stripes, where n =

$2m + 3$ at 0.4 and 0.5 ML, respectively. At 0.4 ML, the single Seiwatz chains (m = 1) have the highest probability and the 5× stripes dominate. This is consistent with LEED showing the pure (5×1) (or (5×'2') pattern at this coverage.

Upon increasing m, the probability of n× stripes drops down and can be fitted by $P(m) = B \times exp(-m\lambda)$ with $\lambda = 0.86$ (Fig. 32(a)). This distribution is quite similar to that of 0.34 ML (Fig. 31), which indicates that the long-range indirect (i.e., via the substrate) interaction of Yb rows on the both surfaces has very similar character. Most likely, such interaction is rather weak so that a random mixture of different adsorbed phases with short correlation lengths is formed. Especially, a large variety of adsorbed phases can be found at 0.5 ML (Fig. 32(b)). As shown, the adsorbate layer has very broad distribution of n× stripes, yielding a mixture of local (5×1), (7×1), (9×1), (11×1), and (13×1) periodicities. These quantitative results clearly illustrate weak correlation of atomic rows/Seiwatz chains on the Yb/Si(111) surface at intermediate coverages, and therefore, this surface can spontaneously form a large variety of local periodicities mixed microscopically.

For comparison, a similar statistical analysis is performed for very related Eu/Si(111) system showing a similar series of adsorbate-induced phases (Kuzmin et al. 2004[c]). In contrast, the Eu/Si(111) surface behaves quite differently and shows much more correlated combinations of atomic rows. The histograms demonstrating the probability of n× stripes versus m for the Eu/Si(111) system at 0.45 and 0.55 ML are presented in Fig. 32(c) and 32(d), respectively. Clearly, both distributions are much narrower compared to the case of Yb/Si(111). The Eu-stabilized 5× and 7× stripes are dominating at 0.45 ML and the 9× stripes at 0.55 ML, and no other periodicities are found in the Eu/Si(111) system at these coverages, in contrast to Yb. Thus, the statistical analysis of STM data reveals an important difference in correlation of atomic rows at the Yb/Si(111) and Eu/Si(111) surfaces: the indirect interaction of Yb-induced rows is significantly weaker than that of Eu-induced rows on the Si(111).

In general, the long-range indirect interaction can play an important role in surface phenomena and adsorption systems, and in particular, the formation of linear atomic rows on surfaces is considered to be due to the anisotropic interaction between adsorbed atoms (e.g., Engelhardt and Menzel 1976). In a simplified picture, the attractive interaction is expected between the adatoms along the chains to overcompensate the dipole–dipole electrostatic repulsion in the orthogonal direction. In a generalized form, the long-range interaction potential can be described by two terms (Xu, Adams, and Einstein 1996). Decaying inversely with the square of distance, the first one is governed by the elastic or dipolar interactions (e.g., elastic strain field). In fact, the Eu atom has a large size

than the Yb atom (for example, compare the covalent radii of two atoms (2.02 and 1.94 Å, respectively). Therefore, one can expect that the potential of elastic strain field in the case of Eu adsorbate on the Si(111) decays slower than that of Yb, and therefore, the adsorbate rows are poorer correlated in the Yb/Si(111) system than those of Eu/Si(111).

The second term also decays very slowly and is interpreted as indirect electronic interaction (Frohn et al. 1991; Redfield and Zangwill 1992; Repp et al. 2000). In the case of semiconductor substrates, the indirect electronic interaction can be mediated by the surface states, and especially one expects considerable oscillatory interaction if the surface states are located near the Fermi energy (Grimley 1967; Einstein et al. 2001). Understanding the role of this term requires a detailed knowledge of the electronic structure of the both systems, but the electronic structure of Eu/Si(111) reconstructions, at least, has not been studied yet. In the absence of such data, we speculate that the different filling of 4*f* subshell in Yb and Eu can be also responsible for the difference in long-range indirect interaction in the Yb/Si(111) and Eu/Si(111). In particular, owning complete 4*f* occupation in divalent configuration, Yb ($4f^{14}$) is diamagnetic, whereas divalent Eu ($4f^{7}$) exhibits a paramagnetic behavior (Wieling et al. 2002). For the latter, a large spin moment can result in a stronger polarization of adsorption bonds formed by Eu 6*s* electrons and Si dangling bonds.

Finally, we presume that the long-range indirect interaction most likely controls the triple- to-single-domain transitions in chain reconstructions on vicinal Si(111) substrates with narrow terraces (Vaara et al. 2003[b,c]). Indeed, the minimization of total number of atomic chains on such surfaces can be the driving force that favors the domain orientation parallel to steps and depresses the two other orientations.

3.3. 2D reconstructions on Si(100) and Ge(100)

Among the metal-induced reconstructions on the Si(100) surface, the (2×3) phase formed by numerous metals in the low submonolayer coverage regime (≤ 1/3 ML) has attracted perhaps the most singnificant interest and been reported most frequently, thus serving as a prototype model system for the metal/Si(100) reconstructions. Various structural models have been proposed for metal/Si(100)(2×3) surfaces. In earlier work, the adsorbate atoms were assumed to reside at specific adsorption sites in the dimer row (2×1) reconstruction of the clean Si(100) (Fan and Ignatiev 1991; Abukawa, Okane, and Kono 1991; Brodde, Bertrams, and Neddermeyer 1993). Later on, STM evidenced that the Si substrate

can be significantly rearranged by metal atoms. For example, the model proposed for the Na/Si(100)(2×3) has suggested the top Si-atom density of 1/3 ML and included alternating dimeric and monomeric Si rows (Saranin et al. 1998[c]). Similar, albeit not equivalent, rearranged Si structures have been considered for Ba (Kim et al. 1999; Herrera-Gómez et al. 2000; Ojima, Yoshimura, and Ueda 2001) and Eu (Kuzmin et al. 2005[b]). Theoretical support, however, has been so far very rare for such systems, which hinders the identification of atomic structure.

The most typical reconstructions on RE/Si(100) surfaces, which have been reported so far, are (2×3) and (2×4) ones. The former has been observed for Yb (Pasquali, D'Addato, and Nannarone 2002; Katkov and Nogami 2003; Kuzmin et al. 2003[a]), Nd (Katkov and Nogami 2003), Er (Yang et al. 2003), Eu (Kuzmin et al. 2005[b]), and Sm (Onsgaard et al. 1990 and 1991; Ohbuchi and Nogami 2005; Kuzmin et al. 2011[b]), and the latter for Dy (Liu and Nogami 2001; Lochner et al. 2015), Ho (Ohbuchi and Nogami 2002), Tm (Cui and Nogami 2011), Yb (Katkov and Nogami 2003; Kuzmin et al. 2003[a]), and Nd (Katkov and Nogami 2003). In general, most of studies performed for these structures by STM have reported rather similar results for different structures; however, only registries of STM features in empty and filled states have been reported in most cases. Most likely, the absence of adequite structural models is due to that the constructing of atomic model usually requires a comprehensive combination of different experimental and theoretical techniques. A combined STM and first-principles calculation study, which was focused on the Gd/Si(100) system, has shown that the (2×3) and (2×4) phases can be considered as building blocks for more complicated (2×7) and (2×8) structures (Liu and Nogami 2003). Hence, the detailed information about the RE-induced (2×3) and (2×4) structures on Si(100) is essential for understanding of the RE/Si(100) systems.

Here we present detailed results obtained by combined experimental and theoretical methods for three Yb-induced reconstructions on the Si(100), namely (2×3) and (2×4) ones formed at relatively low submonolayer coverages and (2×6) one formed at relatively high submonolayer coverage (Kuzmin et al. 2003[a], 2008, and 2010[b]; Punkkinen et al. 2009), as well as Yb-induced (2×4) reconstruction on the Ge(100) surface (Kuzmin et al. 2013). Based on these results we propose atomic models for these systems.

3.3.1. Yb/Si(100)(2×3) and -(2×4)

3.3.1.1. LEED, STM, and CLPES

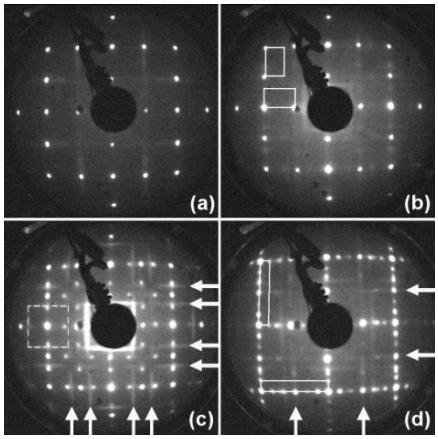

Fig. 33. LEED patterns of (a) clean Si(100) and (b)-(d) Yb/Si(100). (a) The double-domain (2×1) structure. E_p = 44 eV. (b) The (2×1) pattern coexisting with weak (2×3) spots at 0.1 ML Yb. E_p = 47 eV. (c) The double-domain (2×3) spots and additional streaks at 0.25 ML Yb. E_p = 49 eV. (d) The double-domain (1×6) spots and half-order streaks at 0.5 ML. E_p = 42 eV. The streaks are marked by arrows.

In studying the Yb/Si(100) surface the common problem is that it is difficult to determine the saturate coverage for different structures, because all those can readily coexist in the wide coverage ranges. For example, neither (2×3) nor (2×4) can be produced in the pure form covering the surface area completely. These phases are usually microscopically mixed with each other and sometimes with some other phases. LEED showed that the (2×3) and (2×4) structures can appear in the form of diffraction spots and streaks. Fig. 33 examplifies LEED patterns of clean and Yb-adsorbed surfaces at different coverages. The clean surface exhibits sharp spots of the double-domain (2×1) structure (Fig. 33(a)). The Yb deposition leads to an appearing of weak extra spots of double domain (2×3) LEED pattern at 0.1 ML (Fig. 33(b)). Both (2×3) and (3×2) unit cells are shown by white line boxes (note that the (2×1) and (1×2) LEED spots are also still seen at this coverage). The (2×3) pattern becomes much brighter with increasing the Yb coverage.

Fig. 33(c) represents the diffraction results observed at ~0.25 ML. In addition to the fractional diffraction spots with the ×3 periodicity, additional streaks (marked by arrows) are found. Their fractional order is different from 1/3. Therefore, one can assume the features have the 1/4 order.

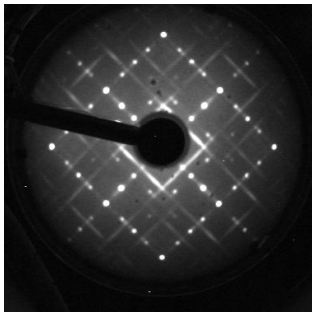

Fig. 34. LEED pattern for the Yb/Si(100) at the coverage which is slightly different from 0.25 ML. The (2×3) and (2×4) structures are observed in the form of 1/3-order streaks and 1/4-order spots. E_p = 61 eV.

At lightly different coverage, one can also observe the LEED pattern where the (2×3) and (2×4) periodicities are manifested in the form of respective streaks and spots, indicating that the ratio of (2×3) and (2×4) structures is dependent on the coverage and, probably, growth conditions. Thus, the persistent coexistence of the two structures in LEED implies a close similarity of their atomic structures and saturate coverages.

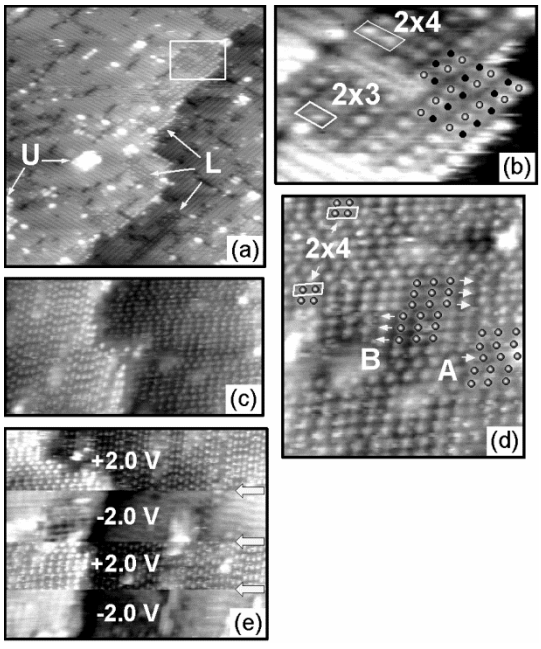

Fig. 35. The empty-state, filled-state, and dual-polarity STM images of Yb/Si(100) at different coverages. (a) 0.1 ML Yb. 36 nm × 36 nm, V_S = 2.0 V, I_t = 0.15 nA. 'U' and 'L' denote upper and lower (2×3) Yb domains, respectively. (b) A magnification of area enclosed in white line box in (a). (2×3) unit cell is marked. The open and solid circles illustrate upper and lower protrusions, respectively, 7.5 nm × 5 nm. (c) 0.25 MLYb. 31nm × 16 nm, V_S = 2.0 V, I_t = 0.59 nA. (d) 0.25 ML Yb, 14 nm × 15 nm, V_S = 2.0 V, I_t = 0.59 nA. A and B defects as well as local (2×4) structure are shown. (e) 0.25 ML Yb. 31.5 nm × 25.5 nm, V_S = -2.0 V/+2.0 V, I_t = 0.59 nA. Arrows indicate a tip position where a sample bias reverse was applied. The other details can be found in the text.

In Fig. 35(a) an empty-state STM image acquired at 0.1 ML Yb is presented. In this image, two terraces separated by the so-called S_B step are identified. The upper terrace exhibits (2×3) domains which are composed of large bright protrusions associated with metal atoms. The white line box points out one of these domains. The domains are surrounded by (2×1) Si dimer rows running along the [01-1] direction. On the lower terrace, in the right bottom corner of Fig. 35(a), the equivalent, 90°-rotated, (3×2) domain co-exists with the (1×2) dimer rows of Si aligned along the [011] direction.

This STM image also reveals that the top of (2×3) and (3×2) islands of Yb-induced phase appears in two different height levels with respect to that of the (2×1) and (1×2) Si dimers, respectively. On the both terraces the protrusions of lower islands (labeled L) are found below Si dimers by 0.07 Å, and the protrusions of upper islands (labeled U) are 1.1 Å higher than the Si dimers. Obviously, lower Yb domains substitute Si dimers. It means that the formation of the Yb adsorbed phase involves Si mass transport. It is interesting to note that the lower Yb domains, as found in large-scale STM image of this surface (not shown), tend to nucleate near the upper edge of the S_B steps. This fact can be understood taking into account that the S_B steps are known to yield much higher sticking probability and be much more reactive compared to the S_A steps (Hoeven et al. 1989; Koo et al. 1996; Wingerden et al. 1997). Therefore, one can expect that the activation barrier for removing the Si dimers from the S_B step edges, which is required for the formation of the lower Yb domains, is lower than that of the S_A steps. In addition, an anisotropy established for surface diffusion of adsorbate atoms along and across the Si dimer rows on the Si(100) (Wang et al. 1999) can play a significant role in the formation of Yb domains near the S_B steps.

The careful inspection of Fig. 35(a) shows that, besides the ordered (2×3) and (3×2) islands, the Yb atoms arrange single and double atomic chains, dimers and

monomers (not marked here) on both terraces of Si(100). The Si dimer vacancies are also found on bare surface areas.

A magnification of the surface area outlined by white box in Fig. 35(a) is presented in Fig. 35(b), which reveals not only the bright round protrusions seen already in Fig. 35(a), but also chains of darker protrusions. The in-plane separation and vertical distance between the brighter (upper) and darker (lower) protrusions are 4.24 and 0.34 Å, respectively. As shown in Fig. 35(b), the pairs of the neighboring upper and lower maxima are separated by the dark areas that can be interpreted as Yb vacancies in the atomic arrangement of outermost layer. Thus, the (2×3) unit cell shown in Fig. 35(b) includes one upper protrusion, one lower one, and the dark area associated with the Yb vacancy. In addition, the local (2×4) mesh, composed of two bright maxima and one darker protrusion, can be also found in this figure. These observations are very consistent with the analogous STM results reported elsewhere (Katkov and Nogami 2003).

At 0.25 ML Yb adsorbed phase covers nearly the whole surface as seen in the empty-state STM image in Fig. 35(c). Two terraces are present in this image. The terrace shown in the left part exhibits the (3×2) phase, and the other does the (2×3) phase. For the sake of brevity, we will notice the both phases as the same (2×3) hereafter. Also, the Yb layer includes an abundance of atomic-scale defects illustrated in Fig. 35(d). First, some of single rows of the protrusions are shifted by Si lattice constant (a_{Si} = 3.84 Å). This type of defects is marked by A in Fig. 35(d). Second, the other type is a coherent shift of such rows by a_{Si} (labeled B). In the latter case, the domain walls separating the neighboring (2×3) domains are present. Third, local (2×4) units distributed randomly are found in the Yb layer. In general, the A and B type defects are believed to relieve the surface stress.

The filled-state STM images of Yb/Si(100)(2×3)/(2×4) demonstrate much lower contrast compared to the empty-state STM images. Fig. 35(e) illustrates the difference between the two STM modes. Probing the area shown in this image, a sample bias reverse (from -2.0 to 2.0 V and vice versa) has been applied three times. The tip positions where the voltage was reversed are marked by arrows. Despite the relatively poor brightness contrast at a negative bias-voltage polarity, the (2×3) arrangement can be also revealed at -2.0 V, in agreement with the empty-state STM data.

Thus, to recapitulate, STM reveals that in the low coverage regime ≤ 1/3 ML, Yb induces the structures with the (2×3) and (2×4) periodicities on the Si(100). LEED showed that the (2×3) periodicity found at 0.1–0.2 ML can gradually change to the (2×4) periodicity with increasing the coverage, but the both phases always coexist and are very related to each other: in empty-state images they show up rows of grouped oval protrusions, with two and three ones in each group,

respectively. A closer inspection of STM images indicated that the neighboring protrusions in both (2×3) and (2×4) unit cells are not identical in brightness and shape, and that the Yb atoms have two different bonding sites in each of the 2×3 and 2×4 phases. Although the registry of STM protrusions with respect to the surround clean Si(100) dimers is clearly established (Katkov and Nogami 2003), the atomic structure of (2×3) and (2×4) phases still remains unclear. Since the STM images of the Yb/Si(100)(2×3)/(2×4) are strongly bias dependent and, thus, contributed by the electronic structure effects. Hence, other techniques are needed to shed more light on the atomic structure of these reconstructions.

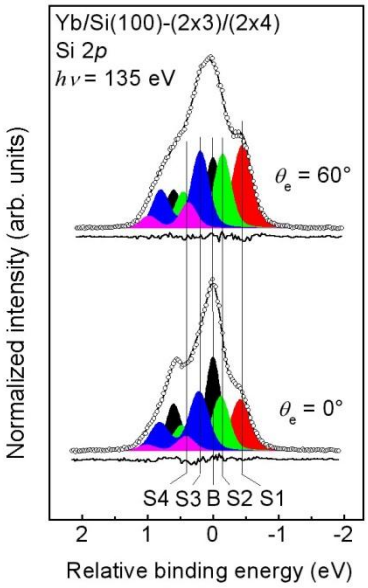

Fig. 36. Si 2*p* spectra for the Yb/Si(100)(2×3)/(2×4) at *hv* = 135 eV and θ_e = 0° and 60°. The raw data (open circles) are presented after the background correction by Shirley's method. The fitting curves are given by solid lines. The residuals are shown for each spectrum by solid line. The bulk (*B*) and surface (*S*1, *S*2, *S*3, and *S*4) components are illustrated by shadow doublets.

Si 2*p* core-level spectroscopy is one of experimental tools which are able to give more information about the Si arrangement of Yb-induced (2×3) and (2×4) phases. Next, we examine the Si 2*p* line shape for the Yb-induced (2×3)/(2×4). Fig. 36 shows Si 2*p* spectra taken for such a surface at *hv* = 135 eV and θ_e = 0° and 60°. The experimental data are given by open circles. The quantitative

analysis of the spectra was done by using the standard fitting procedure with a linear combination of Voigt function peaks. The fitting parameters are listed in Table 5. The fitting reveals four surface components, *S*1-*S*4, with SCLSs of -0.43, -0.13, 0.21, and 0.39 eV relative to the bulk peak *B*. In Fig. 36 these components are shown by shadowed doublets. The analysis of such data allows us to arrive at the following conclusions.

Table. 5. Fitting parameters for the Si 2*p* spectra in Fig. 36. The spin-orbit splitting, branching ratio, and Lorentzian width are identical for all components. The values of spin-orbit splitting, Lorentzian width, Gaussian widths, and surface core-level shifts are given in electronvolts.

	B	*S*1	*S*2	*S*3	*S*4
Spin-orbit splitting	0.602				
Branching ratio	0.50 ± 0.02				
Lorentzian width	0.085				
Gaussian width	0.227	0.299	0.264	0.287	0.262
Surface core-level shift	–	-0.43	-0.13	0.21	0.39

The Si 2*p* line shapes observed for the Yb/Si(100)(2×3)/(2×4) in Fig. 36 and earlier work where the substrate was a vicinal Si(100) surface (Perälä et al. 2005) are different. Also, the number of surface components in Fig. 36 is different from that of (2×3)/(2×4) on the vicinal Si(100) substrate. The present Si 2*p* data does not reproduce the lowest-binding-energy component with a SCLS of –0.64 eV which is found in the case of vicinal substrate. Therefore, such a component is not actually due to the (2×3) and (2×4) phases. In contrast, the other four surface components, *S*1-*S*4, are well reproduced in both studies, indicating that those are caused by the (2×3)/(2×4).

Comparison of the Si 2*p* results for the Yb/Si(100)(2×3)/(2×4) surface and the clean Si(100)(2×1) surface (not shown) reveals that the bulk peak moves toward the higher binding energy by 0.12 eV upon the Yb adsorption. This infers that the Fermi level position in the band gap of Yb/Si(100)(2×3)/(2×4) is moved upward by 0.12 eV as compared to the clean surface. Note that such behavior strongly resembles that of the Eu/Si(100)(2×3) surface, where the respective shift was reported to be 0.14 eV (Kuzmin et al. 2005[b]).

3.3.1.2. DFT calculations. Part I

For the interpretation of experimental results in more detail, first-principles calculations have been performed. The electronic structure calculations have been made using the *ab initio* total energy program VASP (Vienna *ab initio* simulation package) (Kresse and Hafner 1993, 1994; Kresse and Furthmüller 1996[a,b]), which is based on DFT (Hohenberg and Kohn 1964; Kohn and Sham 1965). Within this package the projector augmented wave (PAW) method (Blöchl 1994; Kresse and Joubert 1999) and the local density approximation (LDA) of Ceperley and Alder (Ceperley and Alder 1980), as parametrized by Perdew and Zunger (Perdew and Zunger 1981), are used. The optimization of atomic structure is performed using conjugate-gradient minimization of the total energy with respect to the atomic coordinates. The Yb 6*s* and 5*p*, and the Si 3*s* and 3*p* electrons are included as valence electrons. Slabs with 12 atomic layers, one Yb layer, and eleven Si layers are used. The dangling bonds of the bottom surface Si atoms are passivated by hydrogen atoms. Theoretical lattice constant (3.8387 Å) is used, and two bottom atomic layers of the slabs are fixed to the ideal positions. Other atoms, including the hydrogen atoms, are relaxed until the remaining forces are less than 20 meV/Å. The energy cutoff is 280 eV. The number of *k* points in the Brillouin zone is 24 (18) corresponding to a *k* mesh of 6×4×1 (6×3×1) for the (2×3) ((2×4)) reconstruction.

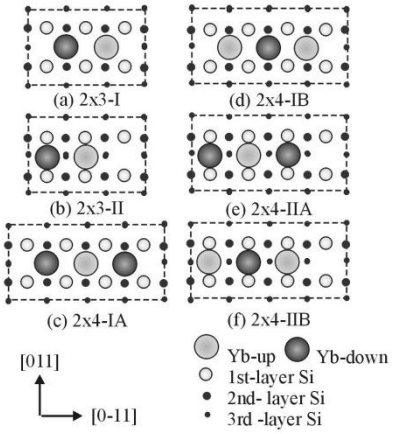

Fig. 37. Possible geometric structures of Yb/ Si(100)(2×3) and –(2×4) phases. The (2×3) and (2×4) unit cells are shown by dot lines.

In this Subsection, we consider, on the basis of STM observations and registry of STM protrusions, several atomic configurations which are potential

candidates for the atomic models of Yb/Si(100)(2×3) and –(2×4) and examine them theoretically. As a starting point for simulations, we assume that the first-layer Si dimers, which are characteristic of the clean Si(100)(2×1) surface, are stripped off, as evidenced from Si 2*p* core-level measurements. That is, the Si substrate initially has the bulk-terminated structure, and the Yb atoms are adsorbed on such a surface. Even though this picture is too simplified, the optimization of these models can allow one to unveil the main tendencies upon formation of these reconstructions. For the (2×3), the Yb coverage is proposed to be 1/3 ML in both configurations, (2×3)-I (Fig. 37(a)) and (2×3)-II (Fig. 37(b)), which is consistent with the number of protrusions in empty-state STM images (two maxima per (2×3) unit). The bonding sites of respective Yb atoms are not identical (labeled Yb-up and Yb-down in Fig. 37), as the empty-state STM protrusions are inequivalent. The (2×4) atomic configurations (Fig. 37(c)-(f)) include three Yb atoms per unit cell, where two of them are equivalent. Such atoms are associated either with bright STM protrusions in the "bright protrusion – dark protrusion – bright protrusion" (BDB) configuration (the (2×4)-IA and (2×4)-IIA structures) or with dark STM protrusions in the DBD configuration (the (2×4)-IB and (2×4)-IIB structures).

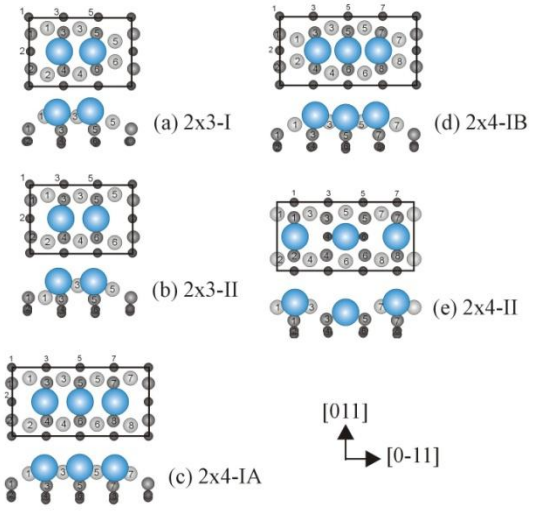

Fig. 38. Fully optimized atomic models of Yb/Si(100)(2×3) and –(2×4) on the basis on the geometric structures in Fig. 37. The Yb atoms are shown by the large circles. Only three upper Si atomic layers are illustrated. The (2×3) and (2×4) are shown by line boxes.

The models of Fig. 37 were optimized by VASP. The fully relaxed atomic geometries of the above reconstructions are illustrated in Fig. 38. The calculations indicate that both the (2×4)-IIA and (2×4)-IIB structures in Figs. 37(e) and 37(f) are unstable and converge to the same configuration shown in Fig. 38(e). It will be called (2×4)-II hereafter. The (2×3)-I and (2×4)-IA geometries (Figs. 38(a) and 38(c)) are found to be the most stable among the models shown in Fig. 38. The relative surface energies of the (2×3)-I, (2×3)-II, (2×4)-IA, (2×4)-IB, and (2×4)-II are given in Table 6. The surface energies of (2×3)-I and (2×4)-IA are lower by 0.016 and 0.008 eV/(1×1) than those of (2×3)-II and (2×4)-II, respectively.

Table 6. Surface energy difference ΔE (eV/(1×1)) for the (2×3) and (2×4) structures in Fig. 38. The values are given with respect to the ground-state (2×3)-I and (2×4)-IA configurations, respectively.

	(2×3)-I	(2×3)-II	(2×4)-IA	(2×4)-IB	(2×4)-II
ΔE	0	0.016	0	0.058	0.008

A closer inspection of the atomic configurations in Fig. 38 gives more information about the Yb/Si(100)(2×3) and –(2×4) phases. Regarding the (2×3) phase, the following trends can be established.

(i) The adsorption site shown in Fig. 37(b) is unfavorable for the Yb atoms in the (2×3) structure. In both fully optimized (2×3)-I and (2×3)-II configurations, the equilibrium adsorption site for the Yb atoms is found to be the one shown in Fig. 37(a). Thus, the (2×3)-II model of Fig. 37(b) is unstable; the optimization of this structure leads to the geometry (Fig. 38(b)) which is very similar to the (2×3)-I in Fig. 38(a).

(ii) The difference in height of two Yb atoms in the (2×3) unit for the models in Figs. 38(a) and 38(b) is 0.15 and 0.04 Å, respectively. Whereas the height difference of bright and dark STM protrusions in empty-state images of Fig. 35 is 0.34 Å. This is in consistency with that STM images of the Yb/Si(100)(2×3) are bias dependent and thus affected by not only the atomic geometry but also the electronic structure effects.

(iii) In both (2×3)-I and (2×3)-II configurations, the first Si layer is strongly rearranged; the first-layer Si atoms tend to dimerize. In these calculations, there are still three symmetrical (unbuckled) first-layer Si dimers, i.e., Si(1)-Si(2), Si(3)-Si(4), and Si(5)-Si(6), per (2×3) unit (the dimer buckling is not yet considered). Furthermore, the bond lengths and vertical locations of such dimers

are not identical. In particular, the bond lengths of the Si(5)-Si(6), Si(3)-Si(4), and Si(1)-Si(2) are 2.29, 2.60, and 2.49 Å in the (2×3)-I and 2.31, 2.64, and 2.48 Å in the (2×3)-II, respectively. The height differences of these dimers along the [100] direction are 0.64 and 0.59 Å for the (2×3)-I, and 1.34 and 0.93 Å for the (2×3)-II. In other words, one of these dimers, i.e., the Si(5)-Si(6) in the (2×3)-I and the Si(1)-Si(2) in the (2×3)-II is significantly lower as compared to the other two dimers, and thus the dimer rows aligned along the [0-11] direction are modulated in height. Note that the [0-11] direction is parallel to the dimer row direction on the clean Si(100)(2×1).

(iv) Moreover, the structure of underlying Si layers is also slightly modified, suggesting the Si rearrangement to penetrate deeply into the Si bulk.

(v) The lateral separation of neighboring Yb atoms in a metal row of the (2×3)-I and –II is 3.75 and 3.94 Å, respectively. Taking the covalent radius of Yb (1.94 Å) into account, it is likely that the Yb atoms are able to interact directly to each other in these structures. In such a scenario an appearing of a vacancy between the Yb atoms paired in the [0-11] direction is thought to be responsible for the strain relief. The structural deformation in the first Si layer might have the same origin as well.

For the (2×4) structure, a similar adsorption site is found to be favorable for all Yb atoms in the favorable (2×4)-IA structure (Fig. 38(c)) and the related (2×4)-IB structure with reverse Yb-triplet configuration (Fig. 38(d)). In the (2×4)-II structure, two atoms of the Yb triplet are adsorbed on the same sites, whereas the third Yb atom resides at an inequivalent site (Fig. 38(e)). For the (2×4)-IA and (2×4)-IB, the height differences between the outer and inner atoms of the Yb triplets are 0.05 and 0.27 Å, respectively, and the lateral separations of such atoms are 3.95 and 3.41 Å, respectively. Similar to the case of (2×3)-I and (2×3)-II structures, the first-layer Si atoms in the (2×4)-IA and (2×4)-IB form dimers, as shown in Figs. 38(c) and 38(d). In addition, the Si dimer rows of the (2×4)-IA and (2×4)-IB are aligned along the [0-11] direction, i.e., parallel to the Si dimer rows in the (2×3)-I and (2×3)-II. Obviously, this implies that the (2×3) and (2×4)-I structures are closely related. In contrast, (2×4)-II (Fig. 37(e)) shows the height difference and lateral separation of the inner and outer Yb-triplet atoms to be much higher (1.10 and 5.68 Å, respectively).

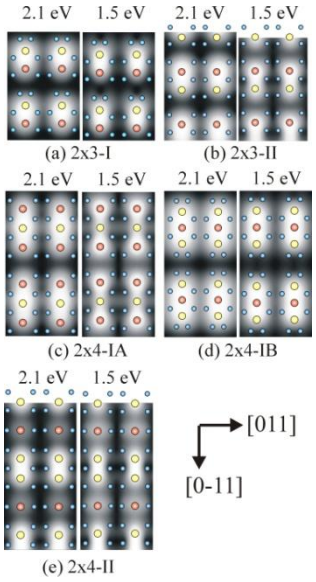

Fig. 39. Simulated empty-state STM images for the (2×3)-I, (2×3)-II, (2×4)-IA, (2×4)-IB, and (2×4)-II structures shown in Fig. 38. The simulations are performed within energy ranges of 2.1 and 1.5 eV above the calculated Fermi energy. The atomic positions of the Yb atoms and the first-layer Si atoms are given by large and small circles, respectively.

Based on the atomic models in Fig. 38, STM images and Si 2*p* SCLSs have been calculated. Fig. 39 represents the spatial distributions of empty states for the (2×3)-I, (2×3)-II, (2×4)-IA, (2×4)-IB, and (2×4)-II configurations within energy ranges of 2.1 and 1.5 eV above the calculated Fermi energy. In these configurations the equilibrium positions of Yb atoms and first-layer Si atoms are also given for each model. As the atomic arrangements of (2×3)-I and (2×3)-II are very similar, it is not surprising that they give rise to similar empty-state distributions, where the most pronounced features are located near to the Yb atoms, although the first-layer Si atoms are also seen to contribute to the above images. In particular, it means that the dangling bonds of first-layer Si atoms are not fully saturated by valence electrons donated by the Yb atoms to the Si substrate. In a simplified picture, two [three] Yb atoms, which are completely divalent in the (2×3) and (2×4) phases, as evidenced from Yb 4*f* measurements (not shown), can donate four (six) 6*s* electrons to the (2×3) [(2×4)] surface unit. Since these units include six and eight first-layer Si atoms with dangling bonds, respectively, it is obvious that all these dangling bonds cannot be completely

saturated by the Yb adsorption. More rigorously, the above STM images reflect the spatial distribution of electronic states induced by the covalent bonding of Yb and Si atoms in the (2×3) and (2×4) structures.

More interestingly, the empty-state images of Fig. 39 are found to depend on bias voltage, in good agreement with experiment (Katkov and Nogami 2003), and the 1.5-eV images for the (2×3)-I and (2×3)-II structures are apparently different. Roughly, the (2×3)-II image shows two maxima centered on the Yb atoms and has the mirror-symmetry plane in the [011] direction, i.e., in the twofold-periodicity direction. In contrast, the (2×3)-I image shows, in addition to the two maxima caused by Yb, a pair of dim features located near to the Si(5) and Si(6) atoms, and therefore, it does not reveal the above mirror symmetry.

For the (2×4) models, the empty-state images are also bias dependent (Figs. 39(c)-(e)). It is worth noting that the main maxima are approximately centered on the Yb atoms, which is similar to the case of (2×3) models. However, the brightness of maxima does not always reflect the vertical position of Yb atoms. Especially, this trend is evident for the (2×4)-IA structure, where the 1.5-eV image shows the bright protrusions located on the lower Yb atoms and the dark protrusions located on the higher Yb atoms. In contrast, the higher the Yb atoms are located, the brighter the protrusions are in the 2.1-eV image. Thus the empty-state STM images calculated for both the (2×3) and (2×4) are bias dependent, in agreement with experimental images (Katkov and Nogami 2003).

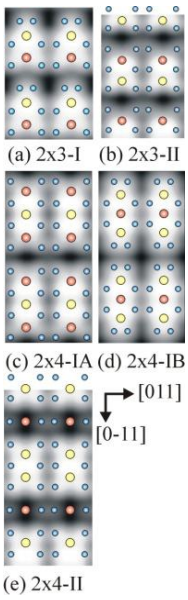

Fig. 40. Simulated filled-state STM images for the same structures as in Fig. 39. The simulations are performed within energy ranges of 2.0 eV below the calculated Fermi energy. See the other details in the caption of Fig. 39.

Filled-state STM images were simulated for the (2×3) and (2×4) structures at two bias voltages (-2.0 and -1.5 V). It is found that the filled-state images for each of the structural models are very similar at these bias voltages. For this reason, we present here only the ones calculated at -2.0 V (Fig. 40). As shown, they are rather different from the empty-state images in Fig. 39, thus supporting the aforementioned dependence of STM images on bias voltage. In particular, for the both (2×3)-I and -II structures, we note that the main contributions in the filled states are two unresolved bright protrusions located in the vicinity of the Yb atoms. In addition, a shoulder located near to the Si(5) and Si(6) atoms is seen. Obviously, the latter STM feature is slightly more evident in the case of the (2×3)-I structure. For the (2×4) structures, the main contributions to the filled-state images are also Yb atoms. Moreover, the first-layer Si atoms also provide a minor contribution. In general, the filled-state images exhibit lower contrast in brightness than the empty-state images, in good agreement with experimental STM results shown in this section earlier.

To discriminate the atomic models for the (2×3) and (2×4) reconstructions, the calculated STM images in Figs. 39 and 40 are compared to the experimental ones (Katkov and Nogami 2003, Kuzmin et al. 2003[a]; Perälä et al. 2005). First, we notice that in experimental empty-state images, the contrast in brightness of different protrusions is found to depend on the bias voltage. Obviously, this is consistent with the behavior of maxima in the calculated empty-state images of Fig. 39.

Second, for the (2×3) reconstruction, some experimental empty-state images (Katkov and Nogami 2003, Kuzmin et al. 2003[a]) reveal two inequivalent maxima that exhibit not only different brightness but also different shape. This trend is consistent with the (2×3)-I structure rather than the (2×3)-II structure. In particular, the mirror symmetry considered above is clearly broken in the experimental images. In addition, the shape and location of protrusions in the measured empty-state images reasonably agree with those of the calculated images for the (2×3)-I structure in Fig. 39(a).

Third, the experimental filled-state images reveal the main bright protrusion, located in the vicinity of the bright maxima in the empty states, and the shoulder, located close to the position of the less bright protrusion in the empty states. Clearly, this behavior is also consistent with our calculated images for the (2×3)-I

structure in Fig. 39(a). We therefore conclude that the (2×3)-I model is the best candidate to describe the (2×3) phase, in good agreement with the surface-energy calculations showing this structure to be favorable.

The experimental empty-state STM images of the (2×4) reconstruction show two types of unit cells, which include either one bright and two dark protrusions the DBD triplet configurationor one dark and two bright protrusions the BDB one, and the protrusions exhibit an oval shape (Katkov and Nogami 2003, Kuzmin et al. 2003[a]; Perälä et al. 2005). The calculated empty-state images for both the (2×4)-IA and (2×4)-IB in Figs. 39(c) and 39(d), respectively, reasonably reproduce these experimental observations. Furthermore, the filled-state images calculated for the above structures (Figs. 40(c) and 40(d)) are consistent with those in experiment. In contrast, the STM images calculated for the (2×4)-II structure in the both empty and filled-state modes are fully inconsistent with the experimental images, and therefore, we rule out this structure as explanation of the (2×4) reconstruction. Thus, we assume that the (2×4)-IA and (2×4)-IB models are most plausible to account for the (2×4) phase. Note that according to our calculations, the favorable structure of the (2×4) phase is the (2×4)-IA model (the BDB configuration) rather than the (2×4)-IB model (the DBD configuration), and the energy difference of these configurations is 0.058 eV/(1×1) (see Table 6). However, the experimental STM images (Katkov and Nogami 2003) clearly evidence that both the configurations equally coexist in spite of the above energy difference. Most likely, such behavior can be understood in terms of surface kinetics, which depends on the surface preparation and which were not taken into account in the above thermodynamic calculations.

The atomic models suggested above have been also examined by calculation of Si 2*p* core-level shifts for the (2×3)-I, (2×3)-II, (2×4)-IA, (2×4)-IB, and (2×4)-II structures (Fig. 38) and comparison of these values with measured SCLSs. Theoretical values are obtained within the initial-state and complete-screening (i.e., including the initial- and final-state effects) models. The data calculated within the former approach for the Si atoms in the first four layers of each of the (2×3)-I, (2×3)-II, (2×4)-IA, (2×4)-IB, and (2×4)-II structures can be found elsewhere (Kuzmin et al. 2008). Here we discuss the main conclusions derived from those data. Based on such calculations, one can find that the Si 2*p* core-level shifts occur for several atomic layers of the (2×3) and (2×4) including the fourth and some deeper layers, and therefore, these reconstructions penetrate deeply enough into the bulk. The SCLSs calculated within the complete-screening model are found to be approximately the same as the initial-state SCLSs for the Si atoms in the second and deeper layers, and only for the first-layer Si atoms, the complete-screening SCLSs are somewhat different from the initial-state ones

showing a clear tendency to move toward the lower binding energy as compared to the respective initial-state values. This tendency has been also observed for the clean Si(100)(2×1) and Ge(100)(2×1) surfaces (Pehlke and Scheffler 1993).

In general, the core-level shifts evaluated for different atomic structures are scattered approximately throughout the similar energy ranges. For example, the energy ranges for the (2×3)-I and (2×3)-II structures are –0.36 to 0.31 eV and –0.42 to 0.40 eV, respectively. Therefore, one cannot unambiguously discriminate between these models on the basis of calculated Si 2*p* data. Also, the core-level binding-energy difference between some individual Si atoms in the (2×3) and (2×4) is so small that it is impossible to resolve all SCLSs in experiment within the instrumental resolution. Nonetheless, the variation of SCLSs in the first Si layer for different atomic structures can be useful in interpreting experimental Si 2*p* data.

For the (2×3)-I, (2×4)-IA, and (2×4)-IB models, which are the most plausible candidates to describe the (2×3) and (2×4) phases, the first-layer Si atoms reveal the shifts in the range between –0.36 and 0.23 eV within the initial-state scheme. Taking into account a systematic shift of SCLS values toward the lower binding energy for the topmost-layer Si atoms within the complete-screening model, we assume that the first-layer Si atoms in the (2×3) and (2×4) contribute mostly to the *S*1 and *S*2 components in Fig. 36. In addition, we notice that the *B* and *S*3 components in Fig. 36 might be also contributed by these atoms partly.Taking into account the facts that the Si atoms bonded to Yb atoms gain an additional electron charge and thus the respective Si 2*p* core-level binding energies are shifted to the lower values relatively the bulk Si atoms and that the first-layer Si atoms can directly interact with Yb atoms in the models of Fig. 38, the above assignments are reasonable.

Regarding the deeper Si atoms taking part in the formation of (2×3) and (2×4) reconstructions, the initial-state model was found to be adequate enough to reproduce SCLSs, as mentioned before, and the second- and third-layer Si atoms are thought to contribute to the *S*2, *S*3, and *S*4, in addition to *B*, whereas the fourth-layer Si atoms are assumed to cause the *S*2, *S*3, and *B*.

3.3.1.3. DFT calculations. Part II

Althought the DTF calculations in Subsection 3.3.1.2 unveiled several important trends in the formation of Yb/Si(100)(2×3) and (2×4) phases, in particular, the tendency for the dimerization of the topmost-layer Si atoms, some issues have still remained unresolved. For example, the dimer buckling has not been tested, and only two adsorption sites have not been examined for the Yb

atoms. In this subsection, we perform DFT calculations where the buckled top-layer Si dimers are initially removed, however, because of the instability of the bulk-terminated Si structure we allow the top-layer Si atoms to move slightly from their positions on Si(100)(1×1) to dimerize. The most favorable adsorption sites on such a surface (see Fig. 41(a)) are T3 (valley bridge) and T4 (cave), whereas HH (pedestal), HB (dimer bridge), and B2 (intermediate bridge) are less preferable (Pomyalov and Manassen 1997). Hence, we assume the RE-metal atoms to reside initially at either T4 or T3 (Figs. 41(b) and 41(c), respectively). In addition, we test a model with a less stable site (HH) shown in Fig. 41(d), and the models proposed earlier for Ba (Ojima, Yoshimura, and Ueda 2001) (Fig. 41(e)) and Eu (Kuzmin et al. 2005[b]) (Fig. 41(f)). The coverage of Yb atoms is 1/3 ML in all these models, meaning that there are two adsorbate atoms per (2×3) unit.

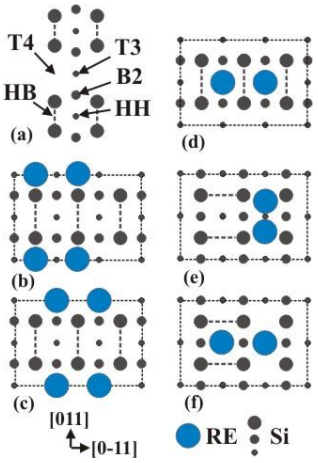

Fig. 41. (a) Adsorption sites on Si(100) with first-layer Si dimers. (b)–(f) Structural models of Si(100)(2×3) reconstruction stabilized by RE atoms. The dashed line boxes represent (2×3) unit cells and the gray dashed lines the orientation and position of the first-layer silicon dimers.

Our calculations indicate that the models in Figs. 41(e) and 41(f) are very unstable, and that the energies of such structures after their full optimization are higher by ~1 eV per (2×3) slab than those of Figs. 41(b) and 41(c). Therefore, we reject the models based on the dimeric and monomeric Si rows for the Yb/Si(100)(2×3). This is easily understood because the number of Si dangling bonds in these models is higher. Dimerization of Si atoms decreases the total energy considerably.

The optimization of the models in Figs. 41(b)–41(d) reveals that the fully relaxed structure corresponds to the model with the T3 adsorption site (Fig. 41(c)). In other words, the metal atoms locate always on valley-bridge adsorption sites. Two different patterns of top-layer Si dimers are found for the Yb/Si100(2×3), as in Subsection 3.3.1.2. One of the patterns ((2×3)-II) is more symmetrical than the other ((2×3)-I). Moreover, our finding reveals that one of the three Si dimers in both structures is buckled. The corresponding surface structures are shown in Fig. 42.

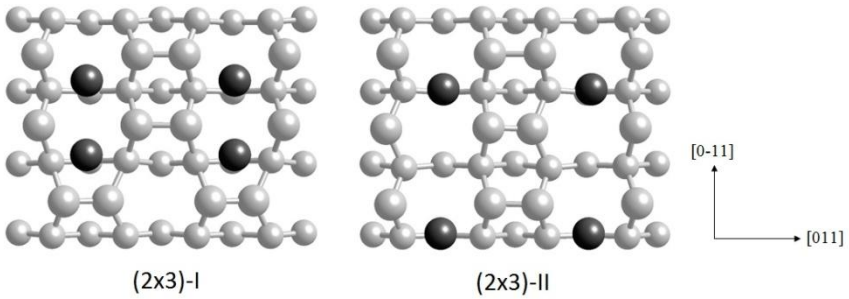

Fig. 42. Fully optimized atomic structures (top view) of (2×3) reconstruction. Left panel: (2×3)-I model. Right panel: (2×3)-II model. The (2×3)-II has a more symmetrical pattern of Si dimers. The black spheres denote adsorbate atoms and the gray spheres denote Si atoms. Atoms in the first and second layers are shown by larger spheres.

If there was no buckling, the ground state for the Yb/Si(100) would be the (2×3)-I, as was found in Subsection 3.3.1.2. Interestingly, the stability of (2×3)-I increases relative to the (2×3)-II as the volume of the substrate increases. Conversely, this means that the stability of (2×3)-I increases as the size of the adsorbed metal atom decreases. Note that for the related Eu/Si(100)(2×3) the favorable structure is the (2×3)-II rather than (2×3)-I, because the size of Eu atom is higher than that of Yb (Punkkinen et al. 2009). However, the buckling of one of the Si dimers lowers the total energy on both surfaces and makes the (2×3)-II stable for both Yb/Si(100) and Eu/Si(100) surfaces. Therefore, the ground-state reconstruction involves the symmetrical pattern of first-layer Si dimers and buckling. The buckling decreases the total energy by 0.033 eV/(1×1) area for the Yb/Si(100). Moreover, the additional lowering of the surface energy can be achieved by a symmetry change from the rectangular lattice to an oblique one, which leads to a further decrease in energy by 3 meV/(1×1). Then, the surface

lattice vectors are ($2a_{Si}$, a_{Si}) and (0, $3a_{Si}$). This symmetry change enhances the buckling of the Si dimers; the buckled dimers are tilted by 0.68–0.71 Å for the oblique lattice and 0.54–0.56 Å for the rectangular lattice. The dimer tilting in the oblique case is comparable to that of the bare Si(100) surface (0.78 Å). Note that a slight tilt (0.15–0.16 Å for the second Si dimer in the oblique case and smaller than 0.1 Å for the third one and rectangular case) is also found for the other two "unbuckled"dimers. Furthermore, the metal atoms are shifted in the direction perpendicular to the direction of metal atom pair slightly more away from each other in the oblique structure. Such tendency to the oblique symmetry is found, e.g., in the experimental STM images of Yb/Si(100) in Figs. 35(c) and 35(d).

It is worth to note that the (2×3) surface is semiconducting irrespective of the amount of Yb atoms in the (2×3) mesh, i.e., one, two, or even three atoms at the coverage of 1/6, 1/3, and 1/2 ML, respectively. This is understood, when we think the situation in the spirit of the electron counting model (Pashley 1989) (or generalized electron counting model (Zhang et al. 2006; Yang et al. 2008). For the Si(100)(2×1), the dangling-bond states related to the lower and upper atoms of the buckled Si dimer lie in the conduction and valence bands, respectively (Pehlke and Scheffler 1993), and thus the dangling bond of the lower atom is empty and that of the upper atom is filled. This is a reminiscence of the polar III-V(100) surface, where the group III atom is a cation and the group V atom is an anion. Within this picture, one can easily see that there are several ways to keep the Yb/Si(100) surfaces semiconducting due to the divalency of the Yb atoms and the inequivalency of dimers. If there is a single divalent Yb atom per (2×3) unit at 1/6 ML, it can donate two electrons to Si dimers. Then, one of the Si dimers donates two electrons to other two Si dimers of which both dangling bonds become occupied. It is also possible that two Si dimers become buckled and then the metal atom donates two electrons for the third Si dimer. If there are two metal atoms per (2×3) unit at the 1/3 ML coverage, two scenarios are possible. If only one metal atom donates its electrons, all the dimers can be unbuckled. But they are not equivalent (one of them locates in a different vertical position). It is energetically more favorable, however, that four electrons are donated from both metal atoms, which leads to one buckled dimer. Finally, if there are three metal atoms at the 1/2 ML coverage, then each of the metal atoms donates two electrons to one Si dimer, leading to the (2×1) structure hypothetically.

In summary, we have thoroughly considered the plausible atomic models for the Yb/Si(100)(2×3) and -(2×4) phases where the adsorbate coverage is 1/3 and 3/8 ML, respectively. The coverage determination, however, is complicated for these phases, because they are coexisting, as already mentioned. The 1/3 ML coverage for the (2×3) phase is consistent with a number of experimental

observations, e.g., STM, LEED, and TDS (Subsections 3.1 and 3.3.1.1). Nevertheless, based on these observations, we cannot exclude the case where the Yb/Si(100)(2×3) reconstruction has the coverage of 1/6 ML. Recently, the (2×3) reconstructions induced by 1/6 ML of Ba and Sr on Si(100) have been studied experimentally and theoretically (Kuzmin et al. 2014), and the so-called dimer-vacancy model has been proposed for such surfaces, where there are one unbuckled Si dimer in the first layer and three buckled Si dimers in the second layer of the substrate. It is still unclear whether such a structure can be stable for the Yb/Si(100)(2×3) at 1/6 ML. Future studies are required to resolve the issue.

3.3.2. Yb/Ge(100)(2×4)

Reconstructions induced by various metal adsorbates (e.g., AEM and RE) on Ge(100) are still significantly less studied than those of Si(100). Only a few studies have been so far reported for AEM/Ge(100) systems (Lukanov et al. 2011 and 2012; Sun et al. 2011). Moreover, no investigations of RE/Ge(100) reconstructions, except for a scanning tunneling microscopy study of Ho-germanide nanolines on Ge(100) (Bonet and Tear 2006), have been performed yet. Here we examine the Yb/Ge(100)(2×4) reconstruction. The present results are believed to provide a good platform for comparison of RE/Ge(100) and RE/Si(100) systems.

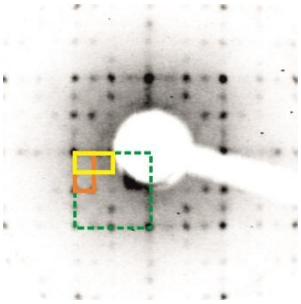

Fig. 43. LEED pattern of the double-domain Yb/Ge(100)(2 × 4) surface. Two equivalent 90°-rotated (2×4) units are shown by solid lines. The (1× 1) unit of the Ge bulk lattice is shown by dashed line. The electron energy is 111 eV.

Fig. 43 depicts a LEED pattern from the Yb/Ge(100)(2×4) reconstruction. In some measurements weak ×8 LEED spots (not shown here) were also observed in addition to the sharp (2×4) spots. The presence of the minor ×8 structure does not

affect practically the experiemntal data, e.g., photoelectron spectra from the Yb/Ge(100). Therefore, we will not consider the ×8 structure hereafter. Next, we will consider CLPES measurements and identification of the atomic structure of Yb/Ge(100)(2×4) based on measured SCLSs and DFT calculations.

3.3.2.1. CLPES

The Ge 3*d* core-level spectra were measured for both the Yb/Ge(100)(2×4) and the clean Ge(100) surface. For the latter, such spectra are well described in literature (Eriksson and Uhrberg 2010) and can be used for the justification of fitting procedure for the Yb/Ge(100) reconstruction.

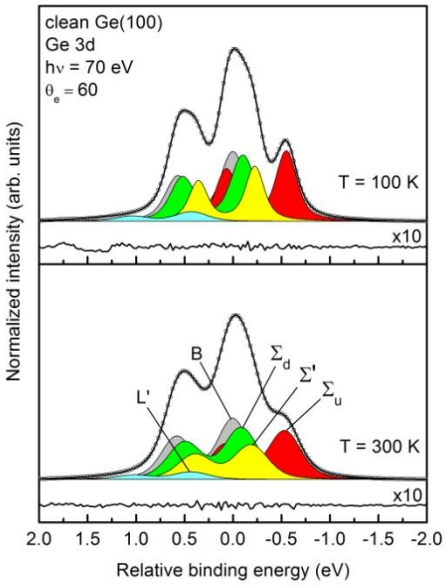

Fig. 44. Normalized Ge 3*d* spectra of the clean Ge(100) surface at 100 K (top) and 300 K (bottom) after Shirley background correction. The photon energy is 70 eV. The emission angle is 60°. The resultant fitting curves are shown by solid lines crossing the experimental data points (open circles). The solid line under each spectrumrepresents a residual curve. The bulk and surface components are given by shadowed spin-orbit doublets. The relative binding energy of the $3d_{5/2}$ peak of the bulk component is set to 0 eV.

Fig. 44 shows normalized spectra recorded at 300 K (bottom panel) and 100 K (top panel) as well as their decomposition. The 70-eV photon energy (the kinetic energy of photoelectrons is 35–37 eV) and grazing emission angle (θ_e = 60°) were chosen to enhance the surface sensitivity. The decomposition was made by using a standard least-squares fitting procedure with a linear combination of model spin-orbit Voigt functions. The spectra were fitted with five spin-orbit doublets that are a bulk component (*B*) and four surface-related components. Among those, Σ_u and Σ_d (herein we use notations from literature (Eriksson and Uhrberg 2010) are shifted by −0.54 and −0.10 eV relative to *B*. They have approximately similar intensities. A third component, Σ', has a SCLS of −0.20 eV and a slightly lower intensity as compared to Σ_u or Σ_d. Finally, a fourth component L' is shifted by 0.43 eV towards the higher binding energy. Its intensity is very low and amounts to 5–6% of the total intensity of Σ_u, Σ_d, and L'. The atomic origins of these components will be discussed below. The Lorentzian full width at half maximum and spin-orbit splitting are 0.150 and 0.594 eV for all the components, respectively. The branching ratio was allowed to vary slightly (by ±10%) around 0.667, which is the theoretical value for the 3*d* level, due to the possible diffraction effects. It is remarkable that despite this flexible constraint, the average branching ratio was found to be 0.671, i.e., it differs from the ideal one (2:3) by only 0.6%.

The Gaussian width (GW) of the Σ_u component can be determined accurately by analyzing the lower-binding-energy tail of spectra. At 100 K the GW of Σ_u is found to be 0.163 eV. The GWs of *B* and Σ_d are 0.218 and 0.208 eV, respectively. The minor broadening of *B* and Σ_d suggests that each of these components is contributed by inequivalent Ge atoms with slightly different core-level binding energies. The GW of Σ' is 0.147 eV and that of L' is about 0.3 eV. At 300 K the GW of *B* is 0.288 eV, and those of Σ_u, Σ_d, Σ' and L' are 0.304, 0.326, 0.328, and 0.343 eV, respectively. The above fitting parameters, such as spin-orbit splitting, branching ratio, Lorentzian width, and GW, are taken into account in the analysis of Yb-adsorbed Ge(100) surface.

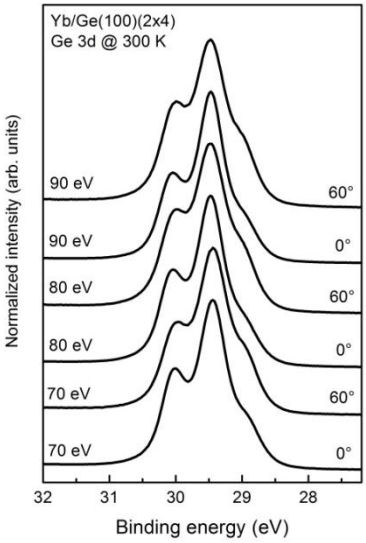

Fig. 45. Normalized raw Ge 3*d* spectra of Yb/Ge(100)(2×4) surface at 300 K at various photon energies and emission angles.

Raw Ge 3d spectra of Yb/Ge(100)(2×4) reconstruction are shown in Fig. 45. They were measured at various photon energies and emission angles at 300 K. Each spectrum is normalized to its maximum. As these spectra are rather featureless and do not change much upon variation of experimental conditions, it is difficult to solve how many surface components contribute to the non-fitted spectral lines. Roughly, the SCLSs of main surface-related components can be evaluated in Fig. 46, where a difference spectrum is represented by dashed line. This spectrum is obtained by subtracting a more bulk-sensitive spectrum at ($h\nu$, θ_e) = (70 eV, 0°) from a more surface-sensitive spectrum at ($h\nu$, θ_e) = (70 eV, 60°) (shown by solid lines). The difference spectrum has a maximum (a positive sign) at 29 eV and a minimum (a negative sign) at 31.1 eV. The maximum is caused by pronounced surface emission, i.e., $3d_{5/2}$ peak(s) of surface components, whereas the dominant contribution to the minimum is the $3d_{3/2}$ peak of the bulk component. Thus, we presume that the (2×4) reconstruction mainly shifts the surface emission to the lower binding energy relative to the bulk.

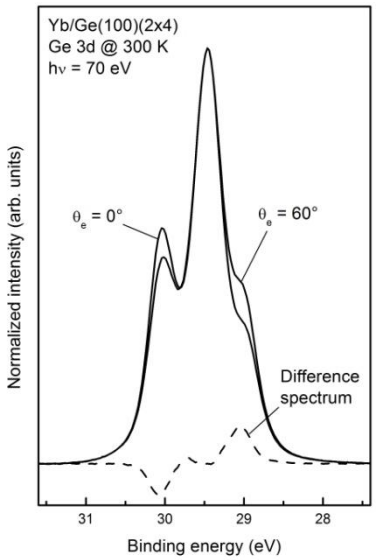

Fig. 46. Difference spectrum of Yb/Ge(100)(2×4) (dashed line) obtained by subtracting the spectrum at ($h\nu$, θ_e) = (70 eV, 0°) from the spectrum at ($h\nu$, θ_e) = (70 eV, 60°). The latter spectra are shown by solid lines. They are represented after the Shirley background removal correction.

The fitting procedure for the spectra in Fig. 45 was similar to that of the clean surface. It should be mentioned that all true SCLSs originating from the different bonding sites in such large unit cell as (2×4) can by no means be resolved in experiment because of the limited energy resolution. Consequently, our analysis should not necessarily be a search for all possible surface components for the (2×4) reconstruction. Rather, it is more important to understand the key characteristic features of the spectra by using a minimum number of components in the analysis. Obviously, the other criteria the fitting should meet are (i) the independence of SCLSs on $h\nu$ and θ_e, and (ii) physically reasonable GWs of the components.

On this basis, we restricted our analysis by using three surface components in total, although the GWs of some of them were somewhat increased. In this fitting scheme the SCLSs were independent on the photon energy and the emission angle (this was not the case in the fitting schemewith two surface components), and the GWs were slightly increasing with the photon energy due to the variation of resolution. In Fig. 47 the fitted spectra at ($h\nu$, θ_e) = (70 eV, 60°) and (90 eV, 60°) are illustrated. The surface-related components are labeled *S*1, *S*2, and *S*3. All of

them are shifted to the lower binding energy. The SCLSs are −0.51,−0.39, and −0.15 eV, respectively. The GW of the bulk component is 0.290 and 0.313 eV at the photon energy of 70 and 90 eV, respectively. The GWs of surface components range between 0.30 and 0.35 eV at $h\nu$ = 70 eV and 0.31 and 0.36 eV at $h\nu$ = 90 eV. Thus, the (2×4) reconstruction shifts the Ge 3*d* emission towards the lower binding energy region relative to the bulk.

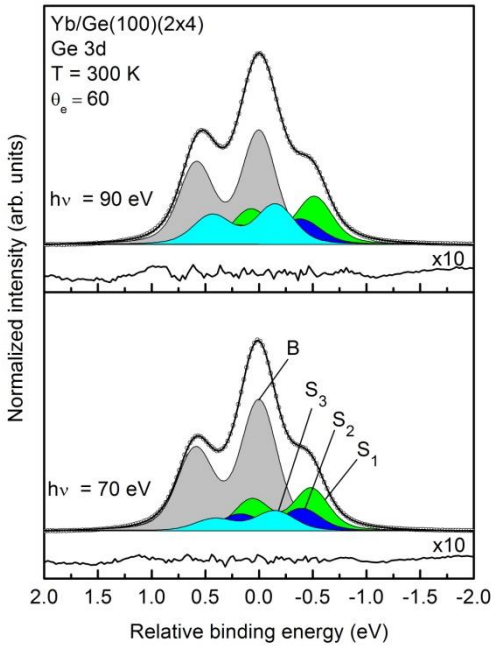

Fig. 47. Decomposed Ge 3*d* spectra of Yb/Ge(100)(2×4) taken at θ_e = 60° and $h\nu$ = 70 and 90 eV. The experimental data are shown by open circles. The bulk and surface components are given by shadowed doublets. The fitting curve and residual for each spectrum are shown by solid lines. The residual curves are multiplied by factor of 10.

3.3.2.2. Atomic structure

Our measurements of Yb 4*f* emission from the (2×4) surface (not shown here) indicated that the adsorbate atoms are completely divalent. This implies that three Yb atoms donate six electrons to the Ge substrate in the (2×4) unit cell, similar to the case of Yb/Si(100)(2×4) reconstruction. Prior to the analysis of

Yb/Ge(100)(2×4), we briefly summarize the findings for the closely related (2×4) and (2×3) structures induced by Yb (see Subsection 3.3.1) and other RE (Eu and Sm) on the Si(100) (Katkov and Nogami 2003; Kuzmin et al. 2003[a]; 2005[b]; 2008; 2011[b]; Ohbuchi and Nogami 2005; Punkkinen et al. 2009; Shinde et al. 2009). It is found that the Si(100)(2×4) and -(2×3) structures include, respectively, three and two metal atoms per unit cell and tend to dimerization in the topmost substrate layer. There are three Si dimers in the (2×3) cell and four Si dimers in the (2×4) one. In each structure, one dimer is buckled, i.e., its axis is not parallel to the surface, and the others are virtually symmetrical. The dimer axes are aligned along the [011] direction and the dimers form rows running along the [0-11] direction. Two patterns of the dimer rows are possible. In a more symmetrical pattern, called (2×*n*)-II (*n* = 3 or 4), the dimers are built up in perfectly straight rows. The other pattern, called (2×*n*)-I, has a more asymmetric form, where the perfect dimer rows are broken by a shift of every third dimer for *n* = 3 and every fourth dimer for *n* = 4 by Si unit length a_{Si} in the [011] direction. The total energy of (2×*n*)-II is lower than that of (2×*n*)-I.

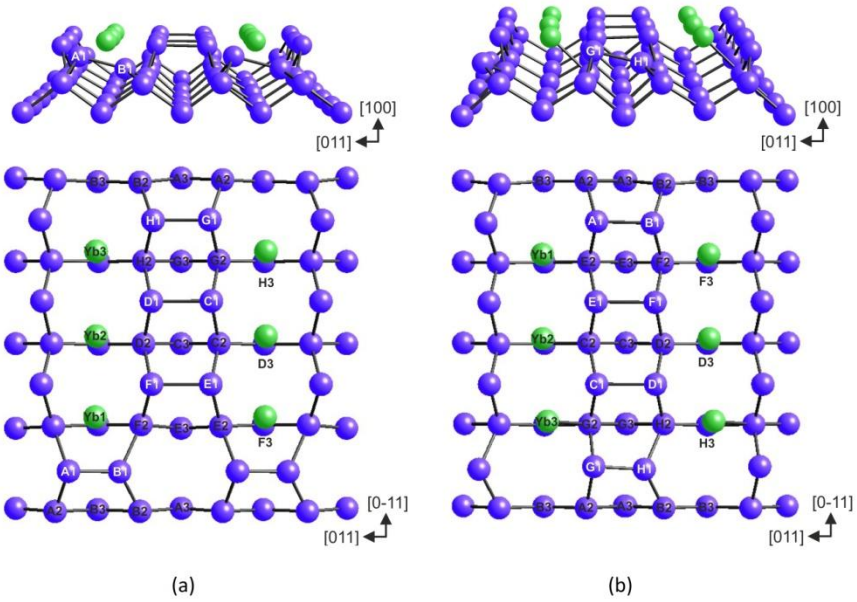

Fig. 48. (a) (2×4)-I and (b) (2×4)-II models of Yb/Ge(100). (top) Perspective view. (bottom) Top view. The metal atoms are labeled Yb1, Yb2, and Yb3. The first-layer Ge atoms are labeled A1–H1. The second-layer and third-layer atoms are labeled A2–H2 and A3–H3, respectively.

The total-energy calculations of the Yb/Ge(100)(2×4) atomic geometry showed that the above tendencies are generally valid for the Ge substrate, and that the (2×4)-I and (2×4)-II structures are very stable on the Ge(100) from the energetic viewpoint. However, in contrast to Si, the energy difference between these structures is extremely small (a few meV per (1×1) surface area). Therefore, we suggest that the (2×4)-I and (2×4)-II patterns are degenerate on the Yb/Ge(100)(2×4), and most likely a mixture of these patterns can be realized in experiment. The fully optimized (2×4)-I and (2×4)-II arrangements are illustrated in Fig. 48. Each (2×4) unit includes four Ge dimers in the first layer, which are Ge(A1)–Ge(B1), Ge(C1)–Ge(D1), Ge(E1)–Ge(F1), and Ge(G1)–Ge(H1), and three metal atoms labeled Yb1, Yb2, and Yb3. The Ge(A1)–Ge(B1) dimer in the (2×4)-I arrangement (Fig. 48(a)) is shifted by Ge unit length (a_{Ge} = 4.00 Å) in the [011] direction. The favorable site for the metal atoms is T3, which is similar to the case of Si (Subsection 3.3.1.3). The T3 site located just above the third-layer atom B3 remains unoccupied leaving a vacancy in the Yb rows (i.e., a missing Yb atom). The Ge dimers neighboring to this vacancy are Ge(A1)–Ge(B1) and Ge(E1)–Ge(F1) in the (2×4)-I, and Ge(A1)–Ge(B1) and Ge(G1)–Ge(H1) in the (2×4)-II.

Table 7. Some properties of Ge dimers in the (2×4)-I and (2×4)-II motifs. Δ*z* is the vertical distance between the atoms of each dimer. *L* is the dimer bond length. The tilted dimers are marked by asterisk.

Dimer	Δz (Å)	*L* (Å)
(2×4)-I		
Ge(A1)-Ge(B1)*	−0.63	2.41
Ge(C1)-Ge(D1)	0.01	2.83
Ge(E1)-Ge(F1)	0.05	2.80
Ge(G1)-Ge(H1)	0.03	2.68
(2×4)-II		
Ge(A1)-Ge(B1)	0.03	2.68
Ge(C1)-Ge(D1)	0.09	2.83
Ge(E1)-Ge(F1)	0.01	2.85
Ge(G1)-Ge(H1)*	−0.57	2.44

Similar to the Si dimers in the (2×4) and (2×3), the Ge dimers are structurally and electronically inequivalent. Table 7 shows the vertical separations (Δ*z*) in the

pairs of atoms forming each Ge dimer as well as the dimer bond lengths (*L*) for the (2×4)-I and (2×4)-II structures in Fig. 48. In the former structure, the Ge(A1)–Ge(B1) dimer is significantly tilted (Δ*z* = -0.63 Å), whereas the other dimers are practically unbuckled (Δ*z* = 0.01-0.05 Å). In the latter structure, the tilted configuration (Δ*z* = -0.57 Å) is found for the Ge(G1)–Ge(H1) dimer, and the other dimers are almost symmetrical (Δ*z* = 0.01-0.09 Å). Thus, the Yb/Ge(100)(2×4) surface includes one buckled and three unbuckled Ge dimers. The bond length is shortest in the buckled dimers (2.41-2.44 Å). In the other dimers, it ranges from 2.68 to 2.85 Å. Within the second layer, the overall buckling of the plane of Ge atoms is 0.20 Å in the (2×4)-I and 0.31 Å in the (2×4)-II. For the third atomic layer, the buckling further decreases. The second-layer Ge(A2) and Ge(B2) atoms are slightly lifted up above the other second-layer atoms because of the missing Yb atom above the Ge(B3) atom.

The height-level differences of Yb atoms are very limited and range within 0.077 Å in the (2×4)-I and 0.043 Å in the (2×4)-II. In the latter structure, the lateral displacements of Yb atoms from the ideal T3 positions are insignificant either. As shown in Fig. 48(b), the distance between Yb1 and Yb2 is different from the Ge lattice constant by 1.23% and the distance between Yb2 and Yb3 by−0.75%. Interestingly, related RE/Si(100) structures have slightly more significant distortion in metal rows (Kuzmin et al. 2011[b]; Shinde et al. 2009). This difference between RE/Si(100) and -Ge(100) systems can arise from the relation of atomic sizes of adsorbates (e.g., an atomic diameter of Yb is 3.88 Å) and the unit length parameters of the substrates (i.e., 3.84 Å for Si and 4.00 Å for Ge). In the Yb/Ge(100)(2×4)-I structure, the distortion of Yb row is more pronounced. The distance between Yb1 and Yb2 is different from the Ge lattice constant by −4.68% and the distance between Yb2 and Yb3 by−0.04%.

Ge 3*d* core-level shifts have been calculated for both (2×4)-I and (2×4)-II structures within the initial-state and complete-screening models, giving further support to the above models. These results are presented in detail elsewhere (Kuzmin et al. 2013), and for the sake of briefness, we omit these data here. The comparison of calculated and measured SCLSs indicates that the relaxation effects in the complete-screening model are very important for the first Ge layer. The relaxation effects also contribute to the SCLSs of the second-layer, third-layer, and fourth-layer atoms. The amount of the complete screening correlates well with initial-state SCLSs for respective bonding sites, i.e., the properties of respective atoms in the initial state. The superscreening occurs for the Ge atoms with most positive initial-state SCLSs,whereas the inferior screening is found for the Ge atoms with most negative initial-state SCLSs. The above correlation are

fruitful for the interpretation of Ge 3*d* line shapes and lack of positively shifted components for the clean and (2×4) surfaces.

3.4. Yb/Si(100)(2×6)

When the metal coverage of Yb/Si(100) exceeds the range where the (2×3) and (2×4) reconstructions are observed, the LEED pattern undergoes the qualitative changes: a new (1×6) LEED structure appears. Fig. 35(d) presents the LEED pattern observed at 0.5 ML. The (1×6) and (6×1) unit cells are marked by the white rectangles. The weak half-order streaks shown by arrows can be seen in this pattern, thus suggesting the 2× ordering. Further it will be shown by STM that this structure actually has the (2×6) unit cell. For this reason, we will use the notation '(2×6)' hereafter.

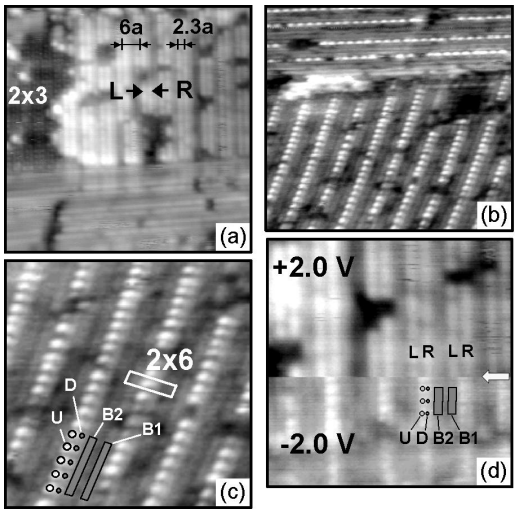

Fig. 49. The empty and filled-state STM images of Yb/Si(100) at 0.5 ML. (a) 28 nm × 28 nm, V_S = 2.0 V, I_t = 0.16 nA. The (2×3) phase is seen as a dark area on the left. (b) 18.5 nm × 17 nm, V_S = 2.1 V, I_t = 0.15 nA. (c) 9.5 nm × 9.5 nm. The 2×6 unit cell is shown. (d) 13 nm × 13 nm, V_S = -2.0 V / 2.0 V, I_t = 0.16 nA. L, R, U, D, B1, and B2 features are marked. The other details can be found in the text.

An empty-state STM image obtained at 0.5 ML is shown in Fig. 49(a). It reveals double striped features composed of two adjacent bright single streaks, R (right) and L (left), aligned along either [0-11] or [011] direction. The vertical

position of these strikes is about (2.0 Å) higher than that of the (2×3) Yb phase of which small domain is adjacent to the (2×6) structure. This difference indicates that the topmost layer in the reconstruction formed at 0.5 ML is noticeably lifted up compared to the (2×3) phase. The spacing between the neighboring double striped features in the (2×6) reconstruction is $6a_{Si}$ (about 23 Å), which agrees well with ×6 periodicity observed in LEED (Fig. 33(d)). A length of the double ×6 features is restricted by vacancies appeared in the STM image as randomly distributed dark areas. The distance between the adjacent single streaks R and L is $2.3a_{Si}$ (about 8.8 Å). The fine structure of the single streaks, e.g., protrusions, is not resolved.

Fig. 49(b) shows a filled-state STM image of the same surface. First of all, the white rows aligned along either the [0-11] or [0 1 1] direction can be found in this image. The spacing between these rows is $6a_{Si}$, and the rows are composed of the single chains of very bright protrusions (denoted by U) and the other neighboring ones of smaller, not so bright, protrusions (denoted by D) (Fig. 49(c)). The periodicity of the both U and D protrusions along a row is $2a_{Si}$. Such double rows are accompanied by the faint unresolved stripes B1 and B2 (a pair of such stripes per the unit length of this reconstruction along the direction of ×6 ordering). Finally, the dark lines lie in between the adjacent stripes. Thus, the periodic structure observed in the filled-state STM images reveals the (2×6) unit cell. In fact, such a periodicity supports the existence of the half-order LEED streaks at 0.5 ML (Fig. 33(d)). Therefore, we suggest the (2×6) unit cell to be a basic building block of Yb-stabilized Si(100) surface at 0.5 ML. Very similar STM results in filled-state mode were obtained for this reconstruction elsewhere (Katkov and Nogami 2003).

A direct evidence for the difference between the STM images in filled and empty states for the (2×6) reconstruction can be obtained in Fig. 49(d). This image is taken with a sample bias reverse and shows the mutual lateral distribution of the aforementioned STM features observed in both STM modes.

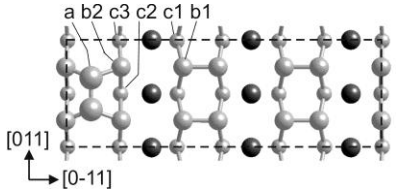

Fig. 50. Atomic model of Yb/Si(100)(2×6). The unit cell is outlined. The Yb atoms are shown by large black balls. The notations '*a*', '*b*', and '*c*' denote the Si atoms in the topmost, first, and second layers.

A careful inspection of the above STM images for the Yb/Si(100)(2×6) allows us to propose and test an atomic model for this reconstruction. This model is obtained based on the DFT calculations. It is shown in Fig. 50. The model is equivalent to the (2×1) reconstruction, except that there is one additional Si dimer above the underlying full Si layer and consequently there are Si dimers in two directions. The metal atoms are adsorbed at valley-bridge sites. This structure leads to a quite low total energy and semiconducting electronic structure if the Yb atoms are divalent. Several other atomic structures were also tested but they have higher total energies. Furthermore, STM images simulated for this structure (Fig. 51) are in good agreement with the experimental ones (Katkov and Nogami 2003; Kuzmin et al. 2003[a]; Cui and Nogami 2009). Therefore, the proposed model is a prominent candidate for the atomic structure of Yb/Si(100)(2×6).

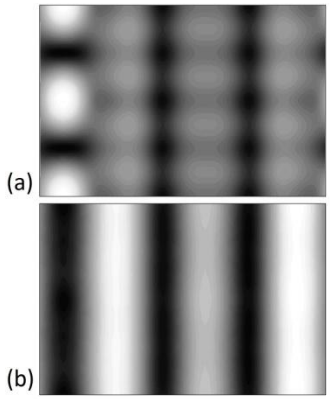

Fig. 51. STM images simulated for the (2×6) model in Fig. 50. Energy ranges: (a) 2.0 eV below the Fermi energy (filled states) and (b) 2.0 eV above the Fermi energy (empty states).

It is essential that in contrast to the (2×3) and (2×4) models discussed in Subsection 3.3.1.3, the (2×6) model does not contain buckled Si dimers. As shown in Fig. 50, it features unbuckled, mutually orthogonal, dimers formed by the first-layer Si atoms *b*1 and topmost-layer Si atoms *a*. The buckled and unbuckled configurations of Si dimers cannot be reliably verified on the basis of STM measurements at RT because this technique is relatively slow (see Section 2). In contrast, CLPES provides a 'snapshop' of Si dimer configuration and can be used to establish whether the Si dimers have tilted or symmetrical configuration. One can expect that the Si 2*p* binding-energy splitting of the dimer-up and dimer-

down atoms is eliminated after the dimer symmetrization on the Yb/Si(100)(2×6), leading to the narrowed Si 2*p* emission. This itself can be an interesting issue shedding light on ties of the surface structure and the Si 2*p* line shape. Moreover, VBPES and Yb 4*f* photoemission can be useful supplementary tools to verify the atomic structure of Yb/Si(100)(2×6).

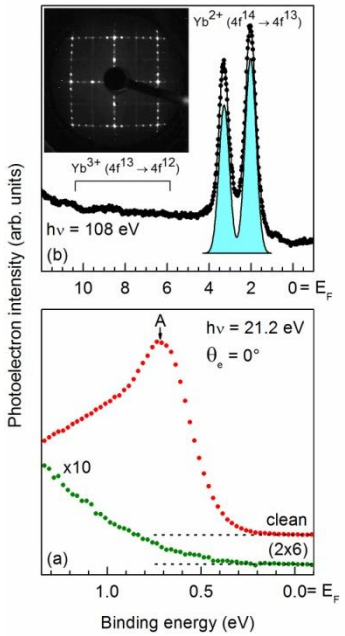

Fig. 52. (a) Normal-emission valence spectra for clean Si(100) and Yb/Si(100)(2×6) measured with $h\nu$ = 21.2 eV at RT. The spectra are normalized to the background intensity. The intensity of the (2×6) spectrum is multiplied by a factor of 10. (b) Yb 4*f* spectrum from the (2×6) reconstruction measured with $h\nu$ = 108 eV at 100 K. The raw data are represented by solid circles. The Yb $4f^{13}$ final state is fitted by a single component shown by shadowed spin-orbit-split doublet. The inset illustrates the (2×6) LEED pattern at 100 K. The electron energy is 45 eV.

Fig. 52(a) illustrates changes in the VB region of the Si surface upon the formation of Yb/Si(100)(2×6). The dominant feature of the clean substrate (the top spectrum in Fig. 52(a)) is a sharp peak at about 0.7 eV (labeled A), which is due to the dangling-bond surface state associated with the up atom of the asymmetric dimers (Johansson et al. 1990). When the (2×6) reconstruction is

formed, this state is clearly suppressed (the bottom spectrum in Fig. 52(a)), indicating that the asymmetric dimer arrangement is broken.

Yb 4*f* spectrum and LEED pattern from the Yb/Si(100)(2×6) at 100 K are shown in Fig. 52(b). In full agreement with the theoretical analysis and model in Fig. 50, the Yb atoms are completely divalent. The Yb $4f^{13}$ final state doublet can be fitted by a single component with a spin-orbit splitting (SOS) of 1.2 eV, suggesting similar bonding sites for the Yb atoms in this reconstruction. The 2× periodicity appears in the form of half-order LEED streaks that have a similar intensity at 300 and 100 K. The lack of 2× periodicity spots is consistent with STM observations (Fig. 49), and it can be explained in terms of the "out-of-the-phase" shift of topmost-layer Si dimer rows in Fig. 50.

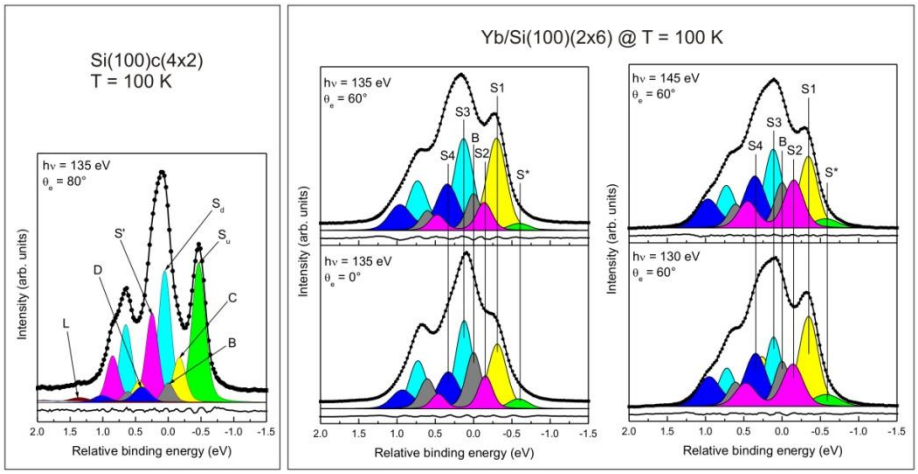

Fig. 53. Si 2*p* spectra of clean Si(100) (left panel) and Yb/Si(100)(2×6) (right panel) at 100 K. The spectra are taken at $h\nu$ =135 eV and θ_e =80° for the clean surface and $h\nu$ =130, 135, and 145 eV and θ_e = 0° and 60° for the Yb-adsorbed surface. The fitting results (SCLS components) are shown by shadowed doublets. The (2×6) spectra are normalized by their maxima.

In Fig. 53 we show normalized Si 2*p* spectra (filled dots) and their decompositions (solid lines) obtained for the (2×6) reconstruction at various $h\nu$ and θ_e (right panel) along with that of the clean Si(100) surface (left panel) at 100 K. (Note at the clean surface has the c(4×2) rather than (2×1) reconstruction at this temperature.) As the Si 2*p* fitting procedure for the Si(100) is well known (Uhrberg 2001; Koh et al. 2003; Eriksson and Uhrberg 2010), the analysis of the

clean spectrum in Fig. 53 provides justified parameters for fitting the (2×6) spectra. For the clean substrate, we found seven spin-orbit split Voigt components (*B*, S_u, *C*, S_d, *S*, *D*, and *L* shadowed doublets). The SCLS of S_u, *C*, S_d, *S*, *D*, and *L* are −0.48, −0.18, 0.06, 0.24, 0.39, and 1.35 eV relative to *B*. The Lorentzian full width at half maximum, which varies in different studies (Koh et al. 2003), is determined from the analysis of the lower-binding-energy tail of S_u that has no overlap with the other components. The value was found to be 67 meV and then fixed for all the components. The spin-orbit splitting is 610 meV. The branching ratio is allowed to vary around 0.50 within 10% due to the possible diffraction effects. The GWs of *B*, S_u, S_d, *C*, *S*, *D*, and *L* are 175, 203, 188, 192, 202, and 346 meV, respectively. The above results are consistent with previous findings (Uhrberg 2001; Koh et al. 2003; Eriksson and Uhrberg 2010) and the origin of identified components was interpreted ibidem. We note that very grazing emission angle 80°allowed us to highly enhance the surface sensitivity and obtain Si 2*p* emission which is largely contributed by the topmost layer, i.e., the up (S_u) and down (S_d) atoms of the asymmetric dimers. The bulk contribution (*B*) is so low that the spectrum is almost completely due to the first three atomic layers and has almost pure surface origin.

To fit the (2×6) spectra, at least five spin-orbit-split components *B*, *S*1, *S*2, *S*3, and *S*4 are required. They can reasonably reproduce these spectra except for their lower binding-energy tail. Such a fitting scheme cannot be improved even by an increase in GW. Therefore, a minor sixth component S^* was added. The results are shown in the right panel of Fig. 53. The five SCLS are −0.32 (*S*1), −0.15 (*S*2), 0.12 (*S*3), 0.34 (*S*4), and −0.58 eV (S^*). The GW of *B* is 179 meV, and that of the surface components varies between 209 and 277 meV. The Lorentzian width, spin-orbit splitting, and branching ratio are the same as for the clean surface. It is essential that the SCLS and GW of *S*1, *S*2, *S*3, and *S*4 are very similar in the two fitting schemes with five and six components, and therefore, we conclude that the *S*1, *S*2, *S*3, and *S*4 are due to the (2×6) reconstruction irrespective of the fitting scheme. In contrast, the origin of S^* is clearly different because its intensity is significantly smaller than those of *S*1−*S*4 and, moreover, it is not reproduced by DFT calculations, as seen below. The S^* most likely originates from defects on the Yb/Si(100) surface, as found by STM (Fig. 49). The further introducing of additional components does not improve the fitting.

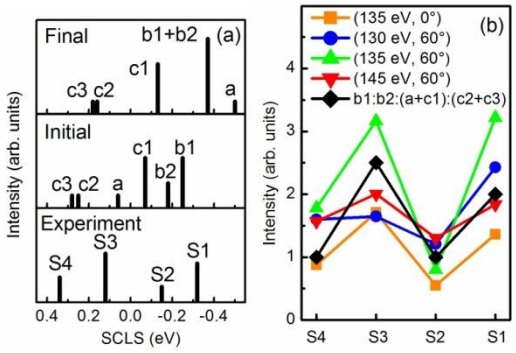

Fig. 54. (a) Comparison of (a) calculated and experimental SCLSs and (b) the intensity ratio of *S*1:*S*2:*S*3:*S*4 at various experimental conditions ($h\nu$, θ_e) and the number ratio of respective Si atoms. For details see the text.

To interpret the *S*1−*S*4, theoretical SCLSs were evaluated with DFT by using the average electrostatic potential at the core of the Si atoms. The bulk reference value was obtained by averaging from the layers 5–7 in the slab. The comparison of calculated and experimental data is given in Fig. 54(a). The vertical bars point out the values of SCLSs. In the bottom panel the bar height is proportional to the intensity of measured SCLSs at $h\nu$ = 135 eV and θ_e = 0°. In the middle and top panels the bar height is proportional to the number of corresponding Si atoms in the (2×6) unit cell in Fig. 50. Within the initial state model, the calculated SCLSs are 0.06 eV for the top-layer Si atom *a*, 0.25 and -0.18 eV for the first-layer Si atoms *b*1 and *b*2, and -0.07, 0.25, and 0.28 eV for the second-layer Si atoms *c*1, *c*2, and *c*3, respectively. The energy ranges of these SCLSs and measured ones agree very well (-0.25 eV to 0.28 eV and -0.32 eV to 0.34 eV, respectively). Taking into account the complete screening effects in the final state model, the SCLSs are -0.50 eV for the atom *a*, -0.37 eV both for *b*1 and *b*2, and -0.13, 0.16, and 0.18 eV for *c*1, *c*2, and *c*3, respectively. (Note that there is an uncertainty (~0.1 eV) in evaluating the final state SCLSs due to the non-accurate bulk reference value (Punkkinen et al. 2008)). Roughly, the final state values tend to move systematically toward the lower binding energy as compared to the respective initial state values while the general trend, i.e., the energy difference between the highest and lowest SCLS remains the same. A more detailed analysis, however, shows that the final state model describes the (2×6) spectra poorer than the initial state model, and also that the effect of shifting final state values toward the lower binding energy is overestimated. Hence, we further consider the initial state scenario for the (2×6) surface. This differs from the case of clean Si(100)

where the Si 2*p* data are better interpreted within the final state scheme (Pehlke and Scheffler 1993; Eriksson and Uhrberg 2010). It is believed that the initial state model is reasonable for the Yb/Si(100)(2×6) because of charge redistribution at this reconstruction (see below), leading to the symmetrical dimer arrangement. We notice that the screening effects are most significant for the topmost-layer atoms *a* in Fig. 50. This agrees with the final state results for the clean Si(100) where the gain in relaxation energy is largest for the topmost atoms, especially for the down atom of the asymmetric dimer (Pehlke and Scheffler 1993; Eriksson and Uhrberg 2010).

It is also seen that the intensity ratios of measured SCLSs correlate with the number ratio of the Si atoms that are suggested to be the origins of these SCLSs in Fig. 54(a). Based on the initial state results, we assume that the Si atoms *b*1 contribute to *S*1, the Si atoms *b*2 to *S*2, the Si atoms *a* and *c*1 to *S*3, and the Si atoms *c*2 and *c*3 to *S*4. Then the number ratio of *b*1:*b*2:(*a*+*c*1):(*c*2+*c*3), which is 4:2:5:2, is well consistent with the intensity ratios of *S*1, *S*2, *S*3, and *S*4 at different experimental conditions, as shown in Fig. 54(b). For example, the *S*1:*S*2:*S*3:*S*4 ratios for $h\nu$ = 135 eV are 2.4:1:3.1:1.6 and 4:1:3.9:2.2 at θ_e = 0° and 60°, respectively, agreeing clearly with the atomic number ratio of *b*1:*b*2:(*a*+*c*1):(*c*2+*c*3). Thus, the measured and calculated Si 2*p* data are in good agreement, supporting the (2×6) structure of Fig. 50.

Next, the SCLS ranges measured for different Si reconstructions are worth comparing. The SCLS range for the Yb/Si(100)(2×6) is 0.66 eV. It is noticeably narrower than those of Yb/Si(100)(2×3)/(2×4) (0.82 eV) (see Subsection 3.3.1.1), Eu/Si(100)(2×3) (1.05 eV) (Kuzmin et al. 2005[b]), and Sm/Si(100)(2×3) (0.80 eV) (Kuzmin et al. 2011[b]), and it is smaller than that of the clean Si(100) (0.87 eV) as well. Most likely, the difference is due to the lack of buckled Si dimers at the Yb/Si(100)(2×6) and the presence of buckled dimers at the Yb/Si(100)(2×3)/(2×4), Eu- and Sm/Si(100)(2×3), and clean Si(100) surfaces. In other words, the narrowed Si 2*p* emission from the Yb/Si(100)(2×6) can be reasonably explained by the symmetrization of Si dimers in the model of Fig. 50.

Now, the question why the dimers are symmetrical in the (2×6) phase raises. The (2×6) structure of Fig. 50 was tested by moving the dimer atoms into the "buckled" positions. After the full optimization of such a structure by DFT calculations, it is found that the dimer buckling does not exceed 0.8 pm, meaning that the dimers are truly symmetrical on the Yb/Si(100)(2×6) with high precision. On the contrary, the fully optimized (2×3) and (2×4) structures of Yb-, Eu-, and Sm/Si(100) contain one asymmetric dimer per surface unit. In these structures, the uppermost Si layer is dimerized with three (four) dimers per unit cell. One of these dimers is buckled, while the rest of dimers are symmetrical. The adsorbate

atoms are divalent and their coverage is 1/3 and 3/8 ML, respectively. Therefore, the surface can be donated by four [six] electrons from the adsorbate per (2×3) [(2×4)] unit cell.

On this basis, we propose the 'dimer-symmetrization' rule. It suggests that the stabilization of the symmetrical dimer arrangement on Si(100) requires the charge transfer of two electrons from the metal to the substrate per dimer. In fact, in the (2×6) reconstruction there are five Si dimers and six Yb atoms that can donate 12 electrons to the surface per unit cell, and therefore, the total number of donated electrons is enough for the symmetrization of all dimers. Tentatively, the above two-electron transfer picture implies that two electrons donated from the metal saturate the half-filled dangling bonds of the dimer atoms, removing the charge rearrangement between the up and down atoms of a buckled dimer. The core-level binding-energy difference of the first and topmost-layers dimer atoms in the (2×6), i.e., the atoms *b*1 and *a*, respectively, is significant (0.3–0.4 eV). This infers that the atom *b*1 gains more electron charge than the atom *a*. The difference is thought to be due to that the distance between the atom *b*1 and the neighboring Yb atom is shorter than the distance between the atom *a* and the neighboring Yb atom.

4. CONCLUSION

Using combined experimental and theoretical techniques, the atomic and electronic structures of surface reconstructions formed at earliest stages of Yb/Si and Yb/Ge interface formation have been studied. On both Si(111) and Ge(111) surfaces, the lowest-coverage reconstruction stabilized by Yb atoms is the (3×2) phase with the adsorbate coverage of 1/6 ML. This reconstruction is interpreted within the HCC structure and involves Si honeycomb chains with the unusual Si=Si and Ge=Ge double bonds, which are separated by empty channels. Such a motif of Si or Ge substrate gives rise to the 3× periodicity. The channels in between the honeycomb chains serve for the accommodation of metal atoms. In the proposed models, the Yb atoms occupy every second T_4 site or slightly shifted from it, leaving to the double periodicity along a metal row. The stability of HCC reconstruction is controlled by the electron counting rule: the HCC arrangement is stabilized by the donation of one electron from the adsorbate per (3×1) mesh of Si or Ge surface. This rule is common for various adsorbates (monovalent and divalent species), including RE and AEM atoms forming the 1/6-ML (3×2) structure and AM atoms forming the 1/3-ML (3×1) structure on Si(111) and Ge(111). The violation of the electron counting rule can induce defects at the

interface; e.g., one missing Yb atom can destroy two (3×1) units, leading to defect(s) involving up to six Si atoms.

At higher coverages, Yb forms intermediate (n×1) reconstructions (e.g., (5×1), (7×1), (9×1) etc.) composed of Si honeycomb and Seiwatz chains. Their structural unit is (H, m×S) where $m = (n\text{-}1)/2 - 1$ and the saturate coverage is (n-1)/2n ML. Although the saturate coverage of intermediate reconstructions implies that each T_4 (or H_3) adsorption site in the empty channels in between Si honeycomb and Seiwatz chains is occupied by adsorbate atoms, the ×2 periodicity is assumed for these phases in order to explain their semiconducting electronic structure. The ×2 periodicity can be adopted by the displacement of every second Yb atoms from the T_4 (H_3) site or/and the deformation of Si honeycomb chains. The periodicity doubling is not resolved in STM but can be found in LEED, supporting that these reconstructions are actually (5×'2'), (7×'2'), (9×'2') etc. Finally, the series of Yb-induced reconstructions is terminated by the (2×1) structure composed of Si Seiwatz chains.

On the (100) surfaces of Si and Ge, ytterbium forms (2×3), (2×4), and (2×6) structures. The first two structures are observed at ≤ 1/3 ML and the latter at 1/2 ML. Atomic models with saturation coverages of 1/3, 3/8, and 1/2 ML, respectively, are proposed for these structures. One of the main properties of such models is dimerization in the top layer(s) of the substrate. In contrast to the clean Si(100) and Ge(100) surfaces, however, there are both symmetrical and buckled dimers in the (2×3) and (2×4) unit cells, while only symmetrical dimers are found in the (2×6) unit cell. On the basis of these results, we have proposed the dimer symmetrization rule: the alignment of Si-Si (Ge-Ge) dimers parallel to the (100) surface plane requires the donation of two electrons from the adsorbate to the substrate per dimer. Thus, 1/2 ML of divalent Yb atoms can symmetrize all the dimers on both surfaces, leading to passivation of such substrates.

Understanding of the presented Yb-induced reconstructions is also relevant to fabrication of metal contacts in semiconductor technology. First it is however worth noting a clear gap between the traditional surface science approach (presented here) and that used in the semiconductor technology: the latter does not typically include any vacuum heating step before the metal growth but a metal film is deposited on a wet chemical etched Si or Ge surface. From surface science viewpoint a chemically etched surface can be indeed free of most contaminants but it is still far from crystalline or well-ordered. The incorporation of vacuum technology into a technological process has been presented recently (Kuzmin et al. 2019). Even if the high-temperature vacuum annealing cannot be used in technology in the same way as in surface science, low temperature vacuum treatment most likely improves a starting surface for metal deposition as well.

Toward that target, the reconstructions considered in this chapter provide first of all a fingerprint diffraction pattern for a high-quality surface because a poor quality semiconductor surface does not exhibit any reconstruction diffraction pattern. Furthermore, the reconstructions open a path to monitor the metal incorporation. The silicides have been already used to make low-resistivity contacts for the transistors of which dimensions have been scaled down very much during the last five decades. Indeed the epitaxial silicides allow one to control the dimensions or extension of the metal-semiconductor interface region which become tightened all the time. Obviously, the controlling crystal quality of the interface regions at atomic scale provides a way to decrease amounts of point defects induced by metal-semiconductor interactions. A decrease in the defect density at metal-semiconductor interface means an improved performance via reduced electrical losses.

ACKNOWLEDGMENT

First of all, the authors are very grateful to Marko Punkkinen, PhD, who made all DFT calculations in this study. We would like to thank the present and former members of our research team: Riitta Perälä, PhD, Riikka-Liisa Vaara, PhD, Jouko Lång, PhD (currently at Comptek Solutions), Johnny Dahl, PhD (currently at Comptek Solutions), Jaakko Mäkelä, PhD (currently at Comptek Solutions), Muhammad Yasir, PhD, Marja Ahola-Tuomi, PhD, Marjukka Tuominen, MSc (currently at Comptek Solutions), Juha-Pekka Lehtiö, MSc, Zahra Jahanshah Rad, MSc, and Esa Vuorinen, MSc. Also, the MAX-lab staff and Risto Punkkinen, PhD are acknowledged for their assistance. Finally, we thank Professors Kalevi Kokko, Juhani Väyrynen, Mikhail A. Mittsev, Mika Lastusaari, and Hele Savin for their valuable contributions to this study.

REFERENCES

Abbati, I., Braicovich, L., Carbone, C., Nogami, J., Lindau, I., Iandelli, I., Olcese, G., and Palenzona, A. 1987. «Photoemission Studies of Mixed Valence in Yb_3Si_5, YbSi and Yb_5Si_3: Equivalent Versus Inequivalent Yb Sites.» *Solid State Commun*. 62: 35-39.

Abukawa, T., Okane, T., Kono S. 1991. «Low energy electron diffraction and X-ray photoelectron diffraction study of the Cs/Si(001) surface: dependence on Cs coverage.» *Surf. Sci.* 256: 370-378.

Allen, F.G., and Gobeli, G.W. 1962. "Work Function, Photoelectric Threshold, and Surface States of Atomically Clean Silicon." *Phys. Rev.* 127: 150-158.

An, K.S., Park, R.J., Kim, J.S., Park, C.Y., Kim, C.Y., Chung, J.W., Abukawa, T., Kono, S., Kinoshita, T., Kakizaki, A., Ishii, T. 1995. «Mg-induced Si(111)3 × 1 structure studied by photoelectron spectroscopy.» *Surf. Sci.* 337: L789-L794.

Aarts, J., Hoeven, A.J., and Larsen, P.K. 1988. «Electronic structure of the Ge(111)-c(2×8) surface.» *Phys. Rev. B* 37: 8190-8197.

Baglin, J.E., d'Heurle, F.M., and Petersson, C.S. 1980. «The Formation of Silicides from Thin Films of Some Rare-Earth Metals.» *Appl. Phys. Lett.* 36: 594-596.

Baglin, J.E., d'Heurle, F.M., and Petersson, C.S. 1981. «Diffusion Marker Experiments with Rare-Earth Silicides and Germanides: Relative Mobilities of the Two Atom Species.» *J. Appl. Phys.* 52: 2841-2846.

Baski, A.A., Erwin, S.C., Turner, M.S., Jones, K.M., Dickinson, J.W., Carlisle, J.A. 2001. "Morphology and electronic structure of the Ca/Si(111) system." *Surf. Sci.* 476: 22-34.

Battaglia, C., Cercellier, H., Monney, C., Garnier, M.G., and Aebi, P. 2007. «Stabilization of silicon honeycomb chains by trivalent adsorbates.» *Europhys. Lett.* 77: 36003-p5.

Battaglia, C., Cercellier, H., Monney, C., Despont, L., Garnier, M.G., and Aebi, P. 2008. «Unveiling new systematics in the self-assembly of atomic chains on Si(111).» *J. Phys.: Conference Series* 100: 052078-4.

Blöchl, P.E. 1994. "Projector augmented-wave method." *Phys. Rev. B* 50: 17953-17979.

Bonet, C. and Tear, S.P. 2006. "Self-assembly of ultrafine nanolines upon Ho reaction with the Ge(001) surface." *Appl. Phys. Lett.* 89: 203119-3.

Braicovich, L., Abbati, I., Carbone, C., Nogami J., and Lindau, I. 1986. «Synchrotron Radiation Studies of The Effect of Thermal Treatment on The Si(111)-Yb Interfaces.» *Surf. Sci.* 168 : 193-203.

Bringans, R.D., and Höchst, H. 1982. "Electronic structure of Ge(111) and Ge(111): H from angle-resolved-photoemission measurements." *Phys. Rev. B* 25: 1081-1089.

Bringans, R.D., Uhrberg, R.I.G., and Bachrach, R.Z. 1986. «Surface and bulk electronic structure of Ge(111) c(2×8) and Ge(111):As 1×1.» *Phys. Rev. B* 34: 2373-2380.

Brodde, A., Bertrams, Th., and Neddermeyer, H. 1993. «Submonolayer- and monolayer-coverage structures of K/Si(100).» *Phys. Rev. B* 47: 4508-4516.

Castellarin-Cudia, C., Surnev, S., Ramsey, M.G., Netzer, F.P. 2001. "Surface structures of thallium on Ge(111)." *Surf. Sci.* 491: 29-38.

Ceperley, D.M. and Alder, B.J. 1980. "Ground State of the Electron Gas by a Stochastic Method." *Phys. Rev. Lett.* 45: 566-569.

Chelikowsky, J.R., and Cohen, M.L. 1976. «Nonlocal pseudopotential calculations for the electronic structure of eleven diamond and zinc-blende semiconductors.» *Phys. Rev. B* 14: 556-582.

Chen, Yong, Ohlberg, Douglas A.A., Medeiros-Ribeiro, Gilberto, Chang, Y. Austin, and Williams, R. Stanley. 2000. «Self-assembled growth of epitaxial erbium disilicide nanowires on silicon (001).» *Appl. Phys. Lett.* 76: 4004-4006.

Chi, K.S., Tsai, W.C., and Chen, L.J. 2003. «Evolution of Vacancy Ordering Structures in Epitaxial $YbSi_{2-x}$ Thin Films on (111) and (001)Si.» *J. Appl. Phys.* 93: 153-158.

Collazo-Davila, C., Grozea, D., Marks, L.D. 1998. «Determination and refinement of the Ag/Si(111)−(3×1) surface structure.» *Phys. Rev. Lett.* 80: 1678-1681.

Cui Y. and Nogami, J. 2009. "Ca induced reconstructions of the Si(001) surface." *Surf. Sci.* 603: 3072-3080.

Cui, Y., Nogami, J. 2011. "Thulium induced reconstructions of the Si(001) surface." *Surf. Sci.* 605: 2038–2044.

d'Heurle, F.M., and Gas, P. «Kinetics of Formation of Silicides: A Review.» 1986. *J. Mater. Res.* 1: 205-221.

Daimon, H., Ino, S. 1985. «Study of the Si(111) 7 × 7 surface structure by alkali- metal adsorption.» *Surf. Sci.* 164: 320-326.

Dávila, M.E., Molodtsov, S.L., Laubschat, C., and Asensio, M.C. 2002. «Structural determination of Yb single-crystal films grown on W(110) using photoelectron diffraction.» *Phys. Rev. B* 66: 035411-8.

DeJarld, Matthew; Campbell, Paul M.; Friedman, Adam L., Currie, Marc; Myers-Ward, Rachael L., Boyd, Anthony K., Rosenberg, Samantha G., Pavunny, Shojan P., Daniels, Kevin M.; and Gaskill, D.K. 2018. «Surface potential and thin film quality of low work function metals on epitaxial graphene.» *Scientific Reports* 8: 16487-11. doi:10.1038/s41598-018-34595-1.

Dillon, J. A., Jr., and Farnsworth, H.E. 1958. "Work Function and Sorption Properties of Silicon Crystals." *J. Appl. Phys.* 29: 1195-1202.

Einstein, T.L., Richards, H.L., Cohen, S.D., Pierre-Louis, O. 2001. "Terrace-width distributions and step-step repulsions on vicinal surfaces: Symmetries, scaling, simplifications, subtleties, and Schrödinger." *Surf. Sci.* 493: 460-474.

Engelhardt, H.A., Menzel, D. 1976. "Adsorption of oxygen on silver single crystal surfaces." *Surf. Sci.* 57: 591-618.

Engelhardt, I., Preinesberger, C., Becker, S.K., Eisele, H., Dähne, M. 2006. «Atomic structure of thin dysprosium-silicide layers on Si(111).» *Surf. Sci*. 600: 755–761.

Eriksson, P.E.J. and Uhrberg, R.I.G. 2010. "Surface core-level shifts on clean Si(001) and Ge(001) studied with photoelectron spectroscopy and density functional theory calculations." *Phys. Rev. B* 81, 125443-6.

Erwin, S.C. 1995. «New structural model for the alkali-induced Si(111)-(3×1) reconstruction from first principles.» *Phys. Rev. Lett.* 75: 1973-1976.

Erwin, S.C. and Weitering, H.H. 1998. «Theory of the "Honeycomb Chain-Channel" Reconstruction of M/Si(111)-(3×1).» *Phys. Rev. Lett.* 81: 2296-2299.

Fan, W.C., Ignatiev, A. 1990. «Metal-Adsorbate-Induced Si(111)-(1×3) Reconstruction.» *Phys. Rev. B* 41: 3592-3595.

Fan, W.C., Ignatiev, A. 1991. «Identification of ordered atomic structures of Ba on the Si(100) surface.» *Surf. Sci.* 253: 297-302.

Feenstra, R.M., Gaan, S., Meyer, G., and Rieder, K.H. 2005. «Low-temperature tunneling spectroscopy of Ge(111)c(2×8) surfaces.» *Phys. Rev. B* 71: 125316-16.

Frohn, J., Giesen, M., Poensgen, M., Wolf, J.F., Ibach, H. 1991. "Attractive interaction between steps." *Phys. Rev. Lett.* 67: 3543-3546.

Fukuda, T. 1994. «Determination of silver coverage on Si(111) 3×1(6×1)-Ag surfaces.» *Phys. Rev. B* 50: 1969-1972.

Gerken, F. 1983. «Calculated photoemission spectra of the 4*f* states in the rare-earth metals.» *J. Phys. F: Met. Phys.* 13: 703-713.

Grimley, T.B. 1967. "The electron density in a metal near a chemisorbed atom or molecule." *Proceedings of the Physical Society* 92: 776-782.

Grozea, D., Bengu, E., Collazo-Davila, C., and Marks, L.D. 1999. «Structure Determination of the Ge(111)-(3×1)Ag Surface Reconstruction.» *Surface Review and Letters* 06: 1061-1065.

Guichar, G.M., Garry, G.A., and Sébenne, C.A. 1979. «Photoemission yield spectroscopy of electronic surface states on germanium (111) surfaces.» *Surf. Sci.* 85: 326-334.

Gurnett, M., Gustafsson, J.B., Holleboom, L.J., Magnusson, K.O., Widstrand, S.M., Johansson, L.S.O., Johansson, M.K.-J., and Gray S.M. 2005. «Core-level spectroscopy study of the Li/Si(111)−3×1, Na/Si(111)−3×1, and K/Si(111)−3×1 surfaces.» *Phys. Rev. B* 71: 195408-9.

Gurnett, M., Holleboom, L.J., Zhang, H.M., Johansson, L.S.O. 2009. "Photoemission study of the Li/Ge(1 1 1)–3 × 1 reconstruction." *Surf. Sci.* 603: 727-735.

Göthelid, M., Grehk, T.M., Hammar, M., Karlsson, U.O., and Flodström, S.A. 1993. «Adatom and rest-atom contributions in Ge(111)c(2×8) and Ge(111)-Sn(7×7) core-level spectra.» *Phys. Rev. B* 48: 2012-2015.

Hamers, R.J., Tromp, R.M., and Demuth, J.E. 1986. «Scanning tunneling microscopy of Si(001).» *Phys. Rev. B* 34: 5343-5357.

Hasegawa, S.Email Author, Maruyama, M., Hirata, Y., Abe, D., Nakashima, H. 1998. «New model for Si(111)-(3×1)Li through determination of its surface Si atom density with the use of scanning tunneling microscopy.» *Surf. Sci.* 405: L503-L508

Hashizume, Tomihiro, Katayama, Mitsuhiro, Jeon, Dong-Ryul, Aono, Masakazu, Sakurai, Toshio. 1993. «Absolute coverage of K on the Si(111)-3×1-K surface.» *Jpn. J. Appl. Phys. Part 2* 32: L1263-L1265.

Hatta, S., Aruga, T., Kato, C., Takahashi, S., Okuyama, H., Harasawa, A., Okuda, T., and Kinoshita, T. 2008. «Band structure of Tl/Ge(111)−(3×1): Angle-resolved photoemission and first-principles prediction of giant Rashba effect.» *Phys. Rev. B* 77: 245436-8.

Herrera-Gómez, A., Pianetta, P., Marshall, D., Nelson, E., and Spicer, W.E. 2000. «Geometrical structure of the 1/2−ML (2×1) and 1/3−ML (2×3) Ba/Si(001) interfaces.» *Phys. Rev. B* 61: 12988-12991.

Hoeven, A.J., Lenssinck, J.M., Dijkkamp, D., Van Loenen, E.J., Dieleman, J. 1989. "Scanning-tunneling-microscopy study of single-domain Si(001) surfaces grown by molecular-beam epitaxy." *Phys. Rev. Lett.* 63: 1830-1832.

Hofmann, R., Henle, W.A., Netzer, F.P., and Neuber, M. 1992. «Electronic structure of epitaxial Yb silicide.» *Phys. Rev. B* 46: 3857-3864.

Hofmann, R., Netzer, F.P., Patchett, A.J., Barrett, S.D., and Leibsle, F.M. 1993. «The growth of epitaxial Yb silicide: a study with STM.» *Surf. Sci.* 291: 402-410.

Hohenberg, P. and Kohn, W. 1964. "Inhomogeneous Electron Gas." *Phys. Rev.* 136: B864-B871.

Hong, S., Lee, G., Kim, H. 2003. "Structure of Si(111)3×2 Induced by Alkaline-Earth Metals." *J. Korean Phys. Soc.* 47: 100-104.

Iandelli, A., Palenzona, A., and Olcese, G.L. 1979. «Valence fluctuations of ytterbium in silicon-rich compounds.» *J. Less-Common Metals* 64: 213-220.

Jeon, D., Hashizume, T., Sakurai, T., Willis, R.F. 1992. «Structural and electronic properties of ordered single and multiple layers of Na on the Si(111) surface.» *Phys. Rev. Lett.* 69: 1419-1422.

Johansson, L.S.O., Uhrberg, R.I.G., Mårtensson, P., and Hansson, G.V. 1990. "Surface-state band structure of the Si(100)2×1 surface studied with polarization-

dependent angle-resolved photoemission on single-domain surfaces." *Phys. Rev. B* 42: 1305-1315.

Kang, M.-H., Kang, J.-H., and Jeong, S. 1998. «Spectroscopic examination of the Na/Si(111)-(3×1) surface structure.» *Phys. Rev. B* 58, R13359-R13362.

Katkov, M.V., Nogami, J. 2003. "Yb and Nd growth on Si(001)." *Surf. Sci.* 524: 129–136.

Kim, J.-S., Ihm, K.-W., Hwang, C.-C., Kim, H.-S., Kim, Y.-K., Lee, C., and Park, C.-Y. 1999. «Adsorption of Ba on Si(001)2×1 Surface.» *Jpn. J. Appl. Phys.* 38: 6479-6482.

Kirakosian, A., McChesney, J.L., Bennewitz, R., Crain, J.N., Lin, J.-L., Himpsel, F.J. 2002. «One-dimensional Gd-induced chain structures on Si(111) surfaces.» *Surf. Sci.* 498: L109–L112.

Knapp, J.A., and Picraux, S.T. 1986. "Epitaxial growth of rare-earth silicides on (111) Si." *Appl. Phys. Lett.* 48: 466-468.

Kofoed, J., Chorkendorff, I., and Onsgaard, J. 1984. «Structural Investigations of the Yb - Si(111) - 2×1, 5×1 and 3×1 Overlayers.» *Solid State Commun.* 52: 283-286.

Koh, H., Kim, J.W., Choi, W.H., and Yeom, H.W. 2003. "Reinvestigation of the Si 2p photoemission line shape from a clean Si(001)c(4×2) surface." *Phys. Rev. B* 67, 073306-4.

Kohn, W. and Sham, L.J. 1965. "Self-Consistent Equations Including Exchange and Correlation Effects." *Phys. Rev.* 140: A1133-A1138.

Koleshko, V.M., Belitsky, V.F., and Khodin, A.A. 1986. «Thin Films of Rare Earth Metal Silicides.» *Thin Solid Films* 141: 277-285.

Koo, J., Yi, J., Hwang, C., Kim, D., Lee, S., Cho, J. 1996. "Atomic structure of monatomic steps on clean Si(001) and Ni-contaminated Si(001)." *Phys. Rev. B* 54: 10308-10311.

[a]Krachino T.V., Kuzmin, M.V., Loginov, M.V., Mittsev M.A. 1997. «Initial Stages of Formation of a Yb-Si(111) Interface.» *Physics of the Solid State* 39: 224–229.

[b]Krachino T.V., Kuzmin, M.V., Loginov, M.V., Mittsev M.A. 1997. «Thermally Activated Reconstruction in Yb-Si(111) Thin-Film Structures.» *Physics of the Solid State* 39: 1493–1497.

Krachino, T.V., Kuzmin, M.V., Loginov, M.V., and Mittsev, M.A. 1999. «Yb and Sm adsorption and silicide formation on Si(111) surface.» *Phys. Low.–Dim. Struct.* 9/10: 95-106.

Krachino, T.V., Kuzmin, M.V., Loginov, M.V., Mittsev, M.A. 2001. "Adsorption stage of the Eu-Si(111) interface formation." *Appl. Surf. Sci.* 182: 115-132.

Kresse, G. and Hafner, J. 1993. "Ab initio molecular dynamics for liquid metals." *Phys. Rev. B* 47: 558-561.

Kresse, G. and Hafner, J. 1994. "Ab initio molecular-dynamics simulation of the liquid-metal–amorphous-semiconductor transition in germanium." *Phys. Rev. B* 49: 14251-14269.

[a]Kresse, G. and Furthmüller, J. 1996. "Efficiency of ab-initio total energy calculations for metals and semiconductors using a plane-wave basis set." *Computational Materials Science*, 6: 15-50.

[b]Kresse, G. and Furthmüller, J. 1996. "Efficient iterative schemes for ab initio total-energy calculations using a plane-wave basis set." *Phys. Rev. B* 54: 11169-11186.

Kresse, G. and Joubert, D. 1999. "From ultrasoft pseudopotentials to the projector augmented-wave method." *Phys. Rev. B* 59: 1758-1775.

Kubo, O., Saranin, A.A., Zotov, A.V., Ryu, J.-T., Tani, H., Harada, T., Katayama, M., Lifshits, V.G., Oura, K. 1998. «Mg-induced Si(111)-(3×2) reconstruction studied by scanning tunneling microscopy.» *Surf. Sci.* 415: L971-L975.

Kuzmin, M., Laukkanen, P., Vanne, R.-L., Väyrynen, I.J. 2002. «An effect of vicinal surface morphology on adsorbate structure: Yb growth on [11-2]-tilt Si(111).» *Surf. Sci.* 515: 471–482.

[a]Kuzmin, M., Perälä, R.E., Laukkanen, P., Vaara, R.-L., Mittsev, M.A., and Väyrynen, I.J. 2003. «Initial Stages of Yb/Si(100) Interface Growth: 2×3 and 2×6 reconstructions» *Appl. Surf. Sci.* 214: 196-2007.

[b]Kuzmin, M., Vaara, R.-L., Laukkanen, P., Perälä, and Väyrynen, I.J. 2003. «Yb, Eu, and (Yb + Eu)-stabilized 3×1 and 3×2 reconstructions on Si(111).» *Surf. Sci.* 538: 124–136.

[a]Kuzmin, M., Laukkanen, P., Perälä, R.E., Vaara, R.-L., and Väyrynen, I.J. 2004. «Formation of ytterbium silicide nanowires on Si(001).» *Appl. Surf. Sci.* 222: 394-398.

[b]Kuzmin, M., Perälä, R.E., Vaara, R.-L., Laukkanen, P., and Väyrynen, I.J. 2004. «Formation of ytterbium silicide film on Si(001) by solid phase epitaxy.» *J. Cryst. Growth* 262: 231-239.

[c]Kuzmin, M., Vaara, R.-L., Laukkanen, P., Perälä, and Väyrynen, I.J. 2004. «Structural and statistical analysis of Yb/Si(111) and Eu/Si(111) reconstructions.» *Surf. Sci.* 549: 183-195.

[a]Kuzmin, M., Laukkanen, P., Perälä, R.E., Vaara, R.-L., and Väyrynen, I.J. 2005. "Atomic structure of the Eu/Si(111) 3×2, 5×1, and 7×1 surfaces studied by photoelectron spectroscopy." *Phys. Rev. B* 71: 155334-10.

[b]Kuzmin, M., Perälä, R.E., Laukkanen, P., and Väyrynen, I.J. 2005. "Atomic geometry and electronic structure of the Si(100)2×3-Eu surface phase." *Phys. Rev. B* 72, 085343-9.

[a]Kuzmin, M., Laukkanen, P., Perälä, R.E., and Väyrynen, I.J. 2006. «Scanning tunneling microscopy study of the Eu-induced Ge(111)-(3×2)/(3×4) reconstruction.» *Phys. Rev. B* 73: 125332-8.

[b]Kuzmin, M., Perälä, R.E., Laukkanen, P., Ahola-Tuomi, M., and Väyrynen, I.J. 2006. "High-resolution core-level photoemission study of Eu-induced (3×2)/(3×4) reconstruction on Ge(111)." *Phys. Rev. B* 74, 115320-8.

Kuzmin, M., Schulte, K., Laukkanen, P., Ahola-Tuomi, M., Perälä, R.E., Adell, M., Balasubramanian, T., and Väyrynen, I.J. 2007. «Atomic and electronic structure of the Yb/Ge(111)-(3×2) surface studied by high-resolution photoelectron spectroscopy.» *Phys. Rev. B* 75: 165305-8.

Kuzmin, M., Punkkinen, M.P.J., Laukkanen, P., Perälä, R.E., Ahola-Tuomi, M., Balasubramanian, T., and Väyrynen, I.J. 2008. «Yb-induced (2×3) and (2×4) reconstructions on Si(100) studied by first-principles calculations and high-resolution core-level photoelectron spectroscopy.» *Phys. Rev. B* 78, 045318-9.

[a]Kuzmin, M., Laukkanen, P., Perälä, R.E., Punkkinen, M.P.J., Ahola-Tuomi, M., Lång, J., and Väyrynen, I.J. 2010. «Stability, structural, and electronic properties of atomic chains on Yb/Ge(111)3×2 studied by STM and STS.» *Phys. Rev. B* 81: 155312-9.

[b]Kuzmin, M., Punkkinen, M.P.J., Laukkanen, P., Perälä, R.E., Tuominen, V., Lång, J.J.K., Ahola-Tuomi, M., Dahl, J., Balasubramanian, T., Johansson, B., Vitos, L., and Väyrynen, I.J. 2010. «Atomic structure of Yb/Si(100)(2×6): Interrelation between the silicon dimer arrangement and Si 2*p* photoemission line shape.» *Phys. Rev. B* 82: 113302-4.

[a]Kuzmin, M., Punkkinen, M.J.P., Laukkanen, P., Lång, J.J.K., Dahl, J., Tuominen, V., Tuominen, M., Perälä, R.E., Balasubramanian, T., Adell, J., Johansson, B., Vitos, L., Kokko, K., and Väyrynen, I.J. 2011. «Surface core-level shifts on Ge(111)c(2×8): Experiment and theory.» *Phys. Rev. B* 83: 245319-8.

[b]Kuzmin, M., Punkkinen, M.J.P., Laukkanen, P., Lång, J.J.K., Dahl, J., Tuominen, V., Tuominen, M., Adell, J., Balasubramanian, T., Vitos, L., Kokko, K. 2011. «Dimer-T3 reconstruction of the Sm/Si(100)(2×3) surface studied by high-resolution photoelectron spectroscopy and density functional theory calculations.» *Phys. Rev. B* 84: 245322-10.

Kuzmin, M., Punkkinen, M.J.P., Laukkanen, P., Perälä, R.E., Lång, J.J.K., Dahl, J., Adell, J., Kokko, K. 2013. «Photoemission and density functional theory study of Ge(100): Clean surface and Yb-induced (2×4) reconstruction.» *Surf. Sci.* 615: 88–96.

Kuzmin, M., Punkkinen, M.P.J., Laukkanen, P., Lång, J.J.K., Dahl, J., Vitos, L., and Kokko, K. 2014. "Atomic-Level Understanding of Interfaces in the Synthesis of Crystalline Oxides on Semiconductors: Sr- and Ba/Si(100)(2×3) Reconstructions." *J. Phys. Chem. C* 118: 1894−1902.

Kuzmin, M., Laukkanen, P., Yasir, M., Mäkelä, J., Tuominen, M., Dahl, J., Punkkinen, M. P. J., Kokko, K., Hedman, H.-P., Moon, J., Punkkinen, R., Polojärvi, V., Korpijärvi, V.-M., and Guina, M. 2015. "Observation of unusual metal-semiconductor interaction and metal-induced gap states at an oxide-semiconductor interface: The case of epitaxial BaO/Ge(100) junction." *Phys. Rev. B* 92 : 165311-4.

Kuzmin, M., Laukkanen, P., Yasir, M., Mäkelä, J., Tuominen, M., Dahl, J., Punkkinen, M. P. J., Kokko, K., Hedman, H.-P., Moon, J., Punkkinen, R., Lastusaari, M., Polojärvi, V., Korpijärvi, V.-M., and Guina, M. 2016. « Toward the atomically abrupt interfaces of SiO_x/semiconductor junctions. » *Adv. Mater. Interfaces* 2016 : 1500510-5. doi: 10.1002/admi.201500510.

Kuzmin, M., Lehtiö, J.-P., Mäkelä, J., Yasir, M., Rad, Z.J., Vuorinen, E., Lahti, A., Punkkinen, M., Laukkanen, P., Kokko, K., Hedman, H.-P., Punkkinen, R., Lastusaari, M., Repo, P., and Savin, H. 2019. Observation of Crystalline Oxidized Silicon Phase. *Adv. Mater. Interfaces* 6: 1802033-9. DOI: 10.1002/admi.201802033.

Lee, G., Kim, J., Mai, H., Chizhov, I., and Willis, R.F. 2000. "Na- and Li-induced Ge(111)3×1 reconstruction: Different electronic configurations revealed by scanning tunneling microscopy images." *J. Vac. Sci. Technol. A* 18: 1488-1491.

[a]Lee, Geunseop, Hong, Suklyun, Kim, Hanchul, Shin, Dongsoo, Koo, Ja-Yong, Lee, Hyung-Ik, and Moon, Dae Won. 2001. «Structure of the Ba-Induced Si(111)- (3×2) Reconstruction.» *Phys. Rev. Lett.* 87: 056104-4.

[b]Lee, G., Mai, H., and Willis, R.F. 2001. "Scanning tunneling microscopy study of the Li-induced Ge(111)3×1 reconstruction." *Phys. Rev. B* 63: 085323-7.

[c]Lee, G., Kim, J., Chizhov, I., Mai, H., and Willis, R.F. 2001. "Absence of double-bond formation on the Ge(111)3×1−Na surface studied by scanning tunneling microscopy." *Phys. Rev. B* 61: 9921-9924.

Lee, G., Hong, S., Kim, H., Koo, J.-Y. 2003. «Atomic structure of the Ba-induced Si(111)3×2 reconstruction studied by LEED, STM, and ab initio calculations.» *Phys. Rev. B* 68: 115314-8.

Lee, G., Cho, H., Kim, Y., and Shim, H. 2007. «Analysis of Core-Level Spectra of the Li/Ge(111)-3×1 and Na/Ge(111)-3×1 Surfaces.» *J. Phys. Soc. Jpn.* 76: 044704-5.

Lee, J.Y., and Kang, M.-H. 2002. "Atomic structure of alkali metal (Li, Na, K) adsorbed Ge(111)−(3×1) surfaces." *Phys. Rev. B* 66, 233301-4.

Li, Sheng S. 2006. *Semiconductor Physical Electronics.* New York: Springer Science & Business Media.

Liu, B.Z., Nogami, J. 2001. "An STM study of the Si(001)(2×4)-Dy surface." *Surf. Sci.* 488: 399-405.

Liu, B.Z., Nogami, J. 2003. " An STM study of the Si(001) (2×7)–Gd, Dy surface." *Surf. Sci.* 540: 136-144.

Lochner, M., R. Bienert, R., Kürpick, U., Matzdorf, R. 2015. «Dysprosium-induced nanowires on Ge(001).» *Surf. Sci.* 637–638: 42–47.

Lottermoser, L., Landemark, E., Smilgies, D.-M., Nielsen, M., Feidenhans'l, R., Falkenberg, G., Johnson, R.L., Gierer, M., Seitsonen, A.P., Kleine, H., Bludau, H., Over, H., Kim, S.K., Jona, F. 1998. «New bonding configuration on Si(111) and Ge(111) surfaces induced by the adsorption of alkali metals.» *Phys. Rev. Lett.* 80: 3980-3983.

Lukanov, B.R., Reiner, J.W., Walker, F.J., Ahn, C.H., and Altman, E.I. 2011. "Formation of alkaline-earth template layers on Ge(100) for oxide heteroepitaxy: Self-organization of ordered islands and trenches." *Phys. Rev. B* 84: 075330-9.

Lukanov, B., Garrity, K., Ismail-Beigi, S., and Altman E.I. 2012. "Deciphering the atomic structure of a complex Sr/Ge(100) phase via scanning tunneling microscopy and first-principles calculations." *Phys. Rev. B* 85: 195316-5.

Lüth, Hans. 2001. *Solid Surfaces, Interfaces and Thin Films*. Springer-Verlag, Berlin.

Miwa, R.H. 2005. «Energetic stability, equilibrium geometry, and the electronic properties of Ca⁄Si(111) surfaces.» *Phys. Rev. B* 72: 085325-7.

Mönch, Winfried. 2001. *Semiconductor Surfaces and Interfaces*. Springer, Berlin, Heidelberg.

Netzer, Falko P. 1995. "Rare earth overlayers on silicon." *J. Phys.: Condens. Matter* 7: 991-1022.

Nicholls, J.M., Hansson, G.V., Uhrberg, R.I.G., and Flodström, S.A. 1986. «New surface states on the annealed Ge(111) surface.» *Phys. Rev. B* 33, 5555-5559.

Nikolić, M.V., Radić, S.M., Minić, V., and Ristić, M.M. 1996. «The dependence of the work function of rare earth metals on their electron structure.» *Microelectronics Journal* 27 : 93-96.

Nogami, J., Carbone, C., Friedman, D. J., and Lindau, I. 1986. «Electronic Structure of The Yb/Ge(111) Interface.» *Phys. Rev. B* 33: 864-872.

Nogami, J., Liu, B.Z., Katkov, M.V., Ohbuchi, C., Birge, Norman O. 2001. «Self-Assembled Rare-Earth Silicide Nanowires on Si(001).» *Phys. Rev B* 63: 233305-4.

Ohbuchi, C. and Nogami J. 2002. «Holmium growth on Si„(001)…: Surface reconstructions and nanowire formation.» *Phys. Rev. B* 66: 165323–6.

Ohbuchi, C. and Nogami J. 2005. «Samarium-induced surface reconstructions of Si(001).» *Surf. Sci.* 579: 157–165.

Ojima, K., Yoshimura, M., and Ueda, K. 2001. "STM observation of the 2×3 and c(2×6) structures on Ba/Si(100)." *Surf. Sci.* 491: 169-174.

Okuda, T., Shigeoka, H., Daimon, H., Suga, S., Kinoshita, T., Kakizaki, A. 1994. «Surface and Bulk Core Level Shifts of the Si(111) 3 × 1-Na and Si(111) δ7 × 7-Na Surfaces.» *Surf. Sci.* 321: 105-110.

Okuda, T., Sakamoto, K., Nishimoto, H., Daimon, H., Suga, S., Kinoshita, T., Kakizaki, A. 1997. «Angle-resolved photoelectron spectroscopy of the Si(111)3×1-Na surface.» *Phys. Rev. B* 55: 6762-6765.

Okuda, T., Ashima, H., Takeda, H., An, K.-S., Harasawa, A., and Kinoshita, T. 2001. "Experimental surface-state band structure of the Ba-induced Si(111)3×1 surface." *Phys. Rev. B* 64: 165312-7.

Okuda, T., Tohyama, T., Maa, X.-D., Wakita, T., Harasawa, A., Kinoshita, T. 2004. «Surface states band structure of Gd-induced one-dimensional chain structure on Si(111) surface measured by angle-resolved photoelectron spectroscopy.» *J. Electron Spectrosc.* 137–140: 125–129.

Okuda, T., An, K.-S., Harasawa, A., and Kinoshita, T. 2005. "Structural analysis of Ba-induced surface reconstruction on Si(111) by means of core-level photoemission." *Phys. Rev. B* 71: 085317-9.

Olmstead, M.A., Uhrberg, R.I.G., Bringans, R.D., Bachrach, R.Z. 1987. "Photoemission study of bonding at the CaF_2-on-Si(111) interface." *Phys. Rev. B* 35: 7526-7532.

Onsgaard, J., Ghijsen, J., Johnson, R.L., Ørskov, F., Chorkendorff, I, and Grey, F. 1990. «The Sm/Si(100) interface studied by electron spectroscopy.» *J. Electr. Spectrosc. Rel. Phenom.* 52: 67-78.

Onsgaard, J., Christiansen, M., Ørskov, F., and Godowski, P.J. 1991. «The growth and reactivity of the Sm/Si(100) interface.» *Surf. Sci.* 247: 208-214.

Owen, J.H.G., Miki, K., Bowler, D.R. 2006. «Self-Assembled Nanowires on Semiconductor Surfaces.» *J. Mater. Sci.* (2006) 41: 4568–4603.

Özkaya, S., Çakmak, M., Alkan, B. 2010. «Ab Initio Study of Yb on the Ge(111)–(3×2) and Si(111)–(3×2) Surfaces.» *Surf. Sci.* 604: 1899–1905.

Quinn, J., Jona, F. 1991. «New Results on the Reaction of Si(111) with Mg.» *Surf. Sci.* 249: L307-L311.

Paggel, J.J., Haak, H., Theis, W., and Horn K. 1993. «Na adsorption on Si(111)-(7×7) studied by scanning tunneling microscopy and photoemission.» *J. Vac. Sci. Technol. B* 11: 1439-1443.

Paggel, J.J., Neuhold, G., Haak, H., Horn, K. 1995. «Scanning-Tunneling-Microscopy and Photoemission Study of an Alkali-Metal-Induced Structural Phase Transition: Si(111)-(7×7) into Si(111)-Na(3×1).» *Phys. Rev. B* 52: 5813-5823.

Palmino, F., Ehret, E., Mansour, L., Labrune, J.-C., Lee, G., Kim, H., and Themlin, J.-M. 2003. "3×2 reconstruction of the Sm/Si(111) interface." *Phys. Rev. B* 67: 195413-6.

Pashley, M.D. 1989. "Electron counting model and its application to island structures on molecular-beam epitaxy grown GaAs(001) and ZnSe(001)." *Phys. Rev. B* 40: 10481-10487.

Pasquali, L., D'Addato, S., and Nannarone, S. 2002. «Growth of Epitaxial Yb Silicide on Si(100) Studied by Metastable Atom Deexcitation Spectroscopy and Photoemission.» *Phys. Rev. B* 65: 115417-10.

Pehlke, E. and M. Scheffler, M. 1993. "Evidence for site-sensitive screening of core holes at the Si and Ge (001) surface." *Phys. Rev. Lett.* 71: 2338-2341.

Perdew, J.P. and Zunger, A. 1981. "Self-interaction correction to density-functional approximations for many-electron systems." *Phys. Rev. B* 23: 5048-5079.

Perälä, R.E., Kuzmin, M., Laukkanen, P., Vaara, R.-L., and Väyrynen, I.J. 2005. "Eu- and Yb-induced reconstructions on a vicinal Si(100) surface." *Surf. Sci.* 584: 8-16.

Perälä, R.E., Kuzmin, M., Laukkanen, P., Ahola-Tuomi, M., Punkkinen, M.P.J., Väyrynen, I.J. 2009. «Ytterbium on Vicinal Si(100): Growth and Properties of the 2D Wetting Layer and the Yb Silicide Phase.» *Surf. Sci.* 603: 102-108.

Petrovykh, D.Y., Altmann, K.N., Lin, J.-L., Himpsel, F.J., Leibsle, F.M. 2002. "Single domain Ca-induced reconstruction on vicinal Si(111)." *Surf. Sci.* 512: 269-280.

Pomyalov, A., Manassen, Y. 1997. "Local electric field effects in STM of single-atom adsorption on a Si(001) surface." *Surf. Sci.* 382: 275-287.

Preinesberger, C., Becker, S.K., Vandré, Kalka, S.T., and Dähne, M. 2002. «Structure of $DySi_2$ nanowires on Si(001).» *J. Appl. Phys.* 91: 1695-1697.

Punkkinen, M.P.J., Kokko, K., Vitos, L., Laukkanen, P., Airiskallio, E., Ropo, M., Ahola-Tuomi, M., Kuzmin, M., Väyrynen, I.J., and Johansson, B. 2008 "Calculation of surface core-level shifts within complete screening: Problems with pseudohydrogenated slabs." *Phys. Rev. B* 77: 245302-7.

Punkkinen, M.P.J., Kuzmin, M., Laukkanen, P., Perälä, R.E., Ahola-Tuomi, M., Lång, J., Ropo, M., Pessa, M., Väyrynen, I.J., Kokko, K., Johansson, B., and Vitos, L. 2009. «Stability and structure of rare-earth metal and Ba-induced reconstructions on a Si(100) surface.» *Phys. Rev. B* 80: 235307-9.

Redfield, A.C., Zangwill, A. 1992. "Attractive interactions between steps." *Phys. Rev. B* 46: 4289-4291.

Repp, J., Moresco, F., Meyer, G., Rieder, K.-H., Hyldgaard, P., Persson, M. 2000. "Substrate mediated long-range oscillatory interaction between adatoms: Cu/Cu(111)." *Phys. Rev. Lett.* 85: 2981-2984.

Rossi, G., Nogami, J., Lindau, I., Braicovich, L., del Pennino, U., and Nannarone, S. 1983. «First Spectroscopic Investigation of The Yb/Si interface at room temperature.» *J. Vacuum Sci. Technol.* A1 : 781-784.

Rossi, Giorgio. 1987. "*d* and *f* metal interface formation on silicon." *Surf. Sci. Rep.* 7: 1-101.

Sakamoto, K., Okuda, T., Nishimoto, H., Daimon, H., Suga, S., Kinoshita, T., Kakizaki, A. 1994. «Photoemission study of the Si(111)3×1-K surface.» *Phys. Rev. B* 50: 1725-1732.

Sakamoto, K., Takeyama, W., Zhang, H.M., and Uhrberg, R.I.G. 2002. "Structural investigation of Ca/Si(111) surfaces." *Phys. Rev. B* 66: 165319-8.

Sakamoto, K., Pick, A., and Uhrberg, R.I.G. 2005. "Structural investigation of the quasi-one-dimensional reconstructions induced by Eu adsorption on a Si(111) surface." *Phys. Rev. B* 72: 195342-9.

[a]Saranin, A.A., Zotov, A.V., Lifshits, V.G., Ryu, J.-T., Kubo, O., Tani, H., Harada, T., Katayama, M., Oura K. 1998. «Reexamination of the reconstruction on the basis of Si atom density and unit cluster determination.» *Phys. Rev. B* 58: 3545-3548.

[b]Saranin, A.A., Zotov, A.V., Lifshits, V.G., Katayama, M., Oura K. 1998. «Family of the metal-induced Si(111)3×1 reconstructions with a top Si atom density of 4/3 monolayer.» *Surf. Sci.* 426: 298-307.

[c]Saranin, A.A., Zotov, A.V., Ryzhkov, S.V., Tsukanov, D.A., Lifshits, V.G., Ryu, J.-T. Kubo, O. Tani, H., Harada, T., Katayama, M., and Oura, K. 1998. «Si(100)2×3−Na surface phase: Formation and atomic arrangement.» *Phys. Rev. B* 58, 4972-4976.

Saranin, A.A., Lifshits, V.G., Ignatovich, K.V., Bethge, H., Kayser, R., Goldbach, H., Klust, A., Wollschläger, J., Henzler, M. 2000. «Restructuring process of the Si(111) surface upon Ca deposition.» *Surf. Sci.* 448: 87-92.

Sekiguchi, T., Shimokoshi, F., Nagao, T., Hasegawa, S. 2001. "A series of Ca-induced reconstructions on Si(111) surface." *Surf. Sci.* 493: 148-156.

Shinde, A., Cao, J., Ouyang, W., Wu, R., Ragan, R. 2009. "Determination of preferential rare earth adatom adsorption geometries on Si(001)." *Physics Letters A* 373: 3459-3463.

Smith, G.S., Johnson, Q., and Tharp, A.G. 1965. «The crystal structure of Yb_3Ge_5.» *Acta Cryst.* 18 : 1085-1086.

Streetman, Ben G., Banerjee, Sanjay. 2000. *Solid State Electronic Devices*. New Jersey : Prentice Hall.

Sun, X., Merckling, C., Heyns, M., Dekoster, J., and Caymax, M. 2011. "Submonolayer barium passivation study for germanium(100)/molecular beam epitaxial Al_2O_3." *Appl. Phys. Lett.* 98: 212903-3.

Takada, S., Sakamoto, K., Kobayashi, K., Suzuki, T., Harasawa, A., Okuda, T., Kinoshita, T. 2006. «Surface Electronic Structure of the (3×2) Reconstruction Induced by Yb on a Si(111) Surface.» *Appl. Surf. Sci.* 252: 5292–5295.

Takeuchi, N., Selloni, A., and Tosatti, E. 1992. "Do we know the true structure of Ge(111)c(2×8)?" *Phys. Rev. Lett.* 69: 648-651.

Tallaj, N., and Buyle-Bodin, M. 1977. "Work Function Measurements on Germanium by Thermionic Emission." *Surf. Sci.* 69: 428-436.

Tersoff, J. and Hamann, D.R. 1983. «Theory and Application for the Scanning Tunneling Microscope.» *Phys. Rev. Lett.* 50: 1998-2001.

Tersoff, J. and Hamann, D.R. 1985. «Theory of the scanning tunneling microscope.» *Phys. Rev. B* 31: 805-813.

Thompson, R.D. and Tu, K.N. 1982. «Comparison of the three classes (rare earth, refractory and near-noble) of silicide contacts.» *Thin Solid Films* 93: 265-274.

Tung, Raymond T. 2014. « The physics and chemistry of the Schottky barrier height. » *Applied Physics Reviews* 1 : 011304-54.

Uhrberg, R.I.G. 2001. "High-resolution core-level spectroscopy of Si(100)c(4×2) and some metal-induced Si(111)√3×√3 surfaces." *J. Phys.: Condens. Matter* 13: 11181-11194.

[a]Vaara, R.-L., Kuzmin, M., Perälä, R.E., Laukkanen, P., Väyrynen, I.J. 2003. «Formation and Thermal-Desorption-Controlled Patterning of Yb-Induced Structures on Vicinal Si(111) [-1-12]-Miscut Surface.» *Surf. Sci.* 529: L229–L233.

[b]Vaara, R.-L., Kuzmin, M., Perälä, R.E., Laukkanen, P., Väyrynen, I.J. 2003. «Evolution of Step and Terrace Structure on [-1-12]- and [11-2]-Miscut Si(111) Surfaces Upon Formation of Triple- and Single-Domain Yb-Induced 3×2 reconstruction.» *Surf. Sci.* 539: 72–80.

[c]Vaara, R.-L., Kuzmin, M., Laukkanen, P., Perälä, R.E., Väyrynen, I.J. 2003. "Two series of triple- and single-domain reconstructions induced by europium on vicinal Si(111) [-1-12]-miscut surface." *Appl. Surf. Sci.* 220: 327-334.

Wachs, A.L., Miller, T., Hsieh, T.C., Shapiro, A.P., and Chiang, T.-C. 1985. «Angle-resolved photoemission studies of Ge(111)-c(2×8), Ge(111)-(1×1)H, Si(111)-(7×7), and Si(100)-(2×1).» *Phys. Rev. B* 32: 2326-2333.

Wan, K.J., Lin, X.F., Nogami, J. 1992. «Comparison of the 3×1 reconstructions of the Si(111) surface induced by Li and Ag.» *Phys. Rev. B* 46: 13635-1638.

Wan, K.J., Lin, X.F., Nogami, J. 1993. «Surface Reconstructions in the Ag/Si(111) System.» *Phys. Rev. B* 47: 13700-13712.

Wang, J., Hallmark, J.A., Marshall, D.S., Ooms, W.J., Ordejón, P., Junquera, J., Sánchez-Portal, D., Artacho, E., Soler, J.M. 1999. «Bonding and diffusion of Ba on a Si(001) reconstructed surface.» *Phys. Rev. B* 60: 4968-4971.

Wieling, S., Molodtsov, S.L., Laubschat, C., and Behr G. 2002. "Electronic and crystalline structure of epitaxial $EuNi_x$ films grown on Ni(111)." *Phys. Rev. B* 65, 075415-6.

Weitering, H.H., Shi, X., Erwin, S.C. 1996. «Band Dispersions of the π-Bonded-Chain Reconstruction of Si(111)3×1-Li: A Critical Evaluation of Theory and Experiment.» *Phys. Rev. B* 54: 10585-10592.

Weitering, H.H., Dinardo, N.J., Pérez-Sandoz, R., Chen, J., Mele, E.J. 1994. «Structural model for the metal-induced Si(111)3×1 reconstruction.» *Phys. Rev. B* 49: 16837-16840.

Weitering, H.H. 1996. "New barium-induced surface reconstructions on Si(111)." *Surf. Sci.* 355: L271-L277.

Wigren, C. Andersen, J.N., Nyholm, R., Karlsson, U.O. 1991. "Growth and epitaxy of Yb silicides on Si(111)." *J. Vac. Sci. Technol.* A 9: 1942-1945.

[a]Wigren, C., Andersen, J.N., Nyholm, R., Karlsson, U.O., Nogami, J., Baski, A.A., Quate, C.F. 1993. «Adsorption-Site Determination of Ordered Yb on Si(111) Surfaces.» *Phys. Rev. B* 47: 9663-9668.

[b]Wigren, C., Andersen, J.N., Nyholm, R., Göthelid, M., Hammar, M., Törnevik, C., Karlsson, U.O. 1993. «Sm- and Yb-Induced Reconstructions of the Si(111) Surface.» *Phys. Rev. B* 48: 11014-11019.

Wingerden, J. van, Dam, A. van, Haye, M.J., Scholte, P.M.L.O., and Tuinstra, F. 1997. "Atomic details of step flow growth on Si(001)." *Phys. Rev. B* 55: 9352-9355.

Wolkow, R.A. 1992. «Direct observation of an increase in buckled dimers on Si(001) at low temperature.» *Phys. Rev. Lett.* 68: 2636-2639.

Wu, Tian-Li; Tseng, Yang-Yan; Huang, Chih-Fang; Chen, Zih-Sin; Lin, Chih-Chien; Chung, Chung-Jen; Huang, Po-Kai; Kao, Kuo-Hsing. 2019. "Demonstration of Annealing-free Metal-Insulator-Semiconductor (MIS) Ohmic Contacts on a GaN Substrate using Low Work-function Metal Ytterbium (Yb) and Al_2O_3 Interfacial Layer." Published in: 2019 IEEE Workshop on Wide Bandgap Power Devices and Applications in Asia (WiPDA Asia). *IEEE Xplore Digital Library*. Date of Conference: 23-25 May 2019. Date Added to IEEE Xplore: 15 July 2019. INSPEC Accession Number: 18919648. doi: 10.1109/WiPDAAsia.2019.8760323.

Xu, W., Adams, J.B., Einstein, T. 1996. "Oscillatory interaction of steps on W(110)." *Phys. Rev. B* 54, 2910-2916.

Yang, J., Cai, Q., Wang, X.-D., Koch, R. 2003. «Initial stages of erbium disilicide formation on Si(001).» *Surf. Sci.* 526: 291–296.

Yang, S., Zhang, L., Chen, H., Wang, E., and Zhang, Z. 2008. "Generic guiding principle for the prediction of metal-induced reconstructions of compound semiconductor surfaces." *Phys. Rev. B* 78: 075305-12.

Yeom, H.W., Abukawa, T., Takakuwa, Y., Fujimori, S., Okane, T., Ogura, Y., Miura, T., Sato, S., Kakizaki, A., and Kono, S. 1998. "Anisotropy of the spin-orbit branching ratio in angle-resolved photoemission from adsorbate layers." *Surf. Sci. 395*: L236-L241.

Yokotsuka, T., Kono, S., Suzuki, S., and Sagawa, T. 1984. «Study of Electronic Structures of Ge(111)7 ×7-Sn and Ge(111) "2 ×8" Surfaces by Angle-Resolved UPS.» *J. Phys. Soc. Jpn.* 53: 696-701.

Yoon, M., Mai, H., Lee, G., Willis, R.F. 2000. «Stabilizing influence of double bonds on the Si(111)-(3×1) and Ge(111)-(3×1) surface reconstructions: new experimental evidence.» *Surf. Sci.* 463: 183-190.

Zhang, L., Wang, E.G., Xue, Q.K., Zhang, S.B., and Zhang, Z. 2006. "Generalized Electron Counting in Determination of Metal-Induced Reconstruction of Compound Semiconductor Surfaces." *Phys. Rev. Lett.* 97: 126103-4.

Zhu, S., Chen, J., Li, M.-F., Lee, S.J., Singh, J., Zhu, C.X., Du, A., Tung, C.H., Chin, A., and Kwong, D.L. 2004. «N-Type Schottky Barrier Source/Drain MOSFET Using Ytterbium Silicide.» *IEEE Electron Device Lett.* 25: 565-567. doi: 10.1109/LED.2004.831582.